Fall 2014

Development of a static bioactive stent prototype and dynamic aneurysm-on-a-chip(TM) model for the treatment of aneurysms

Lisa M. Reece
Purdue University, Birck Nanotechnology Center

PURDUE UNIVERSITY
GRADUATE SCHOOL
Thesis/Dissertation Acceptance

This is to certify that the thesis/dissertation prepared

By Lisa M. Reece

Entitled
DEVELOPMENT OF A STATIC BIOACTIVE STENT PROTOTYPE AND DYNAMIC
ANEURYSM-ON-A-CHIP MODEL FOR THE TREATMENT OF ANEURYSMS

For the degree of   Doctor of Philosophy

Is approved by the final examining committee:

James F. Leary

Sophie A. Lelievre

Sherry L. Voytik-Harbin

Steven T. Wereley

To the best of my knowledge and as understood by the student in the Thesis/Dissertation Agreement, Publication Delay, and Certification/Disclaimer (Graduate School Form 32), this thesis/dissertation adheres to the provisions of Purdue University's "Policy on Integrity in Research" and the use of copyrighted material.

James F. Leary

Approved by Major Professor(s): _____

Approved by: Laurie A. Jaeger   12/02/2014

Head of the Department Graduate Program   Date

DEVELOPMENT OF A STATIC BIOACTIVE STENT PROTOTYPE AND DYNAMIC ANEURYSM-ON-A-CHIP™ MODEL FOR THE TREATMENT OF ANEURYSMS

A Dissertation

Submitted to the Faculty

of

Purdue University

Lisa M. Reece

In Partial Fulfillment of the

Requirements for the Degree

Doctor of Philosophy

December 2014

Purdue University

West Lafayette, Indiana

To Ron, Autumn, and Ron Jr., for making my life so blessed with your forbearance, love,

understanding, and lots of humor and laughs! I could not have done this without your

devotion to me and our devotion to each other.

ACKNOWLEDGEMENTS

I would like to acknowledge and thank my Lord and Savior, Jesus Christ, because without Him I would not have been able to endure the many hours of hard work, study, and fortitude required to get this far in my academic or personal life.

I wish to recognize my family members in Illinois, Oklahoma, Missouri, and Texas who have prayed for me and have encouraged me. They never forgot to cheer me up and make me feel loved and important. Thank you so much for all of the support through the years.

To my dissertation committee: James F. Leary, Sophie Lelièvre, Sherry Voytik-Harbin, and Steven Wereley, I offer my deepest thanks and gratitude for guiding me through a very rewarding project and giving me helpful advice and showing faith in me. I want to also thank Raji Sundararjan, who has helped me with prayers, love, enthusiasm, great advice, and scientific counselling. I must express great appreciation to Jean Paul Allain who was instrumental in obtaining funding for the initial project, and for allowing me to be a Co-PI with him on the grant.

I want to thank the graduate students without whom I could not have performed a lot of

the work in a timely manner: Sandra Arias, Moník Echeverry, Jian-Wei Khor, Fernando Pastrana, Raviraj Thakur, and Emily Walker. Christy Cooper has always been a close friend and colleague with whom it has been fun to hang out, share an office and enjoy stimulating conversations, but I also want to say 'thank you' for all the chemistry help she has provided me. I want to recognize Desirée White-Schenk for always helping me out and for being a great sounding board when our mutual frustrations ran high.

Heartfelt sentiments go to Gloria Powell who helped me with the graduate school red tape. In addition, I would like to express my gratitude to the BMS Department Chair: Laurie Jaeger, who has gone to bat for me along with Dr. Leary on more than one occasion. For this, I am extremely humbled and forever grateful.

I cannot continue without recognizing my Birck Nanotechnology Center family: all the engineers, managers, and other staff (especially Nancy Black, Kenny Schwartz, Guy Telesnicki, and Ira Young). You have made my academic and professional life all the more enjoyable and bearable. I consider myself blessed to have worked beside such a remarkable group of experienced, talented people. I also want to thank Mary Jo Totten for the love, support and prayers she has given me especially through a particularly difficult time in my life.

Finally, it is with increased satisfaction that I wish to express my thanks to my boss, mentor, advisor, colleague and dear friend of many years, Dr. Leary. You have been a great influence on my career and life and have helped to shape it with your skill,

intelligence, wit, verve, humor, and patience. You have been a huge inspiration to me and it has been one of my greatest pleasures to have had the opportunity to work for you and beside you these many years.

TABLE OF CONTENTS

LIST OF TABLES

LIST OF FIGURES

LIST OF ABBREVIATIONS

2D: Two dimensional

AOC: Aneurysm-on-a-Chip™

A-T: Adenine-thymine bundle

BioMEMS: Biological micro-electrical mechanical system

BNC: Bacterial nanocellulose

BSA: Bovine serum albumin

BSC: Biological safety cabinet

C: Celsius

CA: Citric acid

CD34: Cluster designation 34 antibody

CFD: Computational fluid dynamics

cm: Centimeter

CO_2: Carbon dioxide

DAPI: 4',6-diamidino-2-phenylindole

DNA: Deoxyribonucleic acid

DPBS: Dulbecco's phosphate buffered saline

EC: Endothelial cells

ECM: Extracellular matrix

EDS: Energy dispersive spectroscopy

ELP: Elastin-like polymers

EP: Electroporation

EPC: Endothelial progenitor cells

Fe: Iron

g: Grams

GCC: General Cross Correlation

GDC: Guglielmi detachable coils

GUI: Graphic user interface

H_2O_2: Hydrogen peroxide

H_2SO_4: Sulfuric acid

h: Hour

HASMC: Human aortic smooth muscle cells

HCl: Hydrochloric acid

hMSC: Human mesenchymal stem cells

IA: Intracranial aneurysms

ID: Inner diameter

IONP: Iron oxide nanoparticles

ISAT: The International Subarachnoid Aneurysm Trial

JPEG: Joint Photographic Experts Group

kV: Kilovolts

keV: Kiloelectron volts

kPA: Kilopascals

LSMF: Life Science Microscopy Facility at Purdue

M: Molar

MACS: Magnetic activated cell sorting

MBNC: Magnetic bacterial nanocellulose

min.: Minutes

mj: Millijoules

ml: Milliliter(s)

MNP: Magnetic nanoparticles

MP: Megapixel

mS: Millisecond

mT: Milliteslas

MTT: 3-(4,5-Dimethylthiazol-2-yl)-2,5-diphenyltetrazolium bromide

MWSS: Mean wall shear stress

μl: Microliters

μm: Microns, micrometers

μM: Micromoles

μs: Microseconds

μTAS: Micro-total-analysis-systems

N: Normal

NH_4OH: Sodium hydroxide

nl: Nanoliters

nm: Nanometers

nM: Nanomoles

NP: Nanoparticles

O: Oxygen

PBS: Phosphate buffered saline

PDMS: Polydimethylsiloxane

PEG: Poly(ethylene glycol)

PEI: Polyethyleneimine

PGS: Poly(glycerol sebacate)

PHA: Polyhydroxylalkanoates

PI: Propidium iodide

PIV: Particle image velocimetry

PMMA: Poly(methyl methacrylate)

ppm: Parts per million

RF: Radio frequency

RGD: Peptide sequence of arginine-glycine-aspartic acid

RPC: Robust phase correlation

rpm: Revolutions per minute

s: Seconds

SAH: Subarachnoid hemorrhaging

SEM: Scanning electron microscopy

SiOH: Silanol

SMC: Smooth muscle cells

SPION: Super paramagnetic iron oxide nanoparticles

TEBV: Tissue engineered blood vessels

TEM: Transmission electron microscopy

UV: Ultraviolet

V: Volts

WSS: Wall shear stress

ABSTRACT

Reece, Lisa M., Ph.D., Purdue University, December 2014. Development of a Static Bioactive Stent Prototype and Dynamic Aneurysm-on-a-Chip™ Model for the Treatment of Aneurysms. Major Professor: James F. Leary.

Aneurysms are pockets of blood that collect outside blood vessel walls forming dilatations and leaving arterial walls very prone to rupture. Current treatments include: (1) clipping, and (2) coil embolization, including stent-assisted coiling. While these procedures can be effective, it would be advantageous to design a biologically active stent, modified with magnetic stent coatings, allowing cells to be manipulated to heal the arterial lining. Further, velocity, pressure, and wall shear stresses aid in the disease development of aneurysmal growth, but the shear force mechanisms effecting wound closure is elusive. Due to these factors, there is a definite need to cultivate a new stent device that will aid in healing an aneurysm *in situ*. To this end, a static bioactive stent device was synthesized. Additionally, to study aneurysm pathogenesis, a lab-on-a-chip device (a dynamic stent device) is the key to discovering the underlying mechanisms of these lesions. A first step to the reality of a true bioactive stent involves the study of cells that can be tested against the biomaterials that constitute the stent itself. The second step is to test particles/cells in a microfluidic environment. Therefore, biocompatability data was collected against PDMS, bacterial nanocellulose (BNC), and magnetic bacterial nanocellulose (MBNC). Preliminary static bioactive stents were synthesized whereby

BNC was grown to cover standard nitinol stents. In an offshoot of the original research, a two-dimensional microfluidic model, the Aneurysm-on-a-Chip™ (AOC), was the logical answer to study particle flow within an aneurysm "sac" – this was the dynamic bioactive stent device. The AOC apparatus can track particles/cells when it is coupled to a particle image velocimetry software (PIV) package. The AOC fluid flow was visualized using standard microscopy techniques with commercial microparticles/cells. Movies were taken during fluid flow experiments and PIV was utilized to monitor the flow of particles within the "sac" region, and exiting the device. Quiver plots were generated from fluid flow experiments using standard 7 μm latex particles and fixed HASMC in PBS. PIV analysis shows that the particles flowed nicely from input to output. Wall shear stress provided evidence that there was some back flow at the edge of the "sac".

CHAPTER 1. INTRODUCTION

1.1   <u>Rationale</u>

Aneurysms are pockets of blood that collect outside blood vessel walls forming

dilatations and leaving arterial walls weak and very prone to rupture. Current treatments

incorporate: (1) clipping, and (2) coil embolization, including stent-assisted coiling.

While these procedures can be effective, it would be advantageous to design a

biologically active stent, modified with magnetic stent coatings, allowing endothelial and

smooth muscle cells to be manipulated to heal the arterial lining. However, cell behavior

is influenced by surface chemistry, material stiffness, and surface topography, where

changes in nanotopography result in alterations in cell proliferation, adhesion,

differentiation, and gene expression. Further, very little is known about the recruitment

and adhesion of blood vessel cells to different stent coatings exhibiting various

topographies, thus if these mechanisms are better understood, correct topography and

surface chemistry of stent materials may be generated. Another aspect of aneurysm

treatment is the study of how aneurysms form and behave. Velocity, pressure, and wall

shear stresses can aid in pathogenesis and aneurysmal growth [1]. Further, the evolution

of an aneurysm is assumed to be caused by the remodeling of the affected blood vessel's

material constituents (tunica intima, tunica media, or tunica adventitia) [2]. It was

proposed that there was a need for a minimally invasive alternative aneurysm treatment

method such that a bioactive stent prototype would be generated. Out of this work, there developed a requisite to synthesize a device to study aneurysm fluid flow patterns. Therefore, a first step to realizing a bioactive stent and to better understand the formation of aneurysms and the fluid dynamics inside of them, is to design and fabricate a two-dimensional microfluidic model (Aneurysm-on-a-Chip™). The goal of this work is to first identify and test individual components that would make up a bioactive stent and then develop the Aneurysm-on-a-Chip™ (AOC) bioMEMS device to allow for the visualization of cells flowing through an artificial blood vessel environment and quantify the dynamic flow properties within the "aneurysmal sac" as well as entering and exiting the "lesion" [3]. The first two specific aims are to be considered background material vital to the realization of a static bioactive stent prototype. The third specific aim has led to the synthesis and testing of the Aneurysm-on-a-Chip™ that is considered a dynamic stent prototype.

1.2   <u>Specific Aims</u>

Aim 1: Enhance cells and bacterial nanocellulose for ultimate attraction to a static bioactive stent. By rendering the static bioactive stent prototype magnetic, one could effectively attract magnetically labeled cells locally against shearing constraints from a pulsating environment. The first step to realizing this aim is to bind magnetic nanoparticles to human aortic smooth muscle cells (HASMC) thus rendering them magnetic. Passive uptake and electroporation techniques are utilized to label the cells since there is no commercially available magnetic antibody particles for this cell type, and binding schemes of antibody to existing nanoparticles, is beyond the scope of this

research project. Electroporation is a technique whereby cells are subjected to a brief electrical pulse so that when pores open in the membrane, molecules, particles, etc. may enter the cell through the pores and label those cells within the cytoplasm [4]. Further, a biocompatible material, bacterial nanocellulose (BNC), is synthesized and later rendered magnetic (MBNC) via a thermal magnetic nanoparticle synthesis reaction, and subsequently coated to assure biocompatibility for the iron oxide nanoparticles (IONP) impregnating the BNC matrix. The MBNC should attract magnetic HASMC to itself to induce proliferation and growth of these cells. The ultimate goal is to allow the magnetic HASMC to proliferate across the aneurysm neck where the static bioactive stent is placed.

Aim #2: Improve and promote tissue growth and biocompatibility utilizing bacterial nanocellulose. Migration studies for HASMC have been carried out to determine how well cells growing on a substrate moved to an "open" area or synthetic "wound". This helps to show how feasible it is for cells to migrate *in vivo* across the aneurysm neck once they have been magnetically attracted to the static bioactive stent. Cellular health must be maintained to assess migration, therefore, cytotoxicity experiments are performed against the materials with which cells come into contact: BNC and MBNC. The biocompatability of these constituents is vital in order for the static bioactive stent to be tolerated in a blood vessel *in vivo*. The CometAssay® is employed to detect any DNA damage that may be incurred by the cells as a result of exposure to the BNC and MBNC.

Aim #3: Design and development of a dynamic 2D Aneurysm-on-a-Chip™ (AOC) Model. To begin to study aneurysm development, fluid flow patterns must be studied using the AOC, which is considered a dynamic form of the bioactive stent prototype. Experiments carried out include running simple microspheres flowing in water and phosphate buffered saline to fixed HASMC running in PBS. The AOC device is connected to a laptop computer housing the controller software. Fluid flow analyses are performed by observing particles flowing through the AOC under a microscopic field of view. The microscope is attached to a camera coupled to image acquisition software, whereby movies and still images are taken as particles flow through the AOC mechanism. Parameters measured within the AOC prototype are wall shear stress (WSS) and PIV.

CHAPTER 2. BACKGROUND

2.1   Definition of Aneurysms

In layman's terms, aneurysms are pockets of blood (hematomas) that collect outside of

the layers of blood vessel walls and form balloon-like bulges (dilatations or aneurysmal

sacs) that weaken those walls [1, 3–8]. While there are different varieties of aneurysms,

they all share some basic characteristics – they are all defects of the arterial blood vessel

wall. To understand these lesions better, it is important to first appreciate the structure

and function of blood vessel walls. Blood vessels regulate the blood flow in the body and

are made up of three layers of tissue: tunica intima, tunica media (made up of smooth

muscle fibers that widen or narrow the size of the vessel), and tunica adventitia (also

known as tunica extrema) (Figure 2.1) [11]. These dilatations may occur in any artery or

vein in the body and are first classified as true or false aneurysms [3, 6, 10]. A true

aneurysm is bounded by complete blood vessel walls but with altered structure. For

example, the most common histologic discovery is a decrease in the tunica media [5]. It

is important to note also that the blood in true aneurysms remains in the circulatory

system [8]. False aneurysms (pseudoaneurysms) can occur in any blood vessel of the

body as well but rarely naturally occur within the skull [13]. They are different from true

aneurysms in that the vascular lumen does not enlarge, although the diameter of the

abnormal blood vessel segment may be increased. Here, the vascular wall has been

breached and the aneurysmal sac thus consists of only the outer blood vessel layers [8].
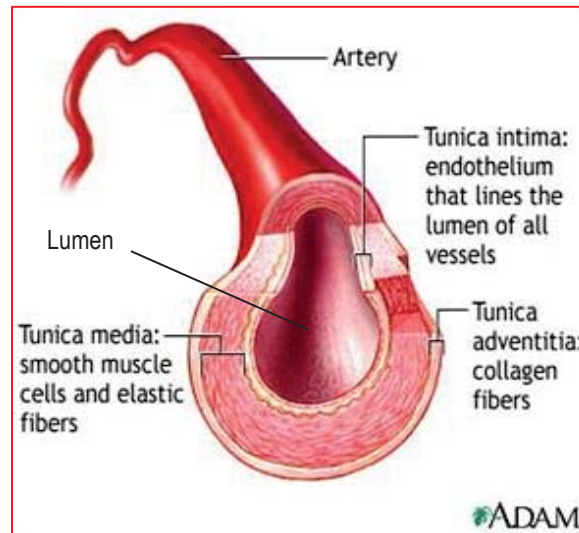
Figure 2.1. The tissue layers of a blood vessel – tunica intima, tunica media, and tunica adventitia (adapted from Weinrauch L.A., Zieve D., Patient Education, 2009) [11].

Other classifications of aneurysms can be based on morphology, size, location (posterior

circulation vs. anterior circulation), etiology [4, 6], and clinical presentation (ruptured vs.

unruptured) [12]. Morphology is centered on the protruding arterial walls of the

aneurysm that can take on three different shapes: saccular, fusiform, and dissecting [11–

13] (Figure 2.2). Saccular aneurysms are spherical and can range from 5-20 cm in

diameter. Fusiform aneurysms have a gradual, progressive outpouching that includes the

complete circumference of the blood vessel. Fusiform aneurysms vary in diameter up to

20 cm and may involve the entire aortic arch or large segments of the abdominal aorta.

Dissecting aneurysms occur when blood enters the wall of the artery and collects in

between (or dissects) the tunica intima, tunica media and/or tunica adventitia whereby a

cavity is created within the vessel wall itself [8]. There are subgroupings of size

categorizations as well. "Small" aneurysms are considered to be less than 10 mm, "large"

is 10-25 mm, and "giant" is 25 mm and above [14]. Interestingly, it has been determined

that aneurysms smaller than 12 mm in dome size account for more than 75% of

unruptured aneurysms [14, 15].
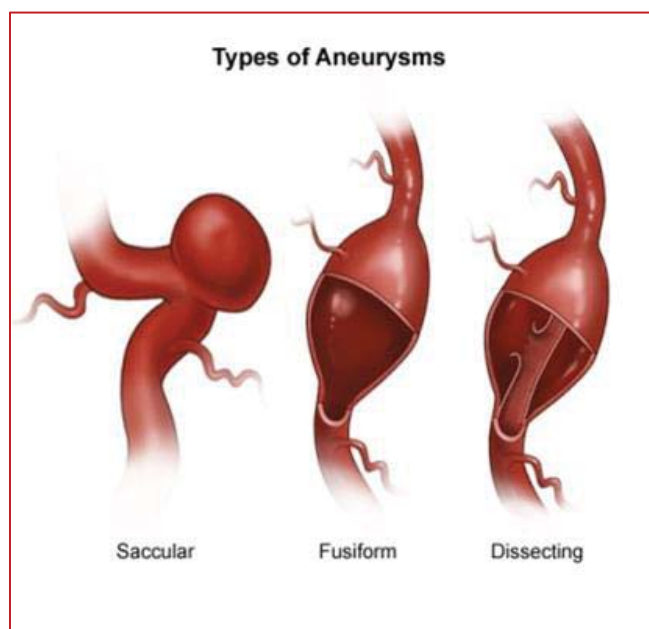
Figure 2.2. The three types of aneurysms – saccular, fusiform, and dissecting
(Endovascular Coiling, Johns Hopkins Medical Center, 2012).

2.2   Common Treatments of Aneurysms

Common aneurysmal treatments include clip ligation and coiling [5]. For example, the

broader treatment plan for a patient suffering a subarachnoid hemorrhage (SAH) due to a

ruptured aneurysm is focused on: (1) treatment of the primary brain injury of the

hemorrhage itself, (2) the necessary supportive, prophylactic, and interventive therapies

for the secondary effects of the bleeding (e.g., cerebral vasospasms), and (3) direct treatment of the aneurysm itself [18]. Concerning the treatment of the initial aneurysm bleed, randomized trials have led to several therapies being discarded because of the serious concern of doing more harm than good, including the use of antifibrinolytic agents [19], sublingual nifedipine (a calcium channel blocker), fluid restriction for hyponatremia (low sodium ions in the blood), delayed clip ligation, and the use of other vasodilators [16–18]. Prophylactic therapies, on the other hand, are available to control the effects on the brain after a bleeding episode has occurred. Vasospasms after SAH are a common occurrence and the treatment regimen is complex including the use of oral vasodilators and cerebral angioplasty (balloon catheterization) among others [16]. The International Subarachnoid Aneurysm Trial (ISAT) performed a study of patients with ruptured aneurysms and found no difference in fatality rates between clipping and coiling [19, 20], while in the setting of an unruptured aneurysm, the minimally invasive procedure of endovascular coiling afforded a shorter recovery time [21, 22].

2.2.1 Coiling Therapy to Occlude Aneurysms

The primary goal of coiling therapy is to tightly pack an aneurysm with coils to promote thrombosis and ultimately endothelialization across the aneurysm orifice [25] to cut off the blood flow into the aneurysm sac and strengthen the weakened blood vessel wall. Coiling is performed under general anesthesia utilizing fluoroscopic guidance [12, 24], and patients are given heparin (an anticoagulant) during catheterization and coil placement [26]. Typically, a large catheter (5-7 French or 1.7-2.3 mm in diameter) is guided to the aneurysm site via the femoral, internal carotid, or vertebral artery –

depending on the location of the aneurysm. A microcatheter (1.7-2.3 French or 0.6-0.8 mm in diameter) is navigated over a microwire (0.014"). Once the best view that clearly delineates the aneurysm neck and surrounding arterial branches is obtained, the microcatheter is advanced into the aneurysm. Coils are then deployed and detached through the microcatheter using either a hydraulic or electrolytic mechanism [14].

There are a variety of coils currently in use today and one type of coil, called Guglielmi detachable coils (GDC), forms the basis of contemporary endovascular treatment of intracranial aneurysms (IA) [27]. Standard platinum coils are also available and have been modified to become biologically active to reduce canalization [26–28]. Matrix coils have been reported to be worse than standard bare platinum coils due to less dense packing and less complete occlusion of the aneurysm after treatment [19, 27]. Besides occluding the aneurysm, a secondary goal behind coiling involves the tight packing of the coils to prevent the shift of the embolic sac over time. This requires filling the large volume in the aneurysm sac completely and effectively, as seen in Figure 2.3 [15], and may require a large number of coils. The objectives of this treatment strategy are admirable but realistically, coiling does have its drawbacks. One of the problems with coiling lies with the last few coils becoming misplaced due to resistance met by the existing coils. This can cause bulging in the parent blood vessel, or worse, failure to deploy at all in the already dense nest of coils resulting in embolization downstream [27, 29]. As serious a complication as embolization is, the possibility of recanalization of the aneurysm attributable to coil compaction is just as critical [21, 24, 26, 28, 30] and remains the major limitation of coiling, particularly for wide-necked or larger aneurysms.

Indeed, the rate of late aneurysmal regrowth after coil embolization is also of great concern and is extremely high (33% or more) for large or giant aneurysms [24, 28, 30].

To facilitate coiling of some aneurysms/pseudoaneurysms, many clinicians deploy stents across the aneurysmal neck to act as a supporting bridge or scaffold for the coils and help facilitate thrombus formation within the aneurysm [22, 31]. To illustrate, stent-assisted coiling of IA has allowed for effective treatment of fusiform or very wide neck aneurysms in which other surgical or endovascular treatment strategies have not been considered feasible [12, 24, 31]. A coil delivery microcatheter is first introduced into the aneurysm sac and then the self-expandable stent is navigated into the parent vessel. Next, the stent is carefully deployed across the aneurysm neck followed by coil placement and detachment [12, 24, 31]. Figure 2.4 shows a diagram of a stent (Fig. 2.4.a.) and the varieties of stent placements available to treat different blood vessel configurations [33] (Fig. 2.4.b.,c.,d.).
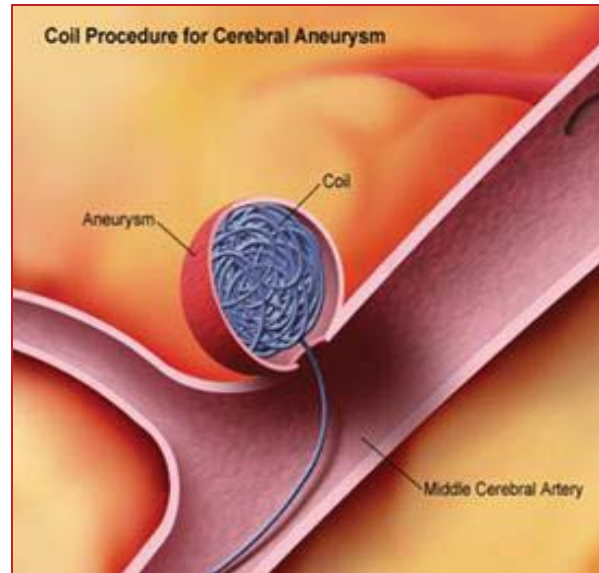
Figure 2.3. Illustration of endovascular coiling of a cerebral aneurysm (Endovascular Coiling, Johns Hopkins Medical Center; 2012).
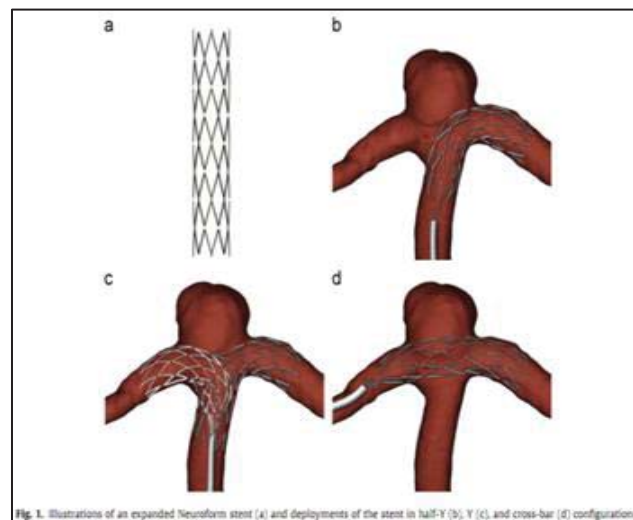
Figure 2.4. Example of a stent (Panel a) and stent deployment configurations (Panels b, c, and d) [33].

Remarkably, a stent-assisted coiling procedure can be a multi-stage process where the stent is deployed first followed by the introduction of coils 6-8 weeks later. Moreover, high porosity stents have been used as stand-alone treatments in certain cases where coil embolization is not permitted [33]. Understandably, while stent-assisted coiling has expanded the treatment of IA, the rates of procedure-related neurological complications and the incidence of angiographic aneurysm recurrence after employment of this technique is not fully understood [26]. Another factor associated with increased risk of aneurysmal recurrence includes treatment of ruptured rather than unruptured aneurysms [3, 13, 16, 19]. It is for these reasons that the durability and long-term efficacy of coiled aneurysms have been questioned [20, 27], and it is why researchers are exploring bioactive stent technology.

2.2.2 Clip Ligation as Alternative to Coiling

Clip ligation is the other option to endovascular coiling and is a surgical procedure where, under general anesthesia, the surgeon removes a section of skull (craniotomy) and exposes the aneurysm [41–43]. As illustrated in Figure 2.5, a metal clip is placed across the neck of the aneurysm sac so that the neck is closed and cut off from the connected blood vessel [13, 41]. In one large study, the mortality rate from the clipping of unruptured aneurysms ranged from 2.6-10.9% [3, 44]. Some of these risks overlap with those seen in open surgery and others are unique to endovascular therapy. In one study, Murayama *et al* described procedural complications in 69 patients (8.45%) - the most common being thromboembolism in 24 patients (2.4%) [27]. In the 1960s, a study was performed on randomized trials that showed the benefits of clipping, including the

craniotomy, outweighed the risks in some circumstances [36]. Later, Fridriksson *et al* stated that in some studies, the mortality rates correlated to the number of craniotomies performed for the treatment of aneurysms. In one study cohort, he found that devastation from the first bleeding episode was the main cause of overall morbidity in 156 of the 355 (44%) surgically treated patients. In addition, postoperative complications such as septicemia, meningitis, thromboembolism, and myocardial infarction, occurred in 59 patients which accounted for a poor outcome in 8 (2%) of those 355 cases [38]. Given the statistics of both the coils and the clipping methods of aneurysm management, it is clear that another approach should be investigated. Like coiling, the installation of a bioactive stent would not require a removal of a portion of the skull, but unlike coiling there would not be a risk of coil embolization. Such a device would allow the body to heal not only the weakened blood vessel, but also occlude the aneurysm neck safely and effectively. Foundational studies of a bioactive stent should begin with the design of a two-dimensional model that may provide preliminary data about how cells and fluid flow can react within an artificial aneurysmal environment. Lab-on-a-chip technology lends itself very well to these types of experiments.
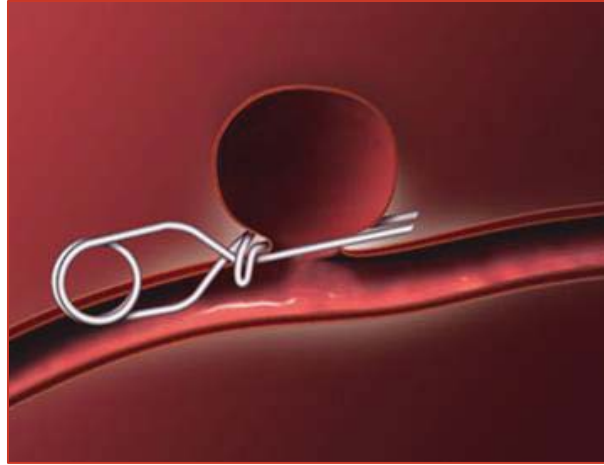
Figure 2.5. Illustration of endovascular clip ligation (clipping) of a cerebral aneurysm
(Endovascular Coiling, Johns Hopkins Medical Center; 2012).

2.2.3   Bioactive Stents for Aneurysm Treatment

The market for bioactive stent technology stands around $5 billion in 2010 in the United

States alone [39]. One reason is that balloon angioplasty has been associated with high

failure rates while restenosis (recurrent narrowing of an artery after successful dilation)

remains another problem with bare (uncoated) metal stents [33, 34]. Patency with bare

stents usually fails because of intimal hyperplasia throughout the stented region [41].

Acute inflammation, chemokine release, and oxygen free radicals occur in the wall

adjacent to the abluminal wall [41] make blood vessel wall healing very difficult.

Slaikeu *et al* submitted a patent application in 1999 for an implantable medical device

assembly suitable for stenting. The patent application proposed to have a stent device

guided by a microcatheter to track bioactive coils to the aneurysm site, as is the norm.

The difference was that the stent device would be partially coated with "a covering

causing an angiogenic response" to aid in the promotion of blood vessel growth at the

aneurysm neck [42].

Another type of bioactive stent that is undergoing effective study is the drug eluting stent device. Drug-eluting nitinol stents have been assessed as an approach to improve patency and generally contain antimitotic drugs as well as Serolimus (an immunosuppressant drug) and heparin (an anticoagulant) [41], to reduce the risk of intimal hyperplasia. Further, drug-eluting stents have yielded lower restenosis and revascularization rates [43]. While the future is wide open for the optimal development of drug-eluting stents, bioactive stents hold the promise of improving clinical outcomes by enhancing device integration with the surrounding biological environment [30]. Ultimately, the bioactive stent would have a coating that would display relevant biomimetic ligands to entice adhesion of endothelial cells (EC), reduce inflammation, prevent thrombosis and thus increase healing. For example, one study used CD34 antibody to coat the stent surface so as to recruit circulating endothelial progenitor cells (EPC) from the bloodstream to accelerate the healing process [30]. The deterrent here, is that the CD34 antibodies not only can attach to EPC but to other progenitor cells as well, including smooth muscle stem cells which can exaggerate restenosis [30]. A peptide sequence of arginine-glycine-aspartic acid (RGD) [37, 38] has been used as an integrin binding motif to promote EC adherence and migration, but studies have shown that cardiovascular use of this peptide has not been favorable [28, 39, 40].

One design of a bioactive stent device involved a standard stent that was intertwined with a novel biomaterial called bacterial nanocellulose (BNC). Unlike RGD, the BNC allows cells to easily bind to it and settle down. BNC is porous and can be rendered magnetic so

that it may attract magnetically-labeled cells to itself. Figure 2.6 shows a diagram of an early basic design of the proposed bioactive stent system.
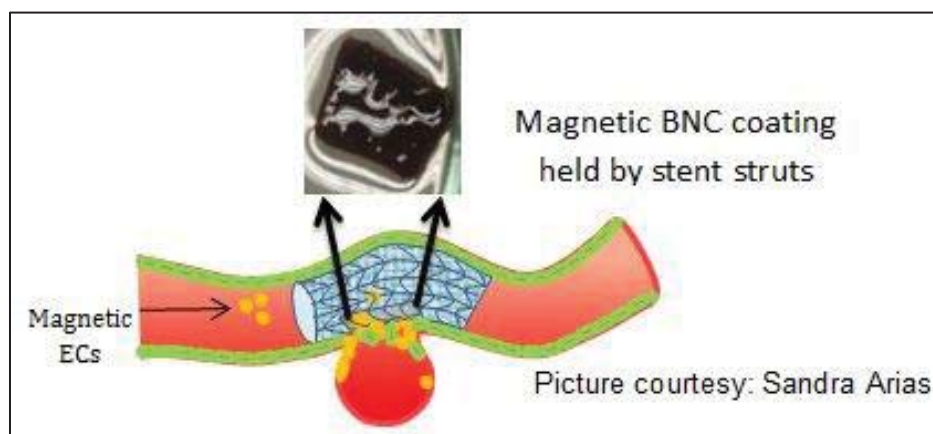
Figure 2.6. Cartoon showing piece of magnetic material (magnetic bacterial nanocellulose) forming a nidus at neck of the aneurysm. Magnetic EC would flow through microchannels to nidus to begin proliferation across neck. (Figure courtesy of Sandra Arias for presentation to Dr. Jean Paul Allain, 2012).

It is important to note that the AOC is a microfluidics device and thus is quite different than the model illustrated in Fig. 2.6. Part of this thesis research was to determine if the materials used in the proposed bioactive stent device would be compatible with human cells, and that the materials utilized would be able to promote cellular growth and be able to attract magnetically-labeled cells. Further, the synthesis of the biomaterials had to be optimized before the realization of a prototype bioactive stent was accomplished. The preparatory work needed for the static bioactive stent device was very necessary and pertinent. The biomaterials, PDMS and BNC/MBNC, could be used in the dynamic AOC to analyze fluid flow in future studies.

2.3   Aneurysm-on-a-Chip™ Design

Cells are subject to multiple cues in their environment, including gradients of cytokines, secreted proteins from neighboring cells, biochemical, and mechanical interactions with the extracellular matrix (ECM), and direct cell-to-cell contacts [39, 46–48]. One engineering process called soft lithography [39, 47–49], has put microfluidics within the reach of biology-focused academic laboratories [49] and holds great promise for the creation of advanced cell culture models [52] for the derivation of the relation between cell migration and growth factors [44]. Lab-on-a-chip devices or "micro-total-analysis-systems" (µTAS) create microsystems incorporating several steps of an assay into a single system [53]. The small footprint and low power consumption of integrated systems creates opportunities for portable, point-of-care devices that can perform analyses hitherto possible only in the research laboratory on a macro scale [47, 51, 52].

The field of microfluidics dates back to the early 1950s when efforts were performed to dispense small amounts of liquids in the nanoliter range that provided the basics of ink-jet technology [55]. However, in this engineering arena, there is nothing in the literature that describes the generation of an aneurysm-on-a-chip *in vitro* culture model though there are many studies that have involved organ-on-a-chip systems. Examples of organs-on-a-chip are the gut chip [54], breast chip [54, 55], liver chip, kidney chip, lung chip, and the body chip [57]. To understand this technology, it is prudent to first distinguish the two main features that a lab-on-a-chip *in vitro* model should include: (1) biocompatibility, and (2) biodegradability. A lab-on-a-chip device must satisfy these two requirements so that cellular studies can successfully be conducted. Secondly, after a suitable material is

chosen, the specific cell type that will satisfy the ultimate *in vivo* model conditions must

be selected and tests must be performed to ensure that the cells will survive in the

presence of the selected material as well as proliferate and survive on the material

surfaces. Apoptosis assays, cytoskeleton labeling, migration assays, identification of

certain adhesion molecules, and cell proliferation assays can be employed to elucidate the

possible mechanisms responsible for successful cellular activities [39, 56]. In summary,

Figure 2.7 shows the guiding principles and practical issues surrounding the generation of

a successful μTAS system [59]. This was the basic algorithm set used to generate the

Aneurysm-on-a-Chip™ model. Using this paradigm, the 2D device used two

biomaterials: one was used to generate the microfluidics channels that mimic blood

vessels and the aneurysm sac, the second substance was generated to ultimately form a

magnetic interface between the support framework and magnetically enhanced HASMC

to allow cell proliferation across the aneurysm neck to seal that opening.
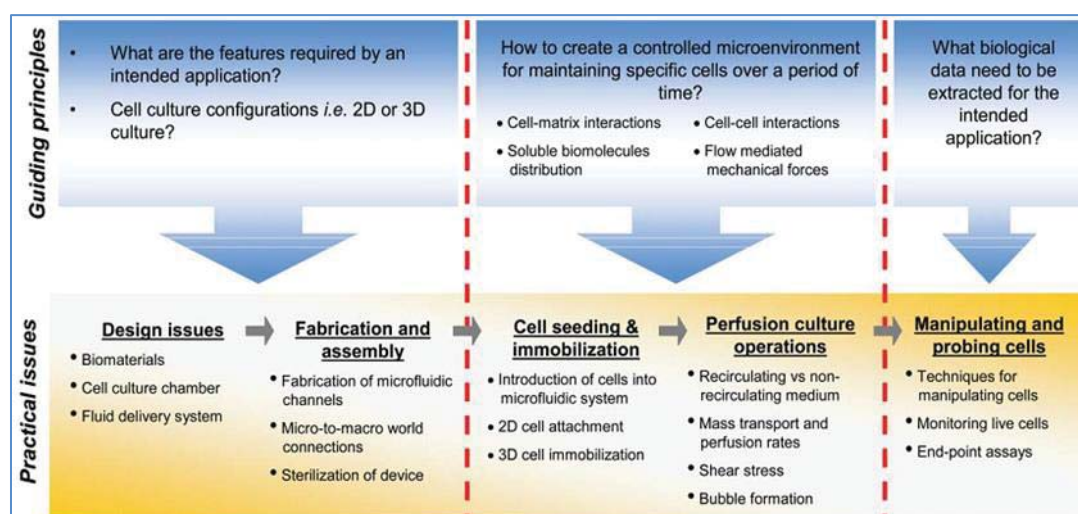
Figure 2.7. Guiding principles and practical issues for robust operation of a microfluidic perfusion culture system [42].

2.4   Characteristics of Biomaterials

Biocompatible materials (or "biomaterials") research is an exciting discipline which has

steadily grown over its approximate half century of existence [58, 59]. Williams defined

a biomaterial as a nonviable substance used in a medical device intended to interact with

biological systems [58, 59]. By definition, the goal of early first-generation biomaterials

was to achieve a suitable combination of physical properties to match those of a living

host [45, 47, 56]. The second generation of biomaterials was designed to produce a

controlled action and reaction in the physiological environment while retaining the

virtues of the first-generation biomaterials. It should be recognized, however, that living

tissue responds to external stimuli and adapts to them, while synthetic materials do not.

Thus, improvements of first- and second-generation biomaterials are limited since man-

made products used for repair/restoration of living tissue represent a compromise [60].

This particular shortcoming limits the lifetime of such devices made with these materials

and presents a challenge for the third generation of biomaterials [59, 61]. Nonetheless,

there are a number of biomaterials in use regularly *in vivo*. As seen in Table 1, examples

of biomaterials include manmade "organoapatites" (e.g., hydroxylapatite) for use as

human artificial bone [59, 62], titanium, stainless steel, poly(methyl methacrylate)

(PMMA), Dacron, Teflon, polyurethane, cellulose, hydrogel, and platinum for

applications involving the skeletal system, the cardiovascular system, and other organs

[61].

For *in vivo* usage, it is important for a material to degrade safely over time after the tissue

has healed and the device is no longer needed [39]. To satisfy this criterion, synthetic

rubber substances, called elastomers have emerged. Further, there are three classes of biodegradable elastomers that have been reported thus far: (1) hydrogels, (2) elastin-like peptides or polymers, and (3) polyhydroxyalkanoates (PHA) [62, 63]. Hydrogels are hydrophilic polymer networks that absorb up to thousands of times their dry weight in water, are chemically stable and biodegradable; in other words, they can degrade, disintegrate, and dissolve [64–67]. In addition, a hydrogel environment is able to protect cells and fragile drugs *in vivo*. Other advantages of hydrogels are that they can easily be modified with cell adhesion ligands, and can be injected *in vivo* as a liquid that gels at body temperature. While hydrogels are able to protect delicate drugs, disadvantages of this type of material include difficulty loading drugs and cells into the material initially, and it is difficult to crosslink the biomaterial as a prefabricated matrix *in vitro*. Of critical importance too, is that hydrogels are not easy to sterilize [67].

Table 1. Applications of synthetic biomaterials and modified natural materials in medicine (adapted from Ratner, Biomaterials Science: A Multidisciplinary Endeavor, 2004) [61].

Application	Types of Materials
Skeletal system (joint replacements, bone plates, bony defect repair)	Titanium, stainless steel, PMMA, hydroxylapatite, Teflon, Dacron
Cardiovascular system (blood vessel prosthesis, heart valve)	Dacron, Teflon, polyurethane, stainless steel, silicone rubber
Catheter	Silicone rubber, Teflon, polyurethane
Organs (artificial heart, skin repair template, artificial kidney)	Polyurethane, silicone-collagen composite, cellulose polyacrylonitrile
Senses	Platinum electrodes, hydrogel, collagen, PMMA, silicone-acrylate

With their difficulty to successfully retain drugs or crosslink them into the matrix, coupled with the problem to render this material sterile, hydrogels are not suitable for a magnetic AOC design. An alternative to hydrogels includes a family of biodegradable elastomers called elastin-like polymers (ELP) that have been used in many different approaches for controlled drug delivery [70] and are made of repeated sequences found in the mammalian elastic protein, elastin - an extracellular matrix protein that confers extensibility and elastic recoil to large human blood vessels, lung, ligaments, and skin [71]. The Fidkowski group has actually developed a novel biodegradable and biocompatible ELP, poly(glycerol sebacate) (PGS), that matches the mechanical properties of veins [63, 70]. They state that PGS causes no chronic inflammatory response when implanted into live animal models and they have shown that endothelial cells adhere and proliferate on unmodified PGS surfaces [72]. Using soft lithography methods, this lab team has successfully developed a lab-on-a-chip PGS capillary network where part of the lumens has been covered by EC [72]. The drawback in implementing this remarkable material for an Aneurysm-on-a-Chip™ apparatus is that it is not commercialized yet and therefore cannot be purchased.

PHA, the final category of biodegradable elastomers, are polyesters produced under unbalanced growth conditions by microorganisms, and accumulate intracellularly in the form of storage granules [67, 69, 71–73]. These materials are thermoprocessable (they can be sterilized by autoclaving) and have been used to coat medical devices to improve biocompatibility [69] including sutures, guided tissue repair/regeneration devices, bone marrow scaffolds, and wound dressings [69, 71]. As attractive as these materials are, the

production cost is the main commercialization-limiting step arising from the cost of the

fermentation substrates and the extraction from the microbial cells [73]. Nevertheless,

PHA remain appealing because the degradation rate of these materials can be modified

and controlled by altering the porosity thereby increasing the surface area [69] – obvious

advantages for drug elution and delivery.

For the AOC 2D model, it should be emphasized that while biocompatibility is required,

biodegradability is not. Therefore, the first biomaterial formed microfluidic channels in a

chip to mock blood vessels as well as mimic different aneurysm forms. One type of

substance that can be coated and utilized for this model is polydimethylsiloxane (PDMS).

For example, there have been studies that have shown PDMS successfully enhanced the

growth of human mesenchymal stem cells (hMSC) and induced neural-like cell

differentiation [76] in a 2D environment. PDMS has therefore demonstrated to be a

suitable biomaterial for μTAS experiments and was the choice material for the

microfluidic chip AOC mechanism. Interestingly, there are other appealing qualities of

this biomaterial that should be discussed further.

2.5   PDMS – Choice Material for BioMEMS Device

PDMS is a liquid bi-component silicone biocompatible pre-polymer (basically

transparent rubber [51]) that, when mixed with a cross-linker agent, becomes

polymerized and rigid. It is by far the most commonly employed material for

microfluidic cellular behavior studies [59] due to its adaptability in being a good

substrate for cell growth, proliferation and differentiation, and for its mechanical stability,

biocompatibility, and non-toxicity [47, 49, 74, 75]. Its rigidity can be controlled by varying the amount of the cross-linker agent concentration as well as the temperature and time of baking (curing) [77]. Further, PDMS can be engineered with different shaped structures on which cells may be cultured [49, 54, 57, 74] thus any size or shape of microfluidic channel can be created. Other advantages of PDMS are rapid prototyping, cost-effectiveness, ease of visualization (100% optically transparent), good gas-permeability, it is autoclavable, and it possesses excellent adhesive properties to glass and other substrates [49, 57, 76]. PDMS is also inherently hydrophobic, so biocompatibility enhancements must be made via surface modifications [57, 73] so that cellular attachment may be achieved. Makamba *et al* summarized seven major techniques for surface augmentations [75, 76]:

1) Modification by exposure to energy,

2) Covalent modification,

3) Chemical vapor deposition,

4) Phospholipid bilayer modification,

5) Protein modification.

Once PDMS is rendered hydrophilic, then cells can be introduced to this material for growth studies. To illustrate, PDMS bioreactors can be fabricated for perfusion culture of mammalian/human cells. Examples of cell cultures in such a µTAS system are the cultivation of fetal human hepatocytes, mouse osteoblastic cells, and human breast cancer cells [54, 76], in addition to the hMSC [76] mentioned earlier. Table 2 shows a comparison of properties of the more common materials used in microfluidic systems [59]; hence it must be stated that there are other materials and polymers suitable for the

culture of cells such as PMMA, silicon, and polysulfone. Given the characteristics in the red rectangle of Table 2, it is easily understood that PDMS is the only biomaterial that lends itself to the requisites for the Aneurysm-on-a-Chip™ because its main traits are transparency, biocompatibility, and sterility. Likewise, it is significant to observe that PDMS is fabricated by means of soft lithographic procedures [51] – fabrication processes that are necessary for the proper generation and development of a lab-on-a-chip device but do not require expensive microelectronics fabrication, injection molding, or laser photoablation that must take place inside of an even more expensive cleanroom laboratory.

Thus far, the AOC *in vitro* model design is two-dimensional, utilizing PDMS as the biomaterial of choice to mimic blood vessels and an aneurysm. The second material to discuss in this review is that of the scaffold upon which cells need grow. The ability to control the placement of cells in an organized pattern on a substrate is desired for tissue engineering applications [79]. One biomaterial that lends itself particularly well to this purpose is bacterial nanocellulose (also known as microbial cellulose) can be rendered magnetic to attract human endothelial cells and help to begin proliferation.

Table 2. Common biomaterials used for fabrication of microfluidic networks in microfluidic perfusion systems (adapted from Slaiku *et al*, 2001) [42].

| Materials | Fabrication techniques | Properties relevant to microfluidic perfusion culture systems | | | | | Examples of microfluidic perfusion systems |
		Visible light transmittance[a]	Autoclavable[b]	Water diffusion coefficient[c] $\times 10^9/m^2\ s^{-1}$	Gas permeability[c] $\times 10^{10}/cm^3$ (STP) cm (cm^2 s cm Hg)$^{-1}$	Young's Modulus[d]/GPa	
Poly(dimethylsiloxane) (PDMS)	Soft lithography	Clear	Yes	3–6 (Heo *et al.*[35])	N$_2$: 280 CO$_2$: 340 O$_2$: 600 (Mark[39])	3.6×10^{-4}–8.7×10^{-4} (Armani *et al.*[40])	12, 13, 18, 19, 21, 22, 41–43
Silicon	Micro-electronics fabrication	Opaque	Yes	N/A	N/A	165 (Dolbow *et al.*[44])	45, 46
Glass	Micro-electronics fabrication	Clear	Yes	N/A	N/A	63–73 (Smith[47])	15, 48
Poly(methyl-methacrylate) (PMMA)	Hot embossing, injection molding, laser photoablation	Clear	Yes	0.002 (Rodriguez *et al.*[38])	N$_2$: 0.039 CO$_2$: 0.78 O$_2$: 0.23 (Nakai *et al.*[49])	3.3 (Brandrup *et al.*[50])	14, 51
Polysulfone	Hot embossing, injection molding, laser photoablation	Clear	Yes	0.009 (Schult *et al.*[52])	N$_2$: 0.2 CO$_2$: 8 O$_2$: 1.5 (Hu *et al.*[53])	2.47 (Brandrup *et al.*[50])	54

[a] Affects compatibility with live-cell imaging during microfluidic perfusion culture. [b] Sterilization of microfluidic perfusion culture system at 121 °C, 20 min. [c] Affects culture conditions within the microfluidic perfusion culture system. [d] Elasticity affects chip-to-world interface and integration of other microfluidic components *e.g.* valves.

2.6   BNC – Choice Material for Bioactive Stent

Cellulose is a linear polymer of glucopyranose sugar molecules, and synthesized by both plants and bacteria. Different types of microorganisms generate this biomaterial: algae (Vallonia), fungi (Saprolegnia, *Dictystelium discoideum*), and bacteria (Acetobacter, Achromobacter, Aerobacter, Agrobacterium, Pseudomonas, Rhizobium, Sarcina, Alcaligenes, Zoogloea), but not all of these entities can secrete the synthesized cellulose as fibers extracellularly [80]. One such species of bacteria, *Gluconoacetobacter xylinum*, was first described by Brown in 1886 where he identified a gelatinous mat, formed in the course of vinegar fermentation on the surface of the growth broth, as a chemical equivalent to cell-wall cellulose. In other words, *G. xylinum* produces extracellular cellulose in the form of pellicles (gelatinous mats) at the air/liquid interface of the culture medium in static culture [80] now known as bacterial nanocellulose (BNC).   BNC contains fibers with high strength and high crystallinity and is also biocompatible and biodegradable. It is commonly used in surgical applications such as tissue implants for

the abdominal wall, skin, subcutaneous tissue, organs, the digestive tract, and cartilaginous tissue [78–80]. In fact, results of various studies indicate that topical applications of BNC membranes like the commercial preparation called Biofill, improve the healing process of burns and chronic wounds [83].

In the development of both the bioactive stent and any microfluidics system, it is understood that cells need to be placed on a scaffold that gives them structure before they can be coaxed into proliferation and ultimately form tissues [84]. Cells are able to sense substrate texture by changing their morphology, cytoskeleton configuration, and intra- and extracellular signaling [44]. BNC is an excellent substance that can act as a framework since it resembles electrospun collagen and has remarkable biocompatible properties [85–87]. In one study, the RGD peptide was added to dry BNC grafts by incubating the BNC for 24 hours at room temperature. The resultant BNC pieces were thus able to promote the enhancement of endothelial cell growth [86]. Bacterial nanocellulose also has a very unique surface roughness due to the fibril lattice and the porous nature of the arrangement of the fibers [88]. The porosity consists of both micro- and nanoporous spaces, which can house a variety of particles such as magnetic nanoparticles. The cellulose fibrils can act as templates for the non-agglomerated growth of ferromagnetic nanoparticles [89].

2.7   HASMC – Ideal Cells for Bioactive Stent and AOC Prototypes

The cellular model for this research should mimic closely the microenvironment within a human or animal body and as a result, smooth muscle cells are the logical choice for the

aneurysm-on-a-chip apparatus. Smooth muscle cells (SMC) are the major cell type in the

tunica media and are widely used in the Tissue Engineered Blood Vessel (TEBV) field

[86–88]. It has also been shown that these cell types have successfully been cultured for

up to 8 weeks on BNC pellicles according to results from the alamarBlue® assay [90].

SMC are able to proliferate and develop a high number of cells, however, when

implanted into a host, a quiescent, differentiated and contractile phenotype is preferable

[86, 88]. Vascular smooth muscle cells cultured *in vitro* typically revert from a

contractile phenotype to a synthetic phenotype. Pulsatile strain and shear stress stimulate

vascular smooth muscle tissue development and induce the vascular SMC to retain the

differentiated phenotype. This property can be measured by studying α-actin levels

compared to static cultured cells and tissue [86, 89]. Interestingly, Gregory Lanza's

research team found that tissue factor-targeted nanoparticles (NP) could bind with high

avidity to smooth muscle cell membranes *in vivo* [94].

2.8   Various Assays to Identify Cellular Mechanisms

There are three important processes that should be evaluated during the examination of

the static and dynamic bioactive stent apparatuses. These properties include: (1)

cytotoxicity of HASMC by the device materials, (2) migration properties of HASMC,

and (3) F-actin detection of the cells growing on the biomaterials used. Cytoxicity

studies begin with the single cell gel electrophoresis assay (CometAssay®). This is a

state-of-the-art technique for quantitating DNA double strand breaks, oxidative DNA

base damage and repair from *in vitro* samples of cells as a direct result of exposure to a

test material [91].

In order to begin to assess how well these substances perform in recruiting cells, migration studies are carried out to determine how effectively cells travelled and multiplied on those biomaterials. Commercially available cell migration kits are used to assess the distance trekked from the seeding area to the neck region. As seen in Figure 2.8, some common cellular migration assays are: A) Transwell Migration Assay – cells travel through the pores in the membrane, B) In Vitro Wound-Healing Assay – cells are seeded on top of a thin extracellulose matrix (ECM) and a pipette tip is used to scratch the surface to produce a "wound", C) Cell Exclusion Zone Assay – cells are seeded on either side of a barrier which generates a "wound", D) Fence Assay – cells are seeded inside a fence (Teflon ring) where the area outside of the fence is the "wound", E) Microcarrier Bead Assay – cells are bound to carrier beads and migrate off onto the bottom of the well, F) Spheroid Migration Assay – same as the bead assay, but cells are contained within a spheroid and the spheroid with the cells begins to spread out, G) Horizontal Capillary Assay – cells are seeded in a well and move to an adjacent well under a cover slip, H) Capillary Tube Migration Assay – cells (leukocytes) move within a capillary tube [95]. One of the most popular assays, the Transwell Migration Assay, utilizes the Boyden Chamber, where cells are seeded onto polycarbonate filters containing 8 μm pores. The material to be tested is placed outside of these filters and cells migrate through the pores to the material. Distances can be measured and scored and migrated cells can be counted via light microscopy methods [40, 96].

Finally, a measure of cellular adhesion and health is the development of filopodia, which are a cell's main sensory tool. Filopodia have been associated with the sensing of both chemoattractant gradients and topographies of different growth surfaces. Fluorescent phallotoxins may be used to stain filamentous actin bundles that drive the filopodia as the filopodia encounter a chemoattractant (inorganic or organic substance that attracts cells). One of these chemoattractants, actin, accumulates in a direction predictive of a future turn if a cell is to experience contact guidance and adhesion [64]. To assess actin levels during migration, Phalloidin may be coupled to a dye molecule and flow cytometry and confocal microscopy can be used to quantify it [99, 100].
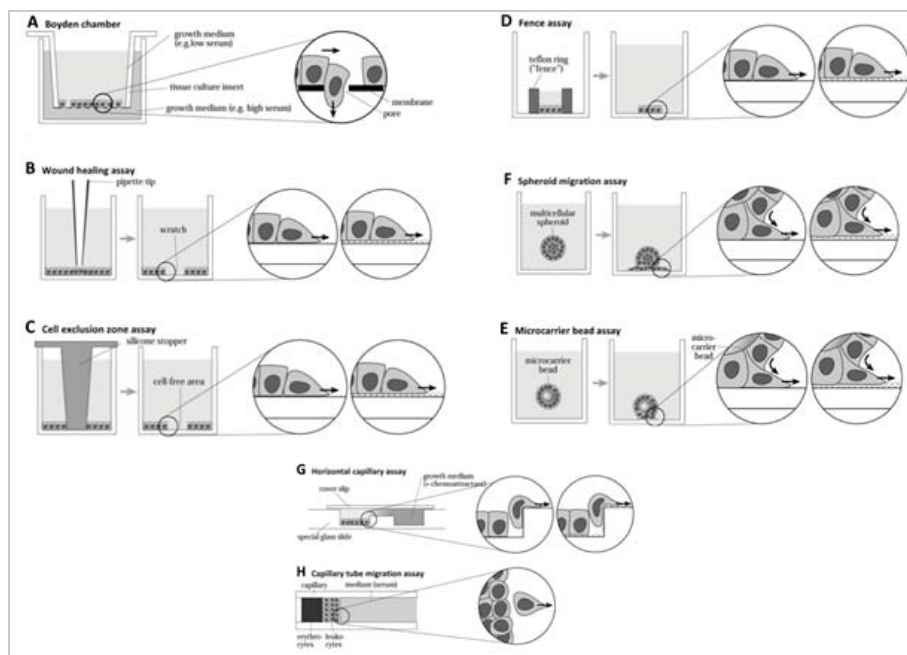
Figure 2.8 [95]. Schema of popular migration assays: A) Boyden Chamber Assay, B) Wound Healing, C) Cell Exclusion Zone, D) Fence, E) Microcarrier Bead, F) Spheroid Migration, G) Horizontal Capillary, H) Capillary Tube Migration

2.9   Hemodynamics and Aneurysm Formation

In order to understand the underlying mechanisms of aneurysm formation, progression, and rupture, studies in hemodynamics (blood flow) and wall shear stress (WSS) can be used to identify the relationships between blood fluid pressures, vascular lesions, and endovascular treatment efficacy [1, 31, 99, 100]. Progress in medical imaging technology and improvements in computer analyses have enabled computational fluid dynamics (CFD) analysis to predict hemodynamics in aneurysms with increased accuracy. Angiography image data can be converted to three-dimension (3D) vessel geometric data for simulations, therefore CFD analysis based on real aneurysm geometry has progressed in recent years [104]. At present CFD is the basic technology used for providing estimations of the hemodynamic flow behavior in IA [106]. While this technology is hopeful, conversely, statistically significant results in patient-specific experiments have not been achieved because the studies in image-guided CFD modeling have been limited to small numbers of aneurysms [105]. Another hindrance in the study of fluid flow was stated by Kumar and Naidu who said that the pulsatile nature of the problem further complicates arriving at a satisfying solution through analytical studies [1]. In spite of the difficulties, CFD data has been obtained in similar patient cases showing that ruptured and unruptured aneurysms had statistically different qualitative hemodynamic characteristics [100, 102]. Each aneurysm explored was found to have its own unique flow pattern, ranging from a simple single repetitive vortex to chaotic changing multiple vortices. Cabral *et al* therefore reasoned that an unstable flow pattern might be associated with aneurysm progression and rupture because of the potential for elevated mean WSS (MWSS) [100, 102]. Further examinations led to the discovery that

concentrated inflow streams and WSS distributions with elevated MWSS and low

aneurysmal viscous dissipation are statistically associated with a clinical history of prior

aneurysm rupture. It was determined that these preliminary results favor theories of

aneurysm progression based on high-flow (high WSS) effects [105]. For a dynamic 2D

Aneurysm-on-a-Chip™ bioactive stent model, there is a simple single inlet (i.e. inlet port)

used with a single outlet port combined with an "aneurysmal sac" between the two ports.

The fluid flow is measured using computational algorithms designed to analyze the flow

of fluid entering the sac, contained in the sac, and exiting the sac. The 2D AOC trial

product was therefore synthesized to be redesignable and modular to provide different

configurations for simulating various aneurysm types and fluid designs.

CHAPTER 3. AIM 1: ENHANCE CELLS AND BACTERIAL NANOCELLULOSE FOR ULTIMATE ATTRACTION TO A STATIC BIOACTIVE STENT

3.1   Introduction

The magnetic protocol for the original bioactive stent was to eventually consist of a

magnetic stent device that would have a magnetic field strong enough to be able to attract

magnetically labeled cells to allow cells to settle down and attach, thus beginning to seal

the aneurysm defect. The first step to realizing this aim was to internalize magnetic

nanoparticles to HASMC thus rendering the cells magnetic. The subsequent step was to

render the BNC magnetic enough to attract the magnetic HASMC. Passive uptake and

electroporation techniques were utilized to label the cells since there are no commercially

available magnetic antibody particles for this cell type, and binding schemes of antibody

to existing nanoparticles, were beyond the scope of this research project. Electroporation

(EP) provided a very effective and rapid method of allowing for the internalization of

particles into a cell after a gentle electric shock, while passive uptake had proven

effective for the internalization of magnetic particles within 24 hours of cell seeding.

Scheme 1 is the description of the magnetic labeling of the HASMC with iron oxide

nanoparticles (IONP) with characterization of biocompatability on the cells after the

process has been performed. Scheme 2 describes the both the synthesis of BNC and

magnetic BNC (MBNC) that culminates in the generation of two static bioactive stents.

In all experiments using cells, Human Aortic Smooth Muscle Cells (HASMC, Cat. #C-007-5C, Gibco® Life Technologies, Carlsbad, CA) were grown under normal culturing conditions ($37.0°C$, 95% air, 5% CO_2) according to the standardized Gibco® protocol (http://tools.invitrogen.com/content/sfs/manuals/HASMC_man.pdf) until the cells reached confluency. Growth medium used was Medium 231 supplemented with Smooth Muscle Growth Serum (SMGS, Cat. #M-231-500, Gibco® Life Technologies). Cells were harvested and density and viability were determined using the Countess® Automatic Cell Counter (Life Technologies, Carlsbad, CA) pursuant to the manufacturer's instructions. HASMC were then seeded for experiments while cells were healthy and in log phase of growth.

3.2   Materials and Methods

3.2.1   Scheme 1: Magnetic Labeling of Cells and Apoptosis Testing

3.2.1.1   Magnetic Tagging of HASMC Via PU

HASMC were first allowed to internalize using the gentle passive uptake (PU) process [40, 50, 101]. Human aortic smooth muscle cells were harvested at a density of $1.0x10^6$ cells/ml with a viability of 87% and seeded in a 6-well tissue culture plate (Cat. #08-772-1B, Fisher Scientific, Hanover Park, IL) at a density of $1.0x10^5$ cells/ml and incubated for 24 hours using different concentrations of 30 nm SPION (Cat. #SHP-30-0010, Ocean Nanotech LLC, Springdale, Arkansas): 6 µg/ml, 8 µg/ml, 12 µg/ml, and 16 µg/ml in nanograde water. The procedure was repeated at least four times to guarantee assay reproducibility. Cells were harvested followed by the evaluation of successful magnetic

labeling determined by scanning electron microscopy (SEM) and Perls Prussian Blue reaction [102, 103].

3.2.1.2   Electroporation of HASMC With SPION

The second method of magnetic internal labeling is via electroporation (EP). It was necessary to determine that the HASMC could survive the EP process, so Trypan Blue Exclusion (Trypan Blue solution, Cat. #C10314, Life Technologies) analyses [104] were executed. To begin with, the EP process was carried out utilizing a BTX ECM 830 Square Wave Electroporator (see Figure 3.1, Genetronics, San Diego, CA), with low voltage and low pulse parameters as illustrated in Table 3 below. Aliquots of 500 µl of cell suspension at a density of 6×10^5 live cells/ml were placed into electroporation cuvettes (refer to Fig. 3.1, Panel A, Cat. #640-45-0126, BTX Harvard Apparatus, Holliston, MA), and pulsed in phosphate buffered saline (PBS) without calcium or magnesium (Cat. #17-516F, Lonza, Walkersville, MD) containing 2 µl of 2 µg/ml SPION. The electroporated HASMC were left undisturbed for 15 minutes after pulsing under normal culture conditions, and then spun down in PBS so as to remove any free nanoparticles (NP). Afterwards, the supernatant was then aspirated, and the cell pellets were resuspended in propagation media, and seeded in a 6-well tissue culture dish (Cat. #07-200-82, Fisher Scientific). Subsequently, the cells were incubated under normal culturing conditions and harvested at 24 h, 48 h, and 120 h time points. The viabilities for each time point were then determined using Trypan Blue.
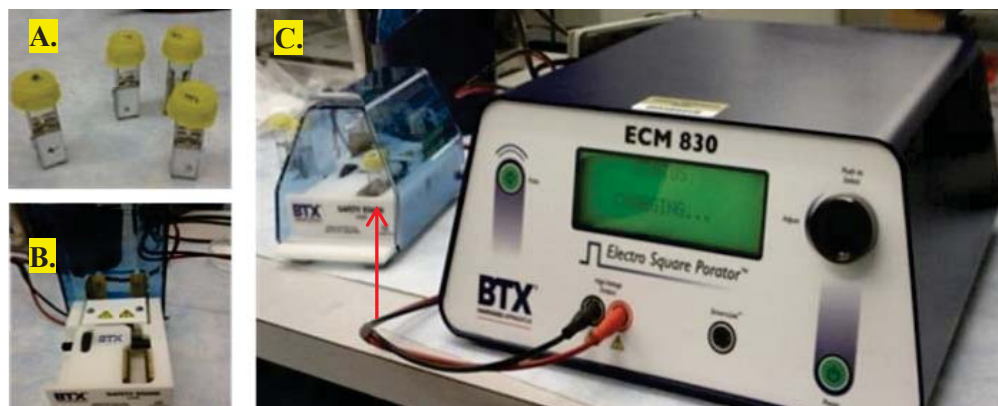
Figure 3.1. Electroporation equipment: Panel A shows sample cuvettes inserted into sample chamber in Panel B. Panel C shows BTX ECM 830 Electroporator controller with samples loaded inside sample chamber (red arrow).

Table 3. Electroporation conditions for HASMC pulsed with SPION for viability determination.

Sample	Field Strength (V/cm)	Pulse Length (µs)	No. of Pulses
1– Untreated Cells	---	---	---
2	500	100	4
3	400	100	4
4	200	100	4
5	200	200	4

3.2.1.3 Determination of Iron Content in HASMC

After magnetic labeling with the SPION, the iron content within the cell samples was

determined. Fe inside of the cells was quantified following the protocol proposed by

Sébastien Boutry *et al* and based on the Perls' Prussian blue reaction [101, 103] whereby

an intense color blue develops with increased iron oxide content . EP was performed at

500 V/cm at 100 µs with 4 pulses for each sample at the following concentrations: 6

µg/ml, 18 µg/ml, 24 µg/ml, and 32 µg/ml. These values were chosen to increase the

number of concentrations to test given the number of cells available. A 96-well tissue

culture plate (Cat. #29442-058, VWR Scientific, Chicago, IL) was used to seed 50 μl of

electroporated cells/well (18 wells for each concentration.) After a 24-hour incubation

period, the cells were washed three times in 300 μl Dulbecco's phosphate buffered saline

(DPBS, Cat. #D8662, Sigma-Aldrich, St. Louis, MO). The cell suspensions were next

incubated overnight at 37°C in 125 μl of 5N HCl (Cat. #9539-03, J.T. Baker,

Phillipsburg , NJ) to induce a more complete acid digestion. The acid was removed and

the wells were washed three times with PBS followed by the addition of 125 μl of 5%

potassium hexacyanoferrate (II) trihydrate (Cat. # P3289, Sigma-Aldrich) was for 15 min.

at room temperature to yield the resultant Perls' Prussian blue reaction. Fe was measured

by the color intensity of Prussian blue in the samples and measured at a wavelength of

630 nm using a microplate spectrophotometer (VersaMax, Molecular Devices, Sunnyvale,

CA). A standard curve was generated to estimate the iron content per cell (analyzed

using a UV/VIS spectrophotometer set at 690 nm (Spectronic GENESYS UV/VIS

Scanning Spectrophotometer, Thermo Fisher, Waltham, MA)) in each of the tested

samples. The equation for the standard curve generation was the following [106]:

$$[Fe] = \frac{(Slope * OD_{690} Labeled Cells + |intercept|)}{\# Labeled Cells} - \frac{(Slope * OD_{690} Unlabeled\ Cells + |intercept|)}{\# Unlabeled Cells}$$

The iron internalized by the HASMC for both PU and EP was quantified using a

microplate reader as described previously. The graph seen in the Results section, Figure

3.13, was generated using the statistical software Origin Pro™ 8.6 (OriginLab,

Northampton, MA). Transmission electron microscopy (TEM) was accomplished on the

samples as well with a FEI/Philips CM-100 TEM system (FEI, Hillsboro, OR).

3.2.1.4 Measurement of Possible DNA Damage by CometAssay®

HASMC was pulsed with commercial SPION and tested for potential DNA damage after

120 h of incubation. The CometAssay® was performed (Cat. #4250-050-K, Trevigen

Inc., Gaithersburg, MD) according to manufacturer's protocols, and populations of

untreated and hydrogen peroxide treated cells were utilized as negative and positive

controls, respectively. The nucleic acid dye SYBR® Green I, was used in this assay to

intercalate to and fluorescently label the DNA contained in the electrophoresed samples.

Cells that do not undergo any DNA damage in the presence of the analyte, will show a

fluorescent round green nucleoid, while DNA damaged cells will have long comets –

positive samples will have nucleoids (the head of the comet) followed by tails which

contain fragmented DNA material (percentage of DNA in the tail). In this experiment,

results were visualized using an epifluorescent Nikon Diaphot microscope (Nikon

Instruments Inc.) at 10X power. The microscope was fitted with a Nikon 990 Coolpix

camera and optical filters optimized for the fluorescent dyes. DNA damage was

quantified using CometScore™ software (Tri Tek Corp., Sumerduck, VA,

http://www.autocomet.com/products_cometscore.php). As can be seen in Figure 3.2,

there are a number of parameters that this software can measure to determine the extent

of DNA damage upon Comet Assay samples.
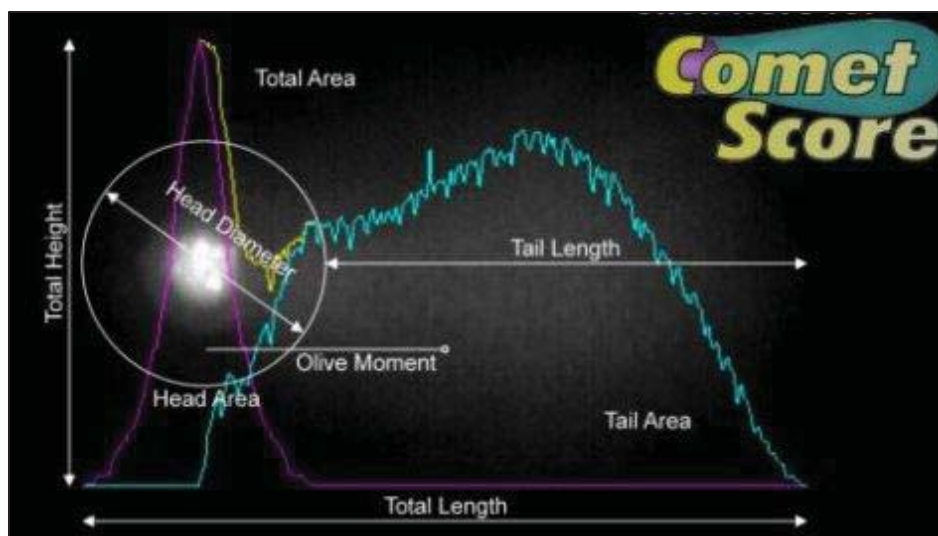
Figure 3.2. Parameters used by Comet Score software program to analyze
Comet Assay Results [107].

The DNA tail (tail length) is the distance of DNA migration from the body of the nuclear

core and is used to evaluate the extent of DNA damage. The Olive Moment parameter is

a measurement of fluorescence intensity corresponding to the amount of genetic material

present in the tail in relation to that found in the comet head and is thus defined as: Olive

Tail Moment = Tail Length x % Tail DNA, where "% Tail DNA" is define by the

fluorescence intensity in the comet tail [108] automatically calculated by the software.

An increased Olive Moment indicates more DNA migration away from the nucleoid head,

and therefore correlates to more genotoxic effects produced by the tested analyte [64].

To evaluate a sample, images are taken of the Comet Assay sample slides and the file is

opened in the software. The user draws a box around the comet that includes both the

head and the tail. A second box is drawn to define the head. The contrast of the comets

to the background is increased by the user and then the software calculates the analysis.

Subsequent paired T-tests were carried out to test for differences between means of the

negative control, test specimens, and the treated control cells (Origin Pro™ 8.6, OriginLab, Northampton, MA).

3.2.2 Scheme 2: Synthesis of BNC/MBNC and Static Bioactive Stent Prototypes

3.2.2.1 <u>Preparation of Standard BNC</u>

BNC pellicles were prepared in-house by culturing the bacterial strain, *Gluconoacetobacter xylinus* (Cat. #10245, ATCC, Manassas, VA). The bacteria excrete the bacterial nanocellulose (BNC) during proliferation and pellicles form at the air-liquid interface of the culture. The shape and size of the pellicle can be controlled by using different growth vessels (i.e. test tubes, flasks). The thickness of the pellicles can be altered by changing the culturing times – the longer the bacteria are allowed to statically grow, the thicker and less porous the pellicles become [82]. First, 500 ml of Mannitol liquid growth medium was made according to ATCC's instructions (2.5 g Yeast Extract (Cat. #Y1625-250G, Sigma-Aldrich), 1.5 g Bacteriological Peptone (Cat. #P0556-1KG, Sigma-Aldrich), 12.5 g D-Mannitol (Cat. #M120-500, Fisher Scientific), and a volume amount of nanograde water) and autoclaved. Next, 500 ml of Mannitol agar was made (same recipe for the liquid medium but with the addition of 7.5 g Bacteriological Agar (Cat. #A5306-250G, Sigma-Aldrich)) and autoclaved. After the agar was allowed to cool to 56°C in a water bath, agar plates (Petri Dish, Cat. #89038-968, VWR Scientific, Chicago, IL) were aseptically poured and allowed to solidify. The solid plates and liquid media were stored at 4°C until needed.

Synthesis of the BNC pellicles began with the preparation of the primary bacterial culture whereby 5 ml of liquid Mannitol medium was aseptically placed in a 14 ml sterile culture tube (Cat. #60818-725, VWR Scientific). This size of culture tube has an outer diameter of 17 mm, which yields that size of BNC pellicle. The media was inoculated by aseptically scraping some frozen bacteria and mixing the inoculum into the media and vortexing briefly. This culture was allowed to statically grow (no aeration or shaking) in an incubator set at 30°C for 24 hours. Even though a very small fragile pellicle formed at the liquid-air boundary, this was not needed and was discarded. For stock *G. xylinus* bacterial plates, a loopful of the fresh bacteria was obtained aseptically from the 24-hour culture and used to streak a Mannitol agar plate. This was repeated until several plates were streaked. All inoculated plates were incubated for 72 h at 30°C until small round whitish colonies were visible. From a stock plate, two or three single colonies were aseptically picked to inoculate a fresh tube of 5 ml of liquid Mannitol media and this culture was allowed to grow statically for 72 h at 30°C. Several tubes were inoculated to provide several pellicles. The resultant pellicles were lifted out of the media and treated with 1N NaOH (sodium hydroxide) solution at 80°C for 1 h to kill any live bacteria. The pellicles were then rinsed at least 3 times with 20 ml sterile nanograde water to remove the dead bacteria. Pellicles were rinsed two more times with 20 ml sterile PBS to bring the pH toward 7.0 and they were allowed to remain in 5 ml fresh sterile PBS at room temperature until ready for analysis or for use with cellular experiments. Figure 3.16 in the Results section shows an example of a BNC pellicle (see red arrow) in Mannitol medium.

3.2.2.2 Preparation of Magnetic BNC

3.2.2.2.1 Magnetic Nanoparticle Synthesis Reaction

It was thought that if the BNC could be rendered superparamagnetic and placed at the

neck of the aneurysm, then magnetically-labeled stem cells, smooth muscle cells, and/or

endothelial cells could be attracted to the neck region so as to attach to the material to

begin to close off the aneurysm. With this in mind, the BNC needed to have iron oxide

nanoparticles (IONP) impregnated into it, and the only way to accomplish this was to

first synthesize the IONP. The creation of such nanoparticles was accomplished by the

optimized coprecipitation reaction of the iron oxide NP into the existing BNC matrix.

The chemical equation for the reaction is:

$$FeCl_2 \cdot 4H_2O + 2FeCl_3 \cdot 6H_2O + 8NH_4OH \rightarrow Fe_3O_4 + 8NH_4Cl + 20H_2O \text{ [109]}.$$

The reaction set up is seen in Figure 3.3. Into a 250 ml three-necked glass round-bottom

flask (Fig. 3.3.A, Cat. 89090-808, VWR Scientific), containing 50 ml nanograde water.

Under stirring conditions, 1M solutions of iron (III) chloride hexahydrate (FeCl$_3$•6H$_2$O,

Cat. #236489-5G, Sigma-Aldrich) and iron (II) chloride tetrahydrate (FeCl$_2$•4H$_2$O, Cat.

#44939-50G, Sigma-Aldrich) were prepared in nanograde water and added to the flask in

a 2:1 stoichiometric ratio: 3.5 ml iron (III) and 1.6 ml iron (II). The reaction mix was

heated gradually at 84°C under a nitrogen atmosphere (to prevent oxidation of the final

product, Fig. 3.3.B) with continued vigorous stirring. The BNC scaffold is introduced

into the reaction mix to promote amalgamation of ferrous ions on the surface of the BNC

fibers. Next, 0.1M ammonium hydroxide (NH$_4$OH, Cat. #318620, Sigma-Aldrich) was

added incrementally to 8.5 ml total to chemically drive the reaction and form magnetite

particles [110] and the entire solution was stirred for 30 min. When the NaOH is

introduced, the ferrous salts begin to precipitate and grow in size. The solution was then gradually heated to 84°C to avoid aggregation of the nanoparticles. After the addition of the ammonium hydroxide, the color of the solution changed from orange to black. The solution was then subsequently heated to 104°C for 1 h to complete the synthesis. The resultant magnetic nanoparticle (MNP) solution was then held in place using a 6 Gauss magnet (check Figure 3.4), after which the reactant mix was decanted to begin the wash steps. The MNP were washed several times with nanograde water by first decanting the supernatant with the magnet in place, followed by removal of the magnet. 200 ml of nanograde water was added to the MNP and the solution was stirred with a plastic 5 ml pipet. The magnet was put back into position to pull the MNP out of solution and the supernatant was decanted again. The process was repeated until the final solution was clear and the pH was near neutral. Dynamic light scattering was used to determine the size of the consequential MNP and the zeta potential was determined using the Zeta Sizer Nano ZS system (Malvern Instruments, Inc., Westborough, MA).
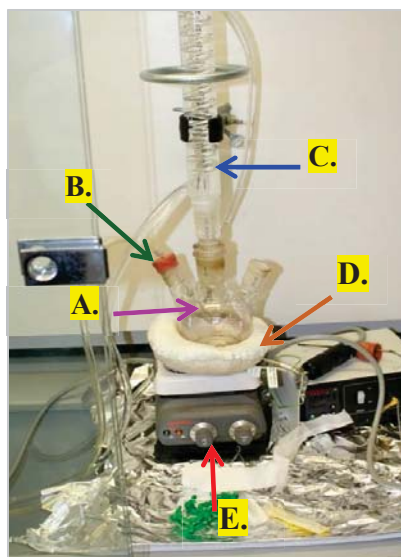
Figure 3.3. Synthesis apparatus for MBNC. (A) 3-necked flask, (B) N_2 gas inject, (C) water-filled condenser, (D) heating mantle, (E) magnetic stirrer/hot plate.
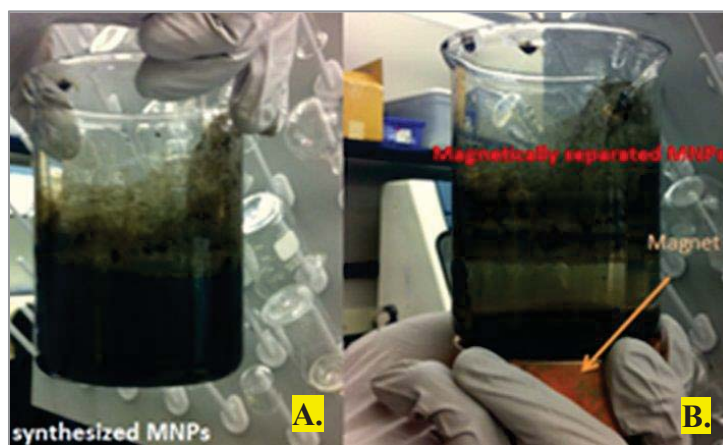
Figure 3.4. Panel A shows the IONP in solution after reaction. Panel B shows how the IONP are easily separated by exposure to magnetic field.

3.2.2.2.2 Generation of MBNC

Once the IONP reaction was optimized and performed, the reaction was set up again, but this time it was to accommodate the addition of BNC. The MNP reaction was carried out the same way as described above, and a new pellicle was grown as depicted. Prior to the addition of the NaOH, the translucent, slimy BNC pellicle was placed into the reaction vessel as seen in Figure 3.5. The NaOH was added incrementally as before and the reaction was carried out. The precipitation of the MNP resulted in complete saturation of the particles into the BNC matrix. The magnet was placed against the 3-neck flask to pull the IONP out of solution. The reaction solution was decanted off and 200 ml of nanograde water was added to the reaction vessel and the magnet was removed to allow the MBNC pellicle to float free. The MBNC pellicle was then removed with tweezers from the 3-neck flask and placed in a glass vial filled with water – this was the first wash. The pellicle was washed several more times with nanograde water until the pH reached neutral, as measured by a pH test strip (Cat. #P4786-100EA, Sigma-Aldrich). The pHed MBNC pellicle was finally removed from the initial glass vial and placed in 5 ml fresh nanograde water at room temperature until ready for experimentation (see Figure 3.6, green arrow points to area of IONP impregnation).

Figure 3.5. BNC pellicle before impregnation of IONP (red circle). Pellicle is clear and slimy before the reaction.
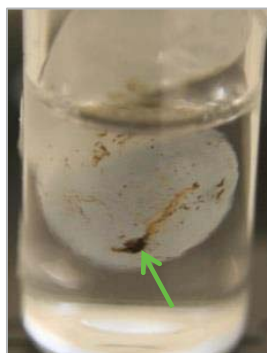
Figure 3.6. Magnetic BNC pellicle resuspended in water. Green arrow points to one area where there are imbedded SPION.

Scanning electron microscopy (SEM) analysis (refer to Figure 3.20) was performed on

the samples in the Life Science Microscopy Facility (LSMF) at Purdue (Purdue

University, West Lafayette, IN) on the Nova NanoSEM™ system (FEI, Hillsboro, OR),

respectively, to show how the SPION attach to the individual fibrils. In order to further

prove that the particles seen in Fig. 3.20, really were iron oxide NP, SEM analysis was

performed on the Phenom ProX Desktop SEM (NanoScience Instruments, Chicago, IL)

that has the capability of simultaneous energy dispersive spectroscopy (EDS) analysis

(see Fig. 3.22). For the Nova NanoSEM system, standard sample preparation techniques

were performed by the LSMF personnel. The MBNC samples analyzed by the Phenom

ProX were air dried inside a biological safety cabinet for 48 h under UV light exposure.

The sample being analyzed was then mounted onto the sample holder (Figure 3.7, red

arrow) for analysis.
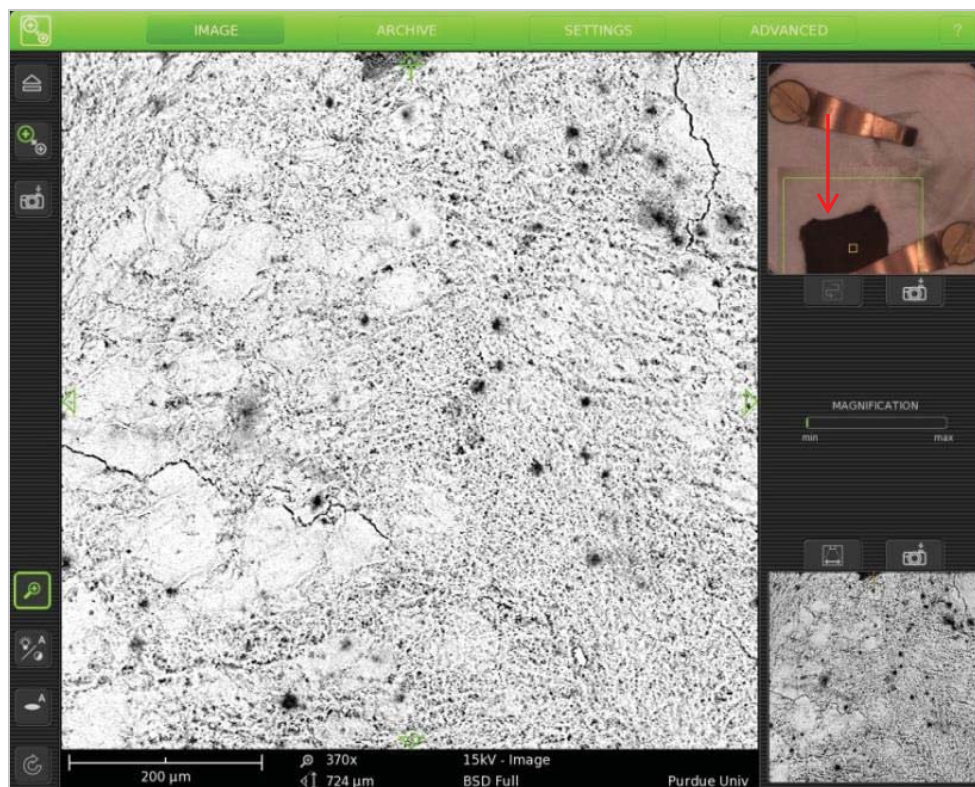
Figure 3.7. MBNC sample under SEM/EDS system. Red arrow points to sample in
sample holder. Black spots on sample are SPION. The scale bar is 200 μm.
It is important to understand that while the BNC itself is biocompatible, the IONP are not.

3.2.2.3   Preparation of Static Bioactive Stents

Nitinol stents were generously provided by Fort Wayne Metals (equal atomic weight

percentage of nickel and titanium, Fort Wayne, IN) on request by PhD candidate, Emily

Walker (School of Materials Engineering, Purdue University, West Lafayette, IN). To

grow a BNC pellicle onto the stent, the stent was first sterilized in an autoclave for 30

minutes. After the stents were allowed to cool, they were placed into a tube of sterile

Mannitol medium. In one tube the stent was oriented horizontally, and in the other tube

the direction was vertical. A loopful of live *G. xylinus* inoculated the media and the tubes

were allowed to grow for 120 h at 30°C. After the incubation period was completed,

pellicles were visible as seen in Figure 3.16 in the Results section.

3.3   Results

3.3.1   Scheme 1: Magnetic Labeling of Cells and Apoptosis Testing

3.3.1.1   Magnetic Tagging of HASMC Via PU

SEM images of magnetic HASMC by passive uptake (PU) shows successful

internalization of the particles within vacuoles as depicted in Figure 3.8, Panel A, blue

arrow. Passive uptake process allowed for the IONP to be taken into the cytoplasm and

engulfed by the vacuole rendering this cell magnetic. The cells successfully took up the

SPION, however, this process was slow. Electroporation offered a quicker method of

magnetic labelling and was included in the research, but optimization of the parameters

had to be performed. Once the method was proven viable for the cells, this was the

preferred method to magnetically tag the HASMC throughout the rest of the study.

Panel A: SPION inside HASMC vacuole
(blue arrow). Scale bar is 0.2 µm.

Panel B: SPION inside HASMC
vacuole. Scale bar is 40 nm.
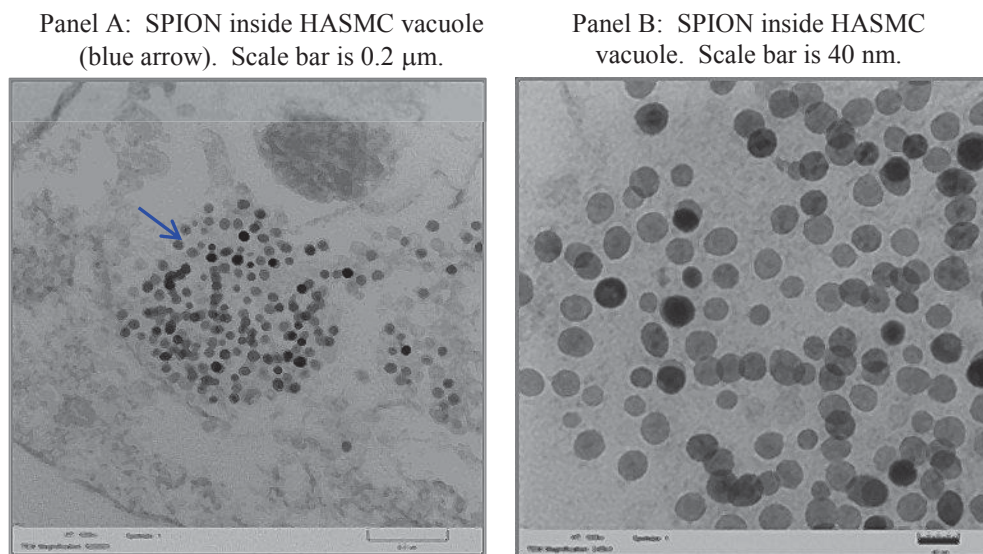
Figure 3.8. SPION internalized by PU into HASMC. Panel A shows SPION within vacuole (blue arrow). Panel B shows close up of internalized SPION.

3.3.1.2   Electroporation of HASMC with SPION

It was important to perform viability counts post electroporation to begin to determine if both the process itself as well as the SPION could be reasonably tolerated by the HASMC. As can be seen from the Trypan Blue Assay viability data in Table 4, all samples at 120 h (120 hours) post EP showed good viability with the highest viability corresponding to 200 V/cm with 100 µs pulses (87.5% viable cells). Upon visual inspection, cells at this time point exhibited healthy monolayers as seen in Figure 3.9 (visual inspection was performed using brightfield illumination with a Nikon inverted Diaphot fluorescent microscope fitted with both 10X and 20X objectives (Nikon Instruments, Melville, NY); images were taken using a Nikon Coolpix 990 digital camera mounted onto the microscope). Looking at the viability data graphically, as seen in Figure 3.10, the higher field strength setting (Sample 2 - 500 V/cm, red diamond) showed

to have the greatest impact on cell viability at 24 hours (~64% viable cells). The cell viability remained above 75% post EP at the 48 hour and 120 hour time points (48h and 120h) as seen in Sample 3 – 400 V/cm, green diamond, Sample 5 – 200 V/cm, light blue diamond, and Sample 2, red diamond. Sample 4 (200 V/cm, 100 µs pulses, light blue diamond) dramatically increased over the three days from the 48 h time point. A more gradual increase was observed for Sample 3 (green diamond) over the same time period, while Sample 5 (light blue diamond) held viability at ~83% for the same time period. Both the Sample 2 (red diamond) and the untreated control (Sample 1 – black diamond) decreased over this time window. These inconsistencies show why it is important to optimize this system to achieve the best electroporation conditions to maximize the SPION uptake while keeping the cells as viable and healthy as possible. Having stated that, the up and down trends seen in the electroporated samples can be accounted for by the recuperation period needed for the cells after EP, and that the Trypan Blue dye may be leaking out during that recovery time. For these experiments, the take home message is that at the end of a 5-day growth period, post EP, the HASMC were growing very well and tolerated the EP process.

Panel A: Negative control
Panel B: 500 V/cm, 100 μs
Panel C: 400 V/cm, 100 μs
Panel D: 200 V/cm, 100 μs
Panel E: 200 V/cm, 200 μs
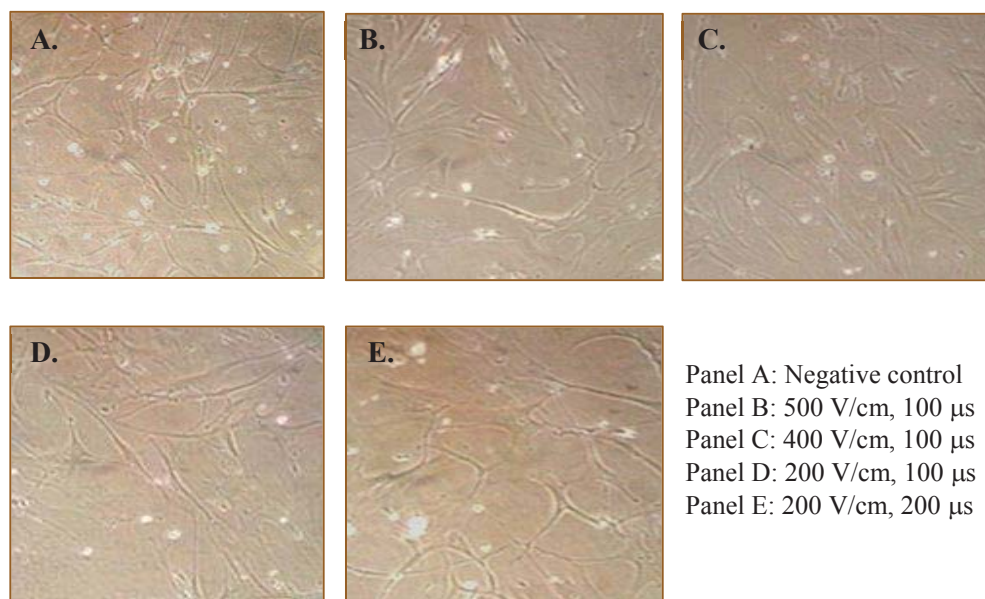
Figure 3.9. NP-seeded HASMC at 5 days (120 h) post EP with SPION: Panel A. Untreated HASMC. Panels B, C, D, E are HASMC at 120 h time point. For all parameters, cells look visually healthy.

Table 4. HASMC Cell Viabilities at 24 Hours, 48 Hours, and 120 Hours Post Electroporation.

Sample	Viability (%)		
	24h	48h	120h
Sample 1– Cells untreated (Negative Control)	76.33	88.50	80.67
Sample 2– 500 V/cm, 100 μs	63.67	83.50	78.33
Sample 3– 400 V/cm, 100 μs	79.00	77.83	82.67
Sample 4– 200 V/cm, 100 μs	85.50	72.00	87.50
Sample 5– 200 V/cm, 200 μs	79.00	82.00	82.00
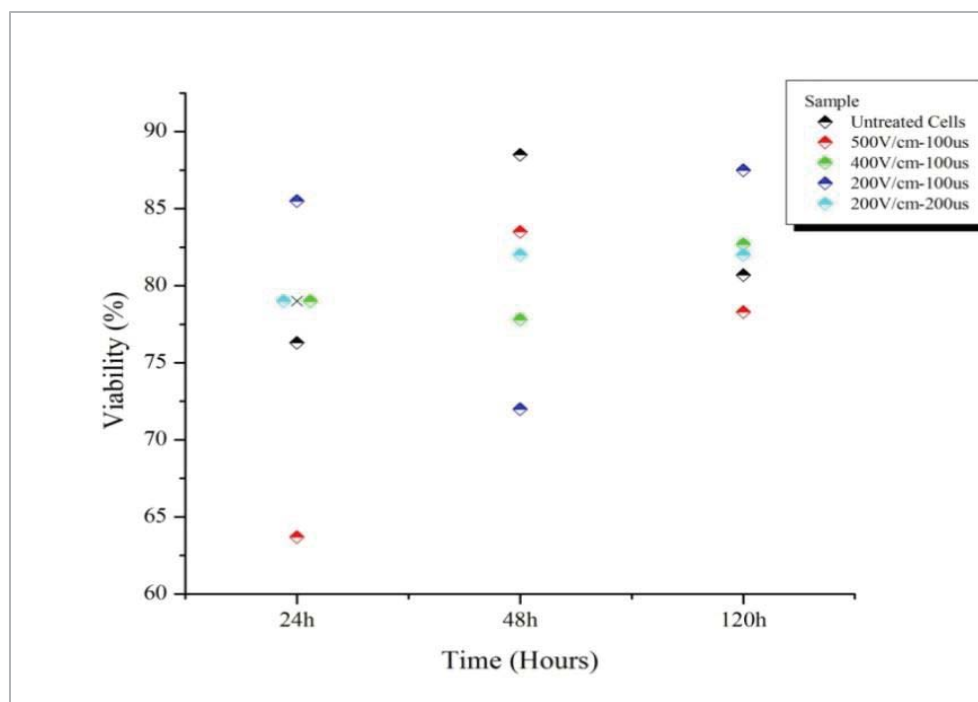
Figure 3.10. HASMC viabilities at 24 h, 48 h, 120 h post EP with SPION. All treated cells are ~77% viable and above at 120 h time point.

3.3.1.3   Determination of Iron Content in HASMC

A standard curve was generated first with which to compare the samples (refer to Figures 3.11 and 3.12). Figure 3.11 shows the Prussian blue staining standards and the increase in blue color which directly corresponds to the iron content within the samples. Four concentrations of iron oxide were employed to generate the standard curve. Iron content was calculated per the equation given in the Materials and Methods section for the Perls Prussian Blue reaction and tabulated for both PU and EP HASMC samples. Results were tabulated as seen in Table 5.
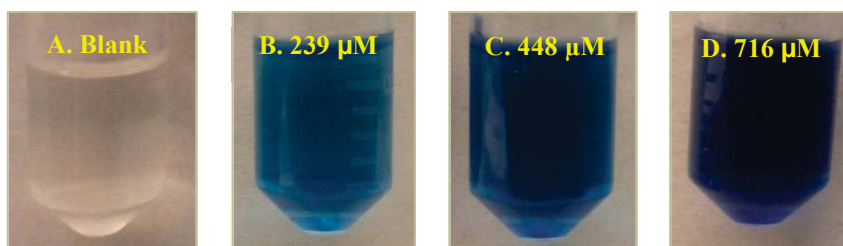
Figure 3.11. Perls Prussian Blue staining for different concentrations of iron oxide digested in 300 µl of acid. Panels A through D show the blank through the highest iron concentration.
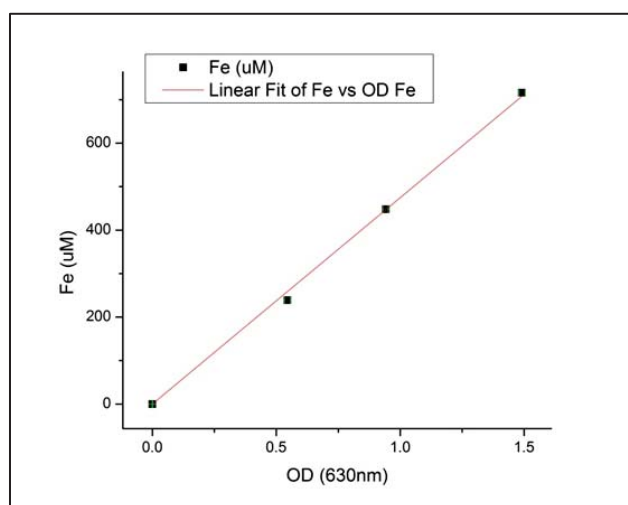
Figure 3.12. Standard curve of known concentrations of iron for the Perls Prussian Blue assay. Samples (refer to Fig. 3.11 above) were analyzed by spectrophotometry at 630 nm.

Table 5. Iron content for magnetic HASMC as measured by Perls Prussian Blue.

Sample	n	Mean	Fe (µM/ml)
Negative Control	18	0.04	---
Passive Uptake			
6 µg/ml	18	0.19	2.91×10^{-4}
8 µg/ml	18	0.08	1.49×10^{-4}
12 µg/ml	18	0.10	2.11×10^{-4}
16 µg/ml	18	0.04	1.49×10^{-4}
Electroporation			
16 µg/ml	18	0.03	7.37×10^{-5}
18 µg/ml	18	0.01	-3.41×10^{-5}
24 µg/ml	18	0.01	-2.51×10^{-5}
32 µg/ml	18	0.07	1.44×10^{-4}
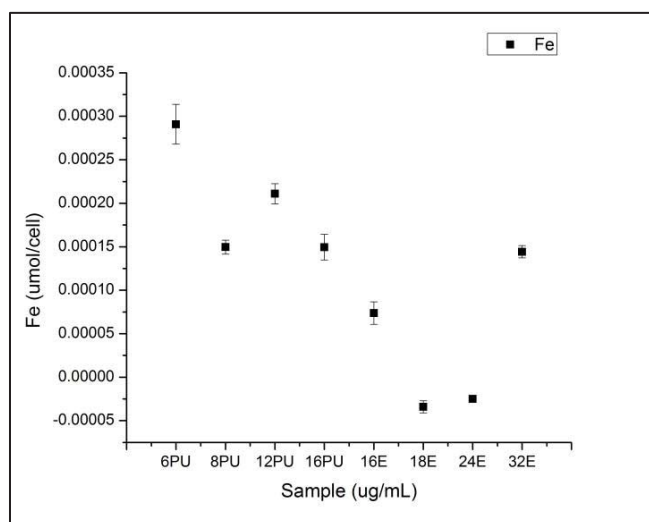
Figure 3.13. Graphical representation of values listed in Table 5 for iron detected within magnetic HASMC. "U" stands for HASMC that used PU to internalize SPION. "E" stands for electroporated HASMC.

The data in Table 5 and Figure 3.14 reflect that HASMC passive uptake is effective in

internalizing the SPION with the highest uptake at 6 µg/ml: 2.91×10^{-4} µM/ml. The EP

samples showed the best Fe content at 32 μg/ml: 1.44×10^{-4} μM/ml while the two middle

iron samples (18 and 24 μg/ml) were negligible, indicating that the EP process was not

successful. It could be that the cells actively pumped out the IONP during proliferation.

The highest concentration of electroporated iron oxide nanoparticles show very similar

results compared with the passive uptake 1.49×10^{-4} μM/ml.

3.3.1.4   Measurement of Possible DNA Damage by CometAssay®

For completeness, another set of experiments were carried out to include a positive

control (30% H_2O_2, as mentioned previously). At a density of 2 μg/ml of commercial

SPION, no statistically significant differences were found between the negative control

and the samples – compare the percentage of DNA in the comet tail and the Olive

Moment (Tables 6 and 7, respectively). Figure 3.14 shows representative results of

nucleoids of HASMC after staining with SYBR® Green I dye. Compact nucleoids are

evident for all the tested samples and no evidence of DNA fragmentation per visual

inspection (Figure 3.14, Panels B, C, D and E) when compared with the negative control

(Panel A). Only the positive control exhibits a long tail as a result of hydrogen peroxide

treatment (Panel F). In Fig. 3.14, the nucleoid diameters range between 25 and 35 μm for

all samples (Panels A, B, C, D and E), while positive control tails reached lengths of up

to 121 μm showing the genotoxic effect of the hydrogen peroxide treatment.

The results shown in Tables 6 and 7 are graphed in Figure 3.15. For percentage of DNA

in Tail (Fig. 3.15, Panel A), the data for pulsed cells with SPION reflect 0-5% DNA

damage correlating very well with the negative control (Panel B). The positive control

possesses above 10% to 25% of DNA in the tail. Taken together, the data reflect that

electroporated HASMC tolerate both the EP procedure under the different parameters, as

well as proliferating nicely with the internalized SPION out to 120 h post electroporation.

Table 6. Summary of Percentage of DNA in Comet Tail for Pulsed HASMC with SPION.

Sample	EP	% DNA in Tail			
		n	Mean	Standard Error (±)	p Value
1 - Untreated Cells	--	50	2.40	0.42	---
2	500 V/cm, 100 μs	50	1.98	0.34	$0.45^{\dagger}$
3	400 V/cm, 100 μs	50	2.36	0.45	$0.95^{\dagger}$
4	200 V/cm, 100 μs	50	2.92	0.64	$0.48^{\dagger}$
5	500 V/cm, 200 μs	50	2.19	0.36	$0.67^{\dagger}$
6 - Positive Control	--	50	17.92	1.18	3×10^{-18}

DNA percentages for HASMC electroporated with SPION. † - no statistically significant differences (p>0.05).

Table 7. Summary of Olive Moments for Pulsed HASMC with SPION.

Sample	EP	Olive Moment			
		n	Mean	Standard Error (±)	p Value
1 - Untreated Cells	--	50	1.07	0.19	---
2	500 V/cm, 100 μs	50	0.86	0.15	$0.37^{\dagger}$
3	400 V/cm, 100 μs	50	1.22	0.25	$0.68^{\dagger}$
4	200 V/cm, 100 μs	50	1.58	0.39	$0.23^{\dagger}$
5	500 V/cm, 200 μs	50	1.12	0.19	$0.86^{\dagger}$
6 - Positive Control	--	50	22.82	1.93	2.67×10^{-15}

Olive Moment values for HASMC electroporated with SPION. No statistically significant differences (†, p>0.05) between negative control and samples.

A. Negative Control

B. 500 V/cm, 100 μs

C. 400 V/cm, 100 μs

D. 200 V/cm, 100 μs

E. 200 V/cm, 200 μs

F. Positive Control: 30% H₂O₂
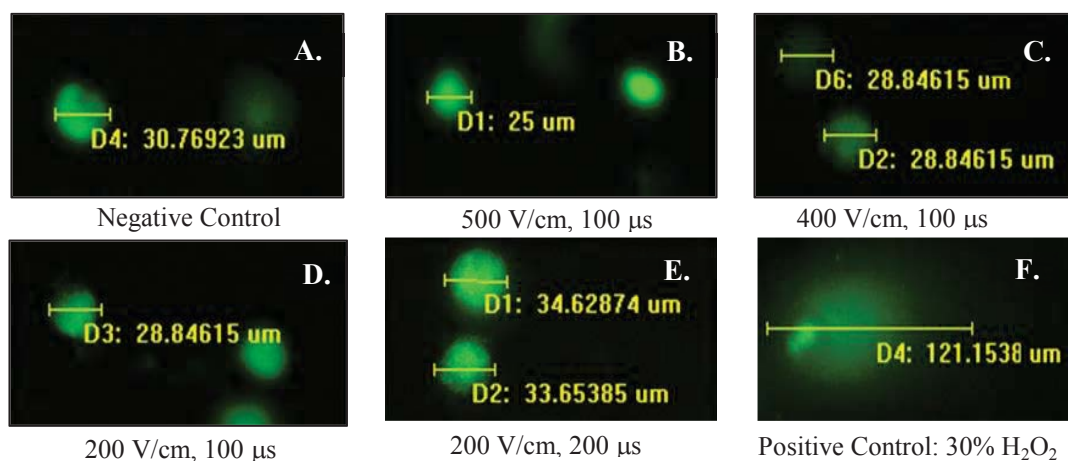
Figure 3.14. CometAssay® results for HASMC with SPION. Panel A: Negative control, Panels B, C, D, E - Pulsed HASMCs with SPIONs, Panel F: Positive control. Data reflect that HASMC tolerates EP and SPION internalization.
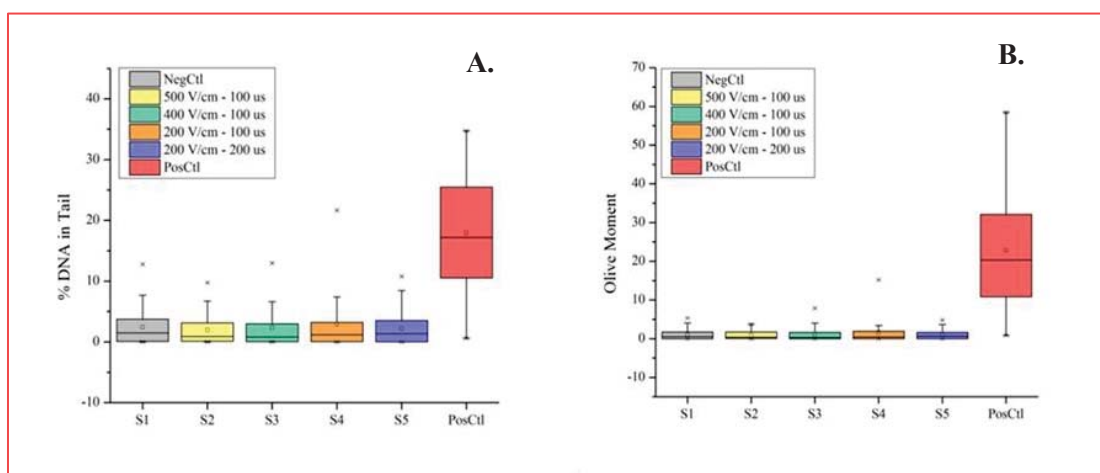
Figure 3.15. Percentage of DNA damage (Panel A) and Olive Moment (Panel B) of pulsed HASMC with SPION. CometAssay® samples are equal to negative control (S1).

3.3.2   Scheme 2: Synthesis of BNC/MBNC and Static Bioactive Stent Prototypes

3.3.2.1   Preparation of Standard BNC

BNC pellicles were easily produced after 72 h of incubation as seen in Figure 3.16 below.

As can be seen in the image, the pellicle takes the shape of the container it is growing in

and occurs at the boundary of air and liquid medium. In Fig. 3.17, the BNC scaffold is

showing pores that are large enough to allow cells to pass through (selected pores were

~3.8 μm in diameter, while other pores (red arrow) are significantly larger). These pores

are large enough to add SPION to and thus the 3-day incubation period was determined

to be the optimal growth period for the BNC samples. The next step was to render the

standard BNC magnetic. The succeeding section discusses those results.
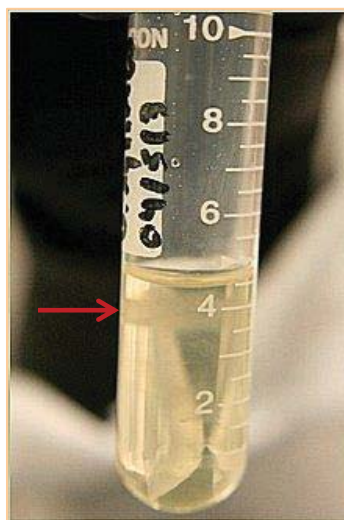
Figure 3.16. Bacterial nanocellulose obtained after 3 days of culture. Red arrow points
to the pellicle growing at the interface of the air-liquid boundary.
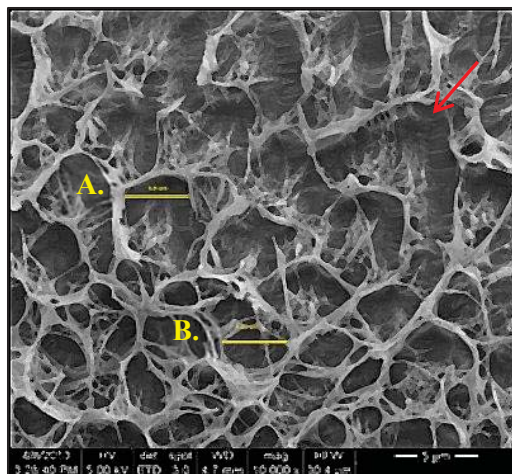
Figure 3.17. SEM of cross-section of BNC showing pores throughout the scaffold. Scale is 5 μm. Pore sizes selected: A. 3.8 μm, B. 3.85 μm. Red arrow points to pore that is ~5 μm by eye.

3.3.2.2   Preparation of MBNC

3.3.2.2.1   Magnetic Nanoparticle Synthesis Reaction

In order for the MBNC to be ferromagnetic – able to attract magnetic cells without an external magnetic force – the minimum critical size for the NP is 100 nm in diameter [111]. This parameter has been satisfied as evidenced by Figure 3.18. The mean hydrodynamic diameter of the coated MNP was found to be ~100 nm via DLS (dynamic light scatter) measurements. It is important to understand that uncoated IONP yielded by the reaction aggregate together as seen in Figure 3.19. This phenomenon is unacceptable in biological systems and describes why it is so important for the biocompatible filming of the iron oxide nanoparticles be performed even while they are embedded within the BNC mesh. The more monodispersed these NP are, even while attached to BNC fibrils, the better off for any *in vitro* or *in vivo* test system.
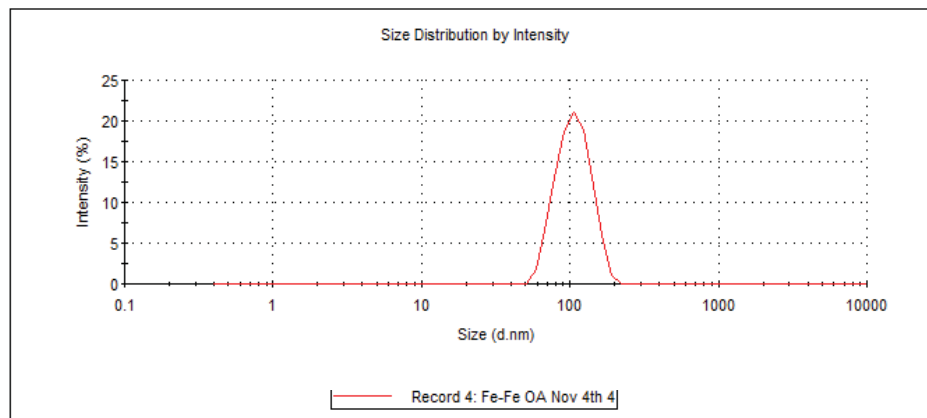
Figure 3.18. Mean DLS size measurement of coated MNP. Average hydrodynamic diameter is ~100 nm.
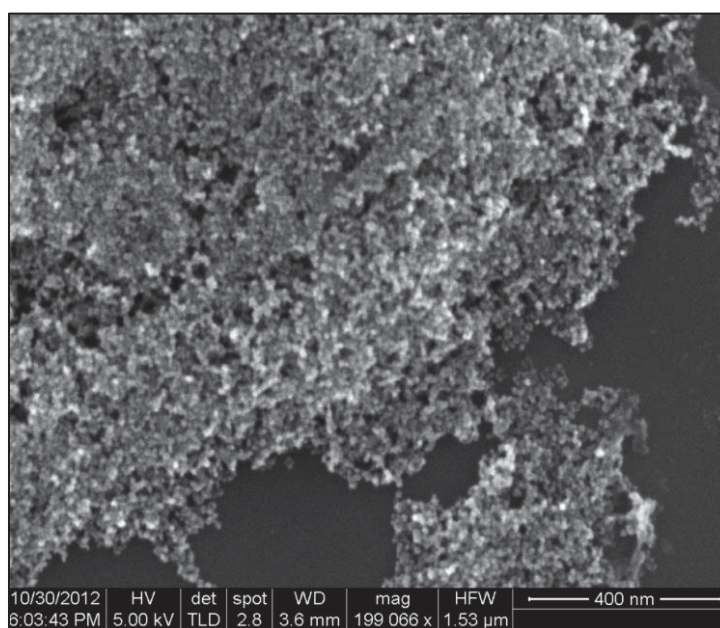
Figure 3.19. SEM of uncoated IONP in water. Without a biocompatible coating, the MNP easily agglomerate to each other.

3.3.2.2.2   Synthesis of MBNC Sample

Uniform dispersion of IONP is accomplished by the reaction given in Section 3.2222.1 of

this document. Figure 3.20 shows a magnified SEM image of the MBNC fibers. The

picture displays the individual BNC filaments incrusted with the nanoparticles.

Measurements were taken of the diverse diameters of the coated fibrils ranging from 29.3

nm to 129.6 nm. Moreover, the paramagnetism of the MBNC was proven when a sample

of it was exposed to a rare earth magnet (6 Gauss or 0.6 mT) and it immediately was

attracted to magnet.
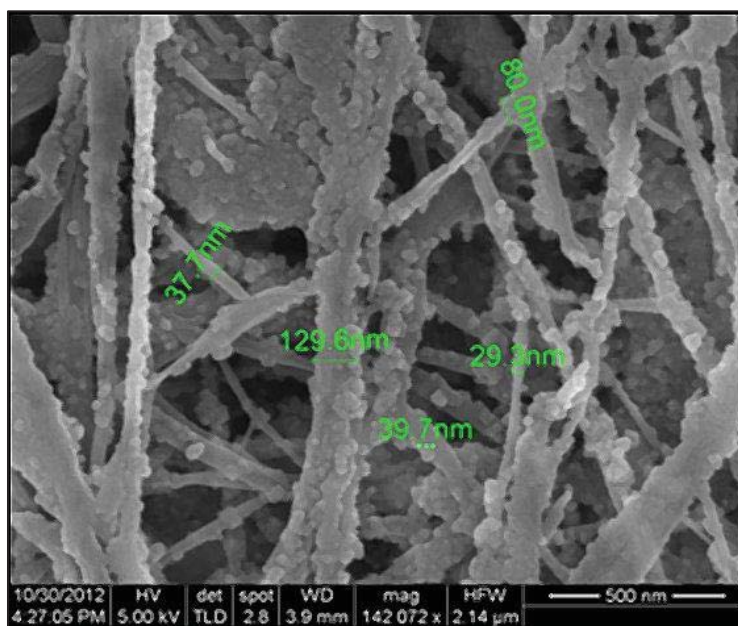
Figure 3.20. SEM image revealing the IONP coating on the BNC fibers. There are a
variety of fibril widths: 29.3 nm, 37 nm, 39.7 nm, 80 nm, and 129.6 nm.

The MBNC was also scrutinized to verify iron content within the matrix. Concurrent

SEM/EDS (energy dispersive spectroscopy) analysis showed that there was Fe and O

located within the matrix and on the fibers themselves. In Figure 3.21, there is one

embedded nanoparticle that is 8.91 μm in diameter. This NP proved to be an iron oxide

NP (see Figure 3.21) as determined by EDS. Figure 3.22 indicates the presence of

elemental iron (~6.3 keV, ~0.6 keV) comprising the IONP seen in Fig. 3.21. This proves

that the reactions rendering the BNC magnetic, was successful. The peak seen at 7 keV

is background energy that could be a contaminant as a result of sample processing.

Nevertheless, the peak at 6.3 keV positively proves that the confirmation of MNP into the

BNC framework was efficacious.
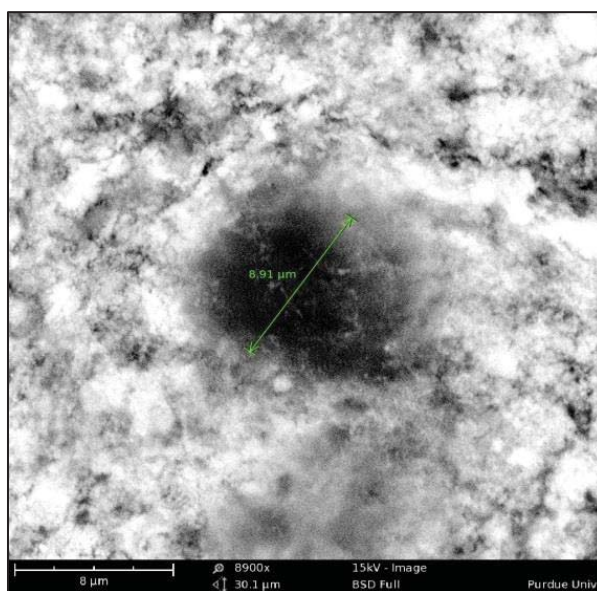
Figure 3.21. MBNC under SEM/EDS analysis. Dark spot: IONP with diam. of 8.91 μm.
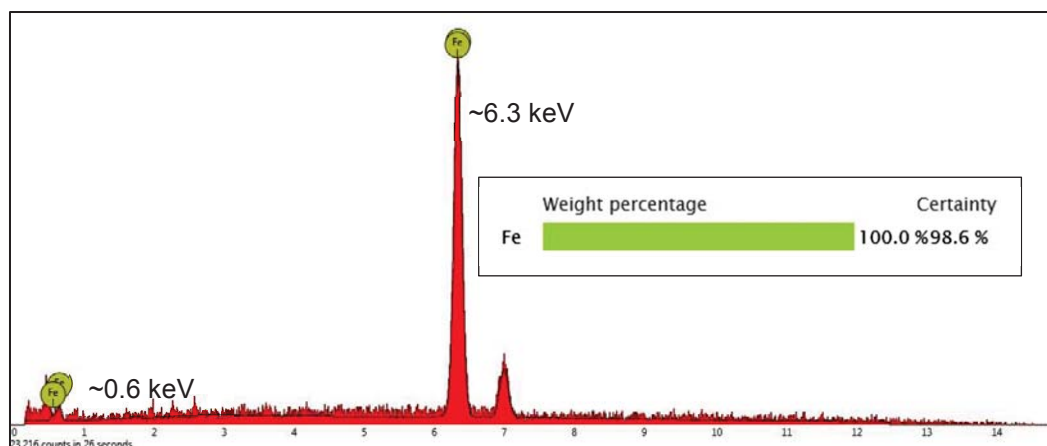
Figure 3.22. EDS analysis of IONP within MBNC (refer to Fig. 3.21). Fe peaks appear at ~0.6 keV and ~6.3 keV. (Peak at 7 keV is background energy.)

An important characteristic of the BNC is porosity. The size and density of the pores determines the ability for blood and other fluids to pass through the BNC. Attention to pore sizes after MNP impregnation is of extreme importance. Figure 3.23 is an example of a pore within a MBNC sample analyzed by SEM. The example pore size is 14.32 μm^2 and is more than enough for the standard 10 mm sized cell. With pore diameters ranging from 8.91 μm to 14.32 μm after impregnation of IONP, the MBNC should be porous enough to allow for the flow of fluids throughout its matrix.
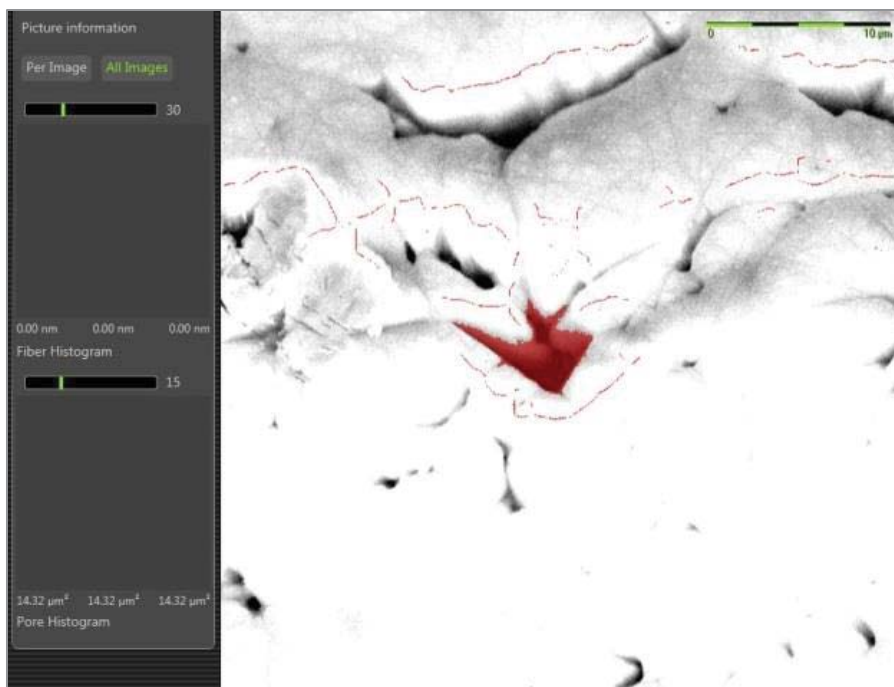
Figure 3.23. NanoScience SEM analysis of a representative pore of a 72 h MBNC sample. Pseudocolor analysis is used to highlight pore. Pore size is 14.32 μm^2.

3.3.2.3 Preparation of Static Bioactive Stents

Figure 3.24 shows the 24 h BNC pellicles grown onto the Nitinol stent scaffolds. These are the static bioactive stent devices generated after all testing was completed for the bacterial nanocellulose material. Panel A shows a vertical stent with BNC, while Panel B shows the stent oriented horizontally.
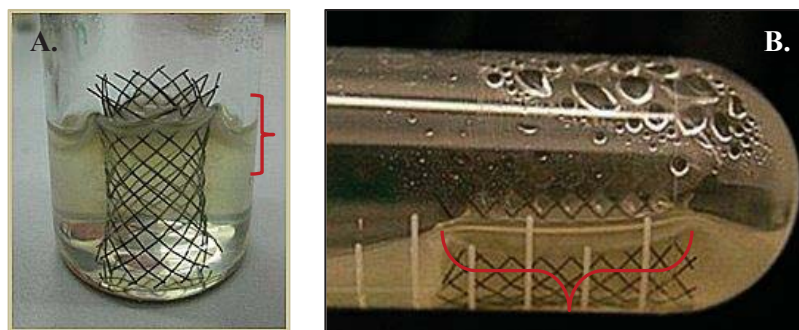
Figure 3.24. Static bioactive stents in Mannitol media. Panel A: Red bracket shows BNC growing at air/liquid boundary and through vertical stent scaffold. Panel B: Red bracket shows BNC growing at air/liquid boundary of horizontal stent scaffold.

3.3.3   Brief Summary of Results

Magnetic labeling of the HASMC with 30 nm SPION was performed by two different pathways: passive uptake and electroporation. HASMC was rendered magnetic by both methods successfully as determined by iron concentration studies, SEM and viability assays. While PU was successful at all concentration (6-16 μg/ml) out to 120 hours post uptake, a method was needed that would prove quicker and thus EP was utilized. Four pulses at 500 V/cm and 100 μs duration proved to yield ~81% viable cells after 120 hours post pulse, while 4 pulses at 200 V/cm and 100 μs duration slightly increased viability to ~88%. Perls Prussian Blue assay showed that EPed HASMC at 32 μl/ml SPION provided an internal iron concentration of 1.44×10^{-4} μM/ml (compare to PU at 1.49×10^{-4} μM/ml for 16 μl/ml SPION density). Subsequent CometAssay® results confirmed that the PU, EP, and living with the internalized SPION, were all conditions that were tolerated well by the HASMC with no DNA damage.

BNC and MBNC were synthesized to render pore sizes in the mesh of ~4-14 μm in diameter. The pore size is very important because cells need to be able to flow through the BNC/MBNC matrices to begin to close the aneurysm neck. The sizes generated are large enough to allow for cellular flow. Further, the iron oxide nanoparticle synthesis was optimized prior to rendering the BNC magnetic. The resultant hydrodynamic diameter of the MNP was 100 nm which is the critical size needed for a material to be ferromagnetic.

3.4   Discussion and Conclusions

There were some challenges to the magnetic labeling of the cells. First, the cells grew rather slowly and did not come up to confluency for 4 days after each split. This made the amount of cells needed for viability assays and for SPION density testing difficult. Furthermore, these cells are only good for 16 to 18 passages before senescence, so all assays had to be planned very carefully before the cells were no longer within their log phase of growth. This was the reason why the PU experiments were performed with lower SPION densities compared to the electroporated specimens at the higher concentrations. With the slower growth rate of these cells, it was decided to take the viability assays out to 5 days to determine if the perturbation of the uptake and internalization of the SPION on the HASMC would be detrimental. This helped to reduce the number of splits the cell populations had to endure. Secondly, it was also rather difficult to keep the CometAssay® procedures consistent each time the tests were performed in the beginning. Sometimes the agarose detached from the slides after the electrophoresis step and had to be retrieved from the Coplin jars. Sometimes the sample

slides floated off the electrophoresis chamber surface and that would cause issues with the orientation of the slides during electrophoresis. These problems were dealt with and solved over the many times the assays were run so that ultimately solid results were obtained.

The synthesis of the bacterial nanocellulose was relatively easy to perform and perfect, but to find the size of pellicle needed for the static bioactive stent had to be determined. The 12 mm x 75 mm culture tube turned out to be the best receptacle for the bacterial growth (24 h incubation). The pellicles yielded were easily transferred into the magnetic IONP synthesis reaction to obtain MBNC. The BNC reaction was also used to generate pellicles that were grown into the nitinol stents to make up the static bioactive stent prototypes. While the growth was done successfully, there was a problem with the pellicles staying on the stents themselves. The pellicles grew through the nitinol mesh, however, once the static bioactive stents were removed from the liquid medium, it was found that the pellicles were just loosely hanging onto the nitinol stents. When washes of the devices were attempted, the BNC pellicles sloughed off easily into the tubes. This version of prototype is obviously not going to work. The BNC pellicles must be "glued" in place somehow, such as by electrospinning or polymer sleeve braiding [112], so as to permanently bind the biomaterial to the nitinol mesh.

Overall, the results yielded repeatable synthesis of magnetic bacterial nanocellulose embedded with SPION that was compatible with HASMC. An interesting note is that while the BNC stent prototype does not have to necessarily be biodegradable for *in vitro*

work, it is this property that is highly desirable for any *in vivo* implantable device. It has also been shown in the literature that biodegradability is a property that shows up in cellular work as evidenced by the efforts of the Freed group (worked with synthetic biodegradable polymers) [113]. This biomaterial is magnetic in the presence of a magnetic field and can be grown to any size or shape needed. Further, the samples that were made for this project have optimal pore sizes for fluid flow and cellular migration.

CHAPTER 4. AIM 2: IMPROVE AND PROMOTE TISSUE GROWTH AND
BIOCOMPATIBILITY UTILIZING BACTERIAL NANOCELLULOSE

4.1   Introduction

Bacterial nanocellulose (BNC) and magnetic bacterial nanocellulose (MBNC) had to be

tested to ensure that the HASMC would grow on these biomaterials successfully. The

first step was to confer biocompatability on the MNP infusing the MBNC scaffold. Citric

acid, PEG, and PEI were used to coat the MBNC and apoptosis assays were performed to

determine an DNA damage to the HASMC that were growing on the biomaterial.

Proliferation was studied by looking at the presence of F-actin. F-actin staining is used to

both characterize HASMC and to measure the health of mammalian culture systems.

Fluorescent phalloidin was utilized to label F-actin found in the cytoskeleton of the cells

seeded onto the BNC and MBNC. In addition to propagation, it was important to study

how cells actually migrate from one place to another. Specifically, manufactured lesions

were used to follow the progression of cells from an area surrounding the "wound" into

that space to fill it in – i.e. healing the "injury". This is an important factor in the

function of the static bioactive stent because once the cells are attracted to the stent, it is

imperative that they begin to dam up the aneurysm neck (i.e. the wound or lesion). Once

the neck is completely closed, then the blood supply is cut off into the aneurysm sac and

the aneurysm is healed. Wound healing assays were therefor performed to visualize and

quantify the effectual HASMC migrations. In addition to these investigations, HASMC

attraction to the biomaterials was observed in an effort to establish evidence that the

BNC/MBNC were able to attract the cells ferromagnetically. Brightfield micrography

was used to observe how the cells surrounded these biocomponents *in vitro*.

4.2   Materials and Methods

4.2.1   Scheme 1: Cellular Growth and Migration Assays

4.2.1.1   HASMC Proliferation Tests

4.2.1.1.1   F-Actin Detection Studies

Before the migration assays could be performed, it was important to determine that the

HASMC would grow on the analytes, thus simple growth tests were performed for the

presence of actin. The magnetic bacterial nanocellulose (MBNC) sample was placed

onto a sterile glass coverslip and allowed to dry for 24 h at room temperature.

Afterwards, the MBNC coverslip was placed into a well of a 24-well tissue culture plate.

HASMC were seeded in a T-25 tissue culture flask at $1x10^6$ cells/ml and allowed to

proliferate until 70-80% confluence (by eye) was achieved. Cells were harvested and

seeded onto the MBNC coverslip at a seeding density of $1x10^5$ cells/ml and allowed to

incubate for 72 h. The coverslips were next transferred into sterile glass Petri dishes.

This step was necessary, because the Phalloidin dye contains methanol that could leach

out contaminants from the plastic of the tissue culture dish and interfere with the staining

process. Alexa Fluor® 532 Phalloidin is a high-affinity F-actin probe (Cat. #A22282,

Life Technologies, Inc.) that will light up with a green fluorescent color when attached

to the actin in a live, healthy, proliferating cell [114].   DAPI (4',6-Diamidino-2-

Phenylindole, Cat. #D1306, Life Technologies, Inc.) is a counterstain that binds to the

adenine-thymine (A-T) bundles of DNA and provides a deep blue fluorescence when

bound to the nucleus of a cell. Both dyes were prepared according to manufacturer's

directions. Following the PBS wash, the cells were fixed with 500 μl 7% methanol-free

formaldehyde solution (Cat. F8775-25ML, Sigma-Aldrich) for 10 minutes at room

temperature (methanol can disrupt actin during the fixation process). Samples were

washed and 500 μl of 0.1% Triton™ X-100 (Cat. T8787-50ML, Sigma-Aldrich) was

added to them for 5 minutes at room temperature to permeabilize the cells. Again, the

cells were washed and 200 μl of 1% bovine serum albumin (Cat. A3311-10G, Sigma-

Aldrich) was added to them for 30 minutes at room temperature to stop the

permeabilization reaction. A PBS wash step was performed and 200 μl of the Alexa

Fluor® 532 Phalloidin stain was added to each sample and incubation proceeded for 20

minutes at room temperature in the dark. A PBS wash was done and 300 μl of 300 nM

DAPI counterstain was added to each sample. Samples were incubated for 30 minutes in

the dark at room temperature. After staining, the samples were washed with PBS again

to reduce background and visually analyzed via fluorescent microscopy using a Nikon

Optiphot upright fluorescent microscope (Nikon Instruments, Inc.) fitted with correct

optical filters for the Phalloidin dye (532 nm excitation and 555 nm emission) and DAPI

(358 nm excitation and 461 nm emission) and a Nikon Coolpix 990 camera (see Figure

4.3).

To compare the growth of HASMC alone (no MBNC substrate), F-actin labeling was

performed again. This time 100 nm Acti-stain™ 488 Fluorescent Phalloidin (Cat.

#PHDG1, Cytoskeleton, Inc., Denver, CO) was utilized according to manufacturer's instructions. Cells were grown to 3 x 10^5 cells/ml density at 92% viability and harvested. Cells were seeded into a 35 mm FluoroDish™ (Cat. 70682, Ted Pella, Inc., Redding, CA) at a density of 10^4 cells/dish and allowed to grow to confluency over 48 hours. Next, HASMC were washed with PBS at 37°C followed by fixation using 1 ml 3.7% paraformaldehyde solution for 10 minutes at room temperature followed by a PBS wash for 30 seconds. Cells were permeabilized for 5 minutes with permeabilization buffer (0.5% Triton X-100 in PBS) at room temperature followed by a wash with PBS for 30 seconds. F-actin staining was performed last by adding 200 μl 100 nm Acti-stain™ to the fixed cells for 30 minutes at room temperature in the dark. At the end of the incubation period, cells were washed three times with PBS to wash off excess dye and reduce any background staining. Nuclei were counterstained with 200 μl 3 μM propidium iodide (PI, Cat. P3566, Life Technologies, Grand Island, NY) for 15 minutes at room temperature in the dark. Cells were washed three times with PBS and stored in 1 ml fresh PBS and used for confocal microscopy (refer to Figure 4.5 in the Results section). Confocal microscopy was performed on an Olympus FV1000 Microscope (Olympus America, Center Valley, PA) using the 488 nm argon ion laser to excite the Acti-stain™ and the 515 nm argon ion laser to excite the PI (green color is Phalloidin and orange color is the nucleus, check out Fig. 4.5), and a 40X fluorescence objective. To determine that the F-actin filaments were stained throughout the cell and not just sporadically, 3 μm image slices were taken as can be seen in Fig. 4.5.

4.2.1.1.2 HASMC Attraction Experiments

HASMC were studied to see if BNC and MBNC could naturally attract them; this is a key to attracting cells to a bioactive stent *in vivo*. HASMC were harvested at 3×10^4 live cells/ml at 83% viability from two T-25 tissue culture flasks. BNC and MBNC analytes were aseptically placed in a 24-well tissue culture plate (Cat. 08-772-1H, Fisher Scientific, Batavia, IL). It is crucial to note that to keep the BNC and MBNC pieces from floating away, they were glued in place by a 50 µl drop of CyGEL™ (Cat. #CY10500, Biostatus Limited, Leicestershire, UK). CyGEL™ is a "thermoreversible gel" that is compatible with live cells as an immobilization agent. It is solid at room temperature and above, but liquid at 4°C. The cold CyGEL™ was applied to the bottom of the wells and then the BNC and MBNC pieces were placed on top. The CyGEL™ was allowed to warm up to room temperature whereupon it solidified and held the analytes in place. HASMC were then harvested at 3x104 cells/ml with 83% viability from two T-25 tissue culture flasks (Cat. #TP90025, MidSci, Inc., St. Louis, MO). Cells were seeded into the wells at 1×10^4 cells/ml away from the BNC and MBNC samples. The sample were cultured under normal conditions for 48 h and examined daily under bright field illumination with a Nikon inverted Diaphot microscope with a 20X objective (Nikon Instruments, Inc.). *In vitro* cell images were taken on Day 2.

4.2.1.2 Wound Healing Assays with IONP Uptake

4.2.1.2.1 Scratch Assays

It was essential to determine cellular migration with magnetically labeled cells thus the Wound Healing Assays were carried out in 24-well tissue culture vessels. Before

working with the cells, a black Sharpie was used to draw a bisecting thin line for each

well on the outside bottom of the wells to act as a pattern for the creation of the "wound"

(Figure 4.1).
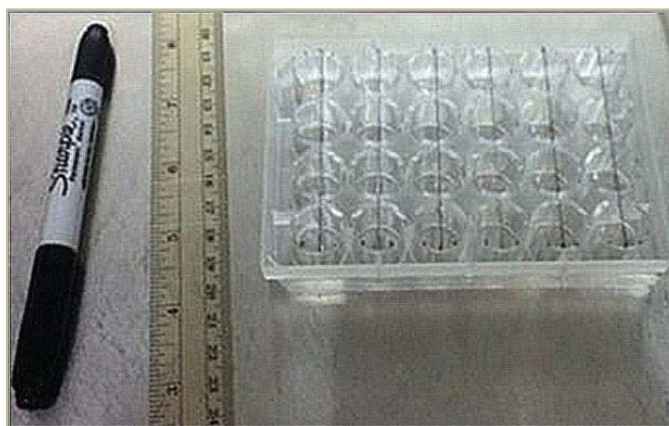
Figure 4.1. 24-well plate that has been scored (vertical black lines) in preparation of the
wound healing assay (scratch assay).

The HASMC was rendered magnetic to determine how migration would behave -

impeded or normal - with SPION present in the cells. For the SPION passive uptake,

cells were seeded in a T-25 tissue culture flask at $1x10^6$ cells/ml and allowed to

proliferate until 70-80% confluence (by eye) was achieved as stated previously. The

HASMC were incubated with 20 μl of SPION for 24 h under normal culture conditions.

The cells were harvested and seeded into wells of a 24-well tissue culture plate at a

density of $1x10^5$ cells/ml and allowed to incubate under normal conditions for 72 h to

allow a nice monolayer to form on the bottom of each well. The "wound" was made after

gently and slowly scratching through the cellular monolayer with a fresh sterile 200 μl

pipette tip vertically down the center of the well following the line drawn on the underside of the well. Wells were gently washed twice with fresh propagation media to remove any loose cells and debris. Cells were then incubated for a total of 36 h and fed during this period. To confirm that SPION were taken up into the cells, at each six hour interval, the cells were fixed *in situ* with 10% Formaldehyde Buffered Solution (Cat. #BDH0502-1LP, VWR Scientific) and stained with the Iron Stain Kit (Cat. HT20-1KT, Sigma-Aldrich) according to manufacturer's protocol. This is known as the Prussian Blue reaction where deposits of iron stain an intense blue color when treated with acid ferrocyanide. Samples were viewed under brightfield microscopy using a Nikon Diaphot microscope (Nikon, Inc., Melville, NY) and under a 10X objective.

4.2.1.2.2 CytoSelect 24-Well Wound Healing Assays

The CytoSelect™ 24-Well Wound Healing Assay kit (Cat. #CBA-120, Cell Biolabs, San Diego, CA) was additionally used to visualize the wound healing process. In a 24-well tissue culture plate (Cat. #08-772-1, Fisher Scientific), CytoSelect™ wound healing inserts were placed into the wells to form a barrier in which cells would not grow, i.e. the "wound". The inserts provide a stable consistent 0.9 mm wound gap between cells. The CytoSelect™ wound healing inserts were aseptically placed into the wells. The HASMC were added to each side of the wound in each well at a concentration of 0.5×10^6 cells/ml and allowed to grow for 48 hours under standard culture conditions until a monolayer was formed around the barriers. It is important to note that during this time, the HASMC passively took up the SPION as well (as described previously in Section 3.2.1.1 of this

text). After incubation, the inserts were aseptically removed to begin the healing process

and allow for cellular invasion into the "wound". Wells were gently washed twice with

fresh propagation medium to remove any detached cells. Fresh medium was added

during the incubation time of 36 hours. At each six hour interval, cells were fixed *in situ*

and stained with the Iron Stain Kit as explained before and visualized under brightfield

microscopy. To enumerate migrated cells within the wound area, particle analysis was

performed with Image J software (NIH, Washington, DC). Figure 4.2 shows the initial

set up in the tissue culture plate. The blue arrow points to a representative well where the

CytoSelect insert has been placed to make a vertical "wound" 9 mm in diameter.
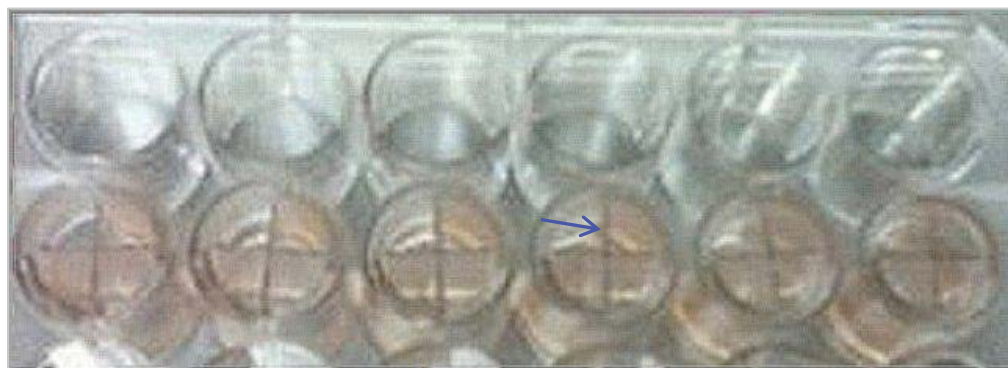
Figure 4.2. CytoSelect Kit Setup. Blue arrow points to a well containing the CytoSelect
insert responsible for making "wounds" where cells are not allowed to grow until the
insert is removed. The insert makes a very distinctive 9 mm width area of non-growth
straight down the middle of each well.

4.2.2   Apoptosis Assays

4.2.2.1 Coating MBNC for Biocompatability

Magnetic nanoparticles are not biocompatible without some type of coating to make them

so [107–111]. The solution to the problem is to overlay the entire MBNC matrix with a

biocompatible agent. After MBNC synthesis was accomplished, the pellicles were

washed and pHed to 6.7. In separate 100 ml Erlenmeyer flasks, pellicles were placed in

36 ml PBS followed by the addition of either 4 ml 1% poly(ethylene glycol) (PEG 1000,

Cat. #sc-203182, Santa Cruz Biotechnology, Inc., Dallas, TX) solution in nanograde

water, or 1% poly(ethyleneimine) (PEI, Cat. #482595-100ML, Sigma-Aldrich) solution

in nanograde water, or citric acid (CA,) . The solution was stirred at room temperature

for 2 h and found to have a pH of 6.5-7.0 after the mixing step. The coated MBNC was

washed several more times with PBS and then exposed to UV irradiation for 24 h to

sterilize the material. SEM was performed to validate the covering of the MBNC fibers

as can be seen in Figure 3.20 in the Section 3.3.2.2.2 of this report. CometAssay®

studies were carried out to determine which biochemical would be the most suitable to be

used for the biocompatability of the MBNC throughout the rest of the research project.

For the CometAssay®, HASMC were grown as described earlier and harvested at

8.2×10^5 cells/ml at a viability of 85%. Visual inspection of the HASMC was conducted

during the 5 day incubation period under bright field illumination utilizing a Nikon

inverted Diaphot fluorescent microscope with 10X and 20X objectives (Nikon

Instruments, Inc.) and fitted with a Nikon Coolpix 990 digital camera. At 48 hours, the

CometAssay® was performed according to manufacturer's recommendations and the results were compared to the nontoxic effects of HASMC growing alone under normal culturing conditions. Positive controls were cells induced into apoptosis by treatment with Etoposide (CometAssay® Control Cells for Alkaline Comet Assay, cat. # 4256-010-CC, Trevigen, Inc., Gaithersburg, MD) and hydrogen peroxide (10 µl of 30% hydrogen peroxide solution in water added to 100 µl of cell suspension and incubated for 30 min). These Etoposide Control Cells have different levels of DNA damage produced by exposure to different concentrations of Etoposide, which induces double stranded and single stranded DNA breaks. Control Cells show incremental increases in percent DNA in the tail when the alkaline Comet assay is performed. CC0 Cells correspond to healthy cells, followed by increases in single-strand damage in populations CC1, CC2, and CC3 Cells [115]. Cells treated with hydrogen peroxide exhibit a similar effect to the ones treated with Etoposide. After electrophoresis, Comet slides were stained with SYBR® Green I Nucleic Acid Gel Stain (Cat. #S-7585, Life Technologies, Inc.) then visualized using an epifluorescent microscope (Nikon Eclipse 80i, Nikon Instruments, Inc.) at 10X and 20X power with optical filters selected for 488 nm excitation and 520 nm emission. Fluorescent imagines were captured using a Micropublisher 5.0 RTV digital camera (QImaging, Surrey, British Columbia, Canada) mounted onto the microscope. The DNA damage was quantified using CometScore™ software (Tri Tek Corp.) followed by subsequent paired T-tests (Origin Pro™ 8.6 software) to ascertain differences between the negative control (CC0), and treated control cells, and CC0 samples and HASMC samples for each BNC coating type – PEI, PEG, and CA.

4.3   Results

4.3.1   Scheme 1: Cellular Growth and Migration Assays

4.3.1.1   HASMC Proliferation Tests

4.3.1.1.1   F-Actin Detection Studies

As can be seen in Figure 4.3, F-actin fibers are visible in the control and MBNC samples (green, Panels A-D) while the nuclei are labeled with the blue DAPI dye. The cells look healthy and have attached to the BNC fibers. The Phalloidin dye stains the BNC a bit, providing background staining (compare Figure 4.3 to Figure 4.4) seen in the images. Regardless of the background staining of the F-actin, the presence of this protein proves the HASMC were actively growing and successfully synthesized a monolayer on top of the MBNC surface, helping to confirm the biocompatability of this biomaterial.

Confocal images were taken of HASMC cells (see Fig. 4.4) where the F-actin was successfully stained with the Acti-stain™ 488 Fluorescent Phalloidin and counterstained with PI for the nuclei. The presence of the F-actin, again confirms that the HASMC are healthy and actively proliferating. Filopodia can be seen (yellow arrows) in Fig. 4.4 indicating that the cells were actively migrating.
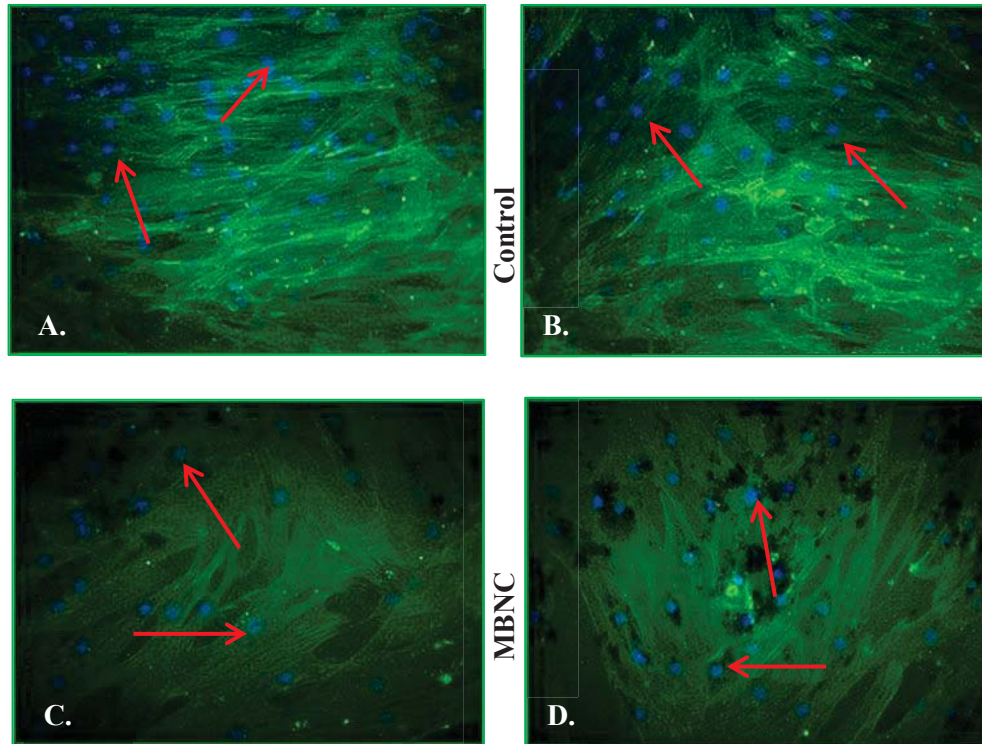
Figure 4.3. HASMC growing on MBNC. Panels A, B are HASMC on glass coverslip as negative control. Panels C, D are cells growing on MBNC. Alexa Fluor® 532 Phalloidin (green) shows F-actin fibers of healthy cells. Blue color (DAPI) corresponds to nuclei (red arrows).
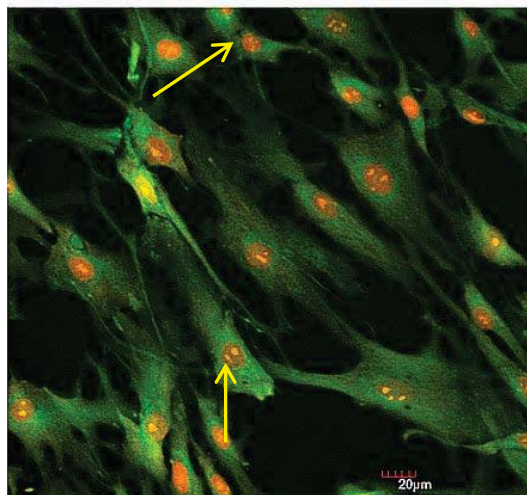
Figure 4.4. HASMC stained with Acti-stain™ 488 Fluorescent Phalloidin for cytoskeleton labeling (green), and counterstained with PI for nuclei detection (orange, yellow arrows).

From the staining results, it is apparent that the HASMC are propagating nicely and these results compare very well to HASMC that are growing in the presence of MBNC as seen in Fig. 4.3. It is important to note that the HASMC shown in both Figs. 4.3 and 4.4 reflect the smooth cellular membrane and round nuclei – both properties indicative of proper cellular development and good condition. To confirm that the HASMC contained healthy morphology throughout the cytoskeleton and not just on the surface, confocal microscopy was performed as seen in Figure 4.5. From 22.5 μm up to 45 μm in thickness, the F-actin stained successfully to show that the phalloidin was not just staining on the surfaces of the cells, but through the entire intracellular matrix.
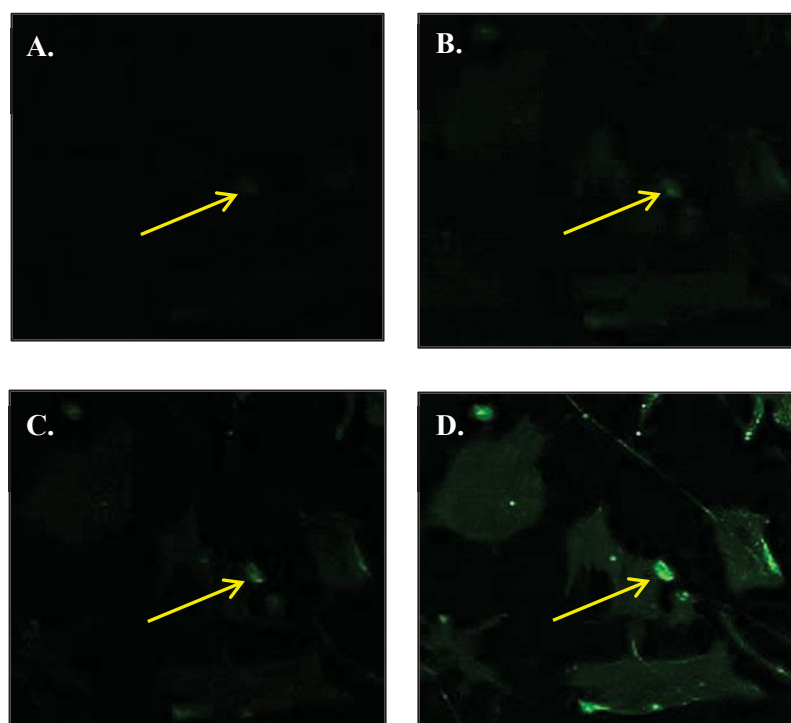
Figure 4.5. HASMC confocal images showing depth of F-actin staining (yellow arrows).
Panel A: Lowest Z-slice at 22.5 μm depth, followed by progressive slices in Panels B
and C, topping off at 45 μm slide in Panel D.

4.3.1.1.2   HASMC Attraction Experiments

HASMC were seeded in tissue culture wells away from the BNC and MBNC samples, as

described beforehand, to see if these analytes would be biocompatible enough to attract

these cells to them. Figure 4.6 shows the HASMC morphology after two days in contact

with the test specimens. The negative control, Panel A, features HASMC growing in the

absence of test material under normal culture conditions, while Panel B shows cells

growing in close proximity to the unmodified BNC sample. As can be seen in Fig. 4.6,

Panels B and D, the cells migrate towards both types of biomaterials (red arrows) and

they begin to proliferate along the edges of the analytes. Magnetic HASMC look stressed

(Panel C) compared to the negative control cells (Panel A). This may be due to the

passive uptake of SPION. Nevertheless, the cells were growing and migrating toward the

MBNC. It is also interesting to note that the magnetic HASMC follow the edge of the

MBNC perfectly (purple line, Panel D) – this could be due to a slight magnetic attraction

(i.e. ferromagnetism) given off by the MBNC that attracts the magnetic HASMC towards

itself.
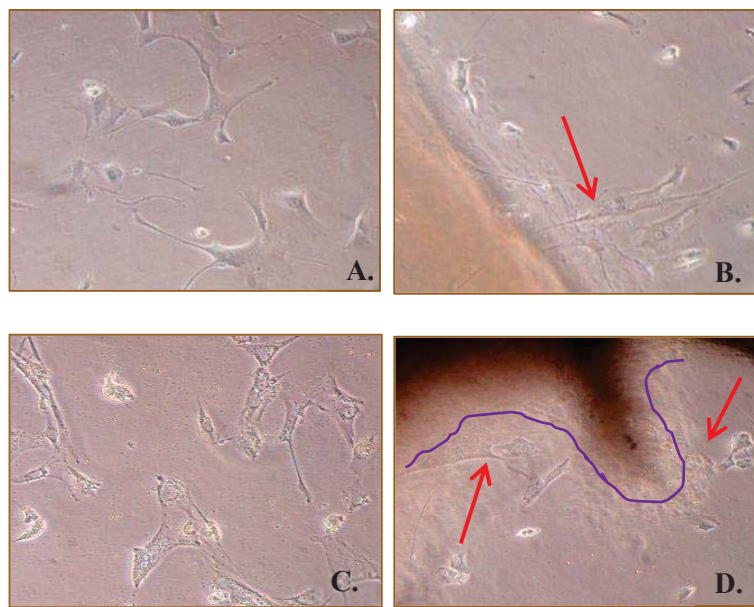
Figure 4.6. *In vitro* Wound Healing Assays. Cell migration progression clearly is seen through time course (Panels A-D), beginning at the 12 h time point and ending at 48 hour time point. Red arrows show cell attraction. Purple line shows possible ferromagnetic attraction.

4.3.1.2   Wound Healing Assays with IONP Uptake

4.3.1.2.1   Scratch Assays

In Figure 4.7, Panel A, we see the initial wound. The scratch is the open area between the sides of the cellular monolayer. As we progress through the time points (Panel B, 6 h time point, shows no cells migrating into the "wound"), we see that the cells begin to actively migrate towards the center of the "wound". Panel C (12 h time point) has 10 infiltrating cells, and Panel D increases slightly to 16 cells at 18 h. At 24 h of incubation, Panel E indicates that 35 cells moved into the "wound" area while the 30 hour time point in Panel F shows 57 cells were counted within the same area. In all panels, we see a dark pinkish stain on all cells indicating that the iron staining is positive for the presence of internalized iron oxide NP.

A.   0 h

B.   6 h: 0 infiltrating cells

C.   12 h: 10 infiltrating cells

D.   18 h: 16 infiltrating cells

E.   24 h: 35 infiltrating cells

F.   30 h: 57 infiltrating cells
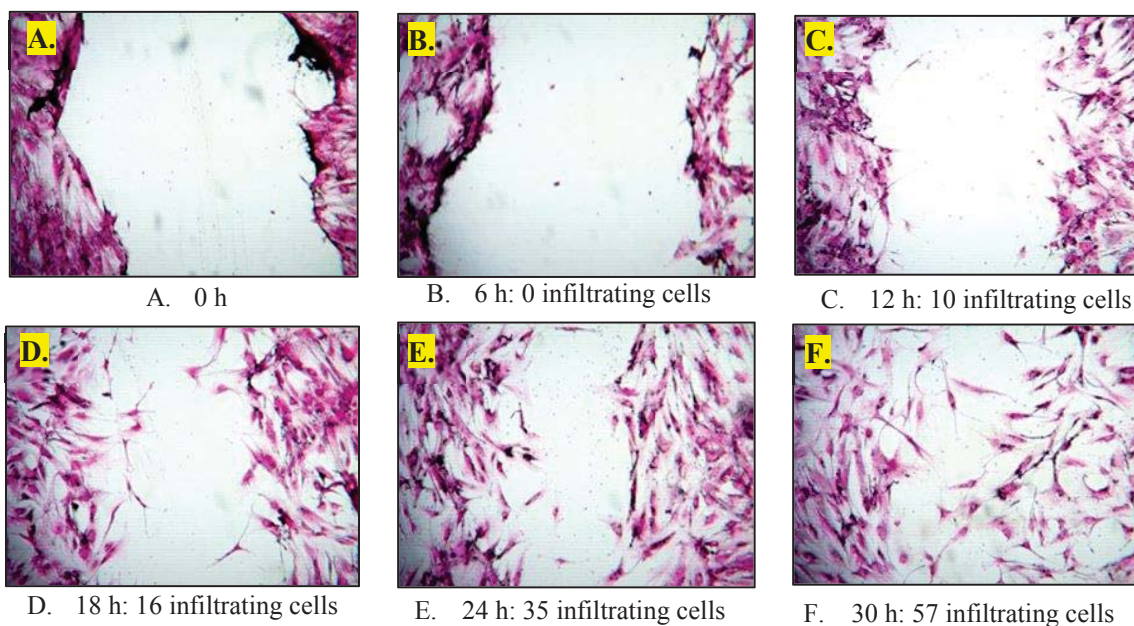
Figure 4.7. HASMC Scratch Assay Results. Panel A shows the initial "wound". The progression of infiltration of cells into the wound is visualized in Panels B – F. The wound is "healed" at 30 h (Panel F).

4.3.1.2.2   CytoSelect™ 24-Well Wound Healing Assays

The CytoSelect™ 24-Well Wound Healing Assay kit (Cell Biolabs) was additionally used to visualize the wound healing process, since the "wound" generated in this type of assay was made by a standard sized insert. Figure 4.8 Panel A shows cells in a well before the insert is placed – i.e. before the "wound" was created. Panels B through F show infiltration of healthy cells into the wound area. Further, in Panels C and D, the blue arrows point to examples of HASMC that have taken up the SPION. We see that the magnetic HASMC were successful in closing the wound at the 30 hour time point. This demonstrates that not only do the cells journey to fill in the gap, but they do so effectively with the internalized IONP.

Panel A: 6 h-68 infiltrating cells
Panel B: 12 h-149 infiltrating cells
Panel C: 18 h-122 infiltrating cells
Panel D: 24 h-100 infiltrating cells
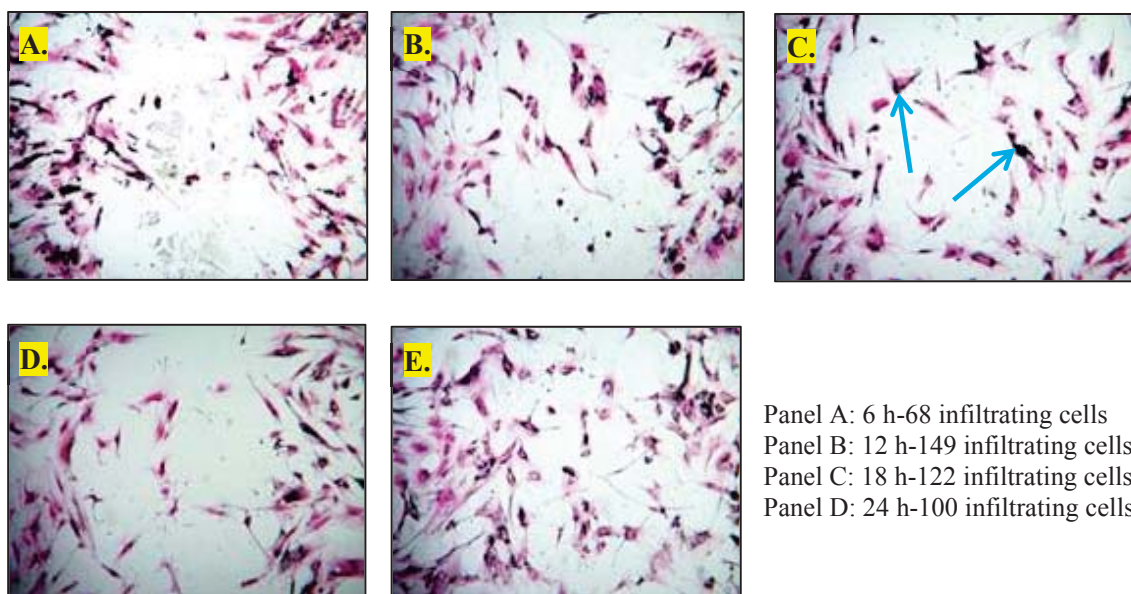
Figure 4.8. CytoSelect Wound Healing Assay. Panel A: HASMC at 6 h showing 68 cells coming into wound. Panels B through F show how cells successfully migrate to close "wound". Blue arrows in Panels C point to examples of cells stained with Prussian Blue indicating IONP internalization.

4.3.2   Scheme 2: Apoptosis Assays

4.3.2.1 Coating MBNC for Biocompatability

With the IONP synthesis reaction optimized, biocompatability had to be addressed.

Since MNP are not biocompatible, it was important to render these NP as such by coating

them with CA, PEG, and PEI. While all three coatings were successful in conferring

biocompatibility to the MBNC, the data relate that PEI is actually the best reagent to use

with the lowest DNA damage. MBNC was successfully generated and coated for

biocompatability as evidenced by SEM imaging and EDS. Once the synthesis reactions

were perfected, the preparation of bioactive stent devices was attempted. BNC was

grown into the scaffolds of sterile nitinol stents after 24 hours of incubation. Table 8

shows the results of these assays by including comet images of duplicate samples. The

exposure of HASMC to coated MBNC resulted in little DNA migration (Table 8, Panels

E, F, and G) when compared to the positive controls (Panels B, C, and D), and more

resembled the CC0 negative control results (refer to Panel A). Nonetheless, it can be

surmised that all three types of biocompatible reagents matched more closely to the

nucleoids of the negative control than to those of the positive controls. Out of the three

tested samples (Panels E, F, and G), it would seem that the pegylation of the MBNC

showed to be more toxic to the HASMC than either PEI or CA. Table 9 summarizes the

statistical results of the CometAssay® for the DNA percentage found in the comet tails.

The data clearly suggests that PEI is the gentlest coating to use on the MBNC with 2.43%

of tail DNA compared to the negative control of 1.64%. It is interesting to note that all

three coatings, were well below the positive controls of 13.2%, 12.2%, and 22% for CC1,

CC2, and CC3, respectively. Table 10 summarizes the Olive Moment results for the

samples. As discussed previously, the Olive Moment parameter is a measurement of

fluorescence intensity corresponding to the amount of genetic material present in the tail

in relation to that found in the comet head. Again, the Olive Moments corroborate the

results seen in the % DNA in the tails. Figure 4.9 shows the data in graph form.

Table 8. CometAssay® Results for Biocompatible Coatings on MBNC
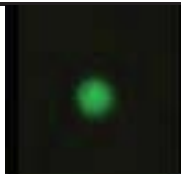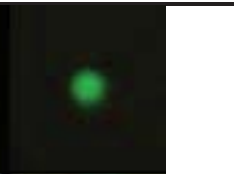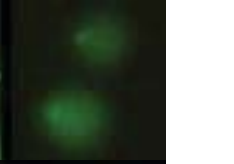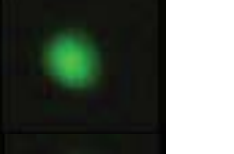
Sample	Comet Results (duplicate samples)
Panel A: Negative Control CC0 Cells	
Panel B: Positive Control CC1 Cells	
Panel C: Positive Control CC2 Cells	
Panel D: Positive Control CC3 Cells	
Panel E: Citric Acid-Coated MBNC	
Panel F: PEG-Coated MBNC	
Panel G: PEI-Coated MBNC	

Table 9. Summary of Percentage of DNA in Comet Tail From HASMC Growing with MBNC with Various Biocompatible Coatings

Sample	% DNA in Tail			
	n	Mean	Standard Error (±)	p Value
CC0 (*Negative Control*)	35	1.64	0.40	---
Citric Acid-Coated	35	3.15	0.55	0.05†
PEG-Coated	35	3.02	0.72	0.13†
PEI-Coated	35	2.43	0.54	0.30†
Positive Controls				
CC1	35	13.19	1.17	7.04×10^{-10}
CC2	35	12.24	0.57	4.43×10^{-16}
CC3	35	21.95	1.22	7.12×10^{-17}

†No statistical significance to the negative control – indicates no toxic effects (T-test, $p<0.05$).

Table 10. Summary of Percentage of DNA in Comet Tail from HASMC Growing with MBNC with Various Biocompatible Coatings

Sample	Olive Moment			
	n	Mean	Standard Error (±)	p value
CC0 (*Negative Control*)	35	0.46	0.12	---
Citric Acid-Coated	35	0.99	0.17	0.02
PEG-Coated	35	1.11	0.25	0.04
PEI-Coated	35	0.82	0.17	0.12†
Positive Controls				
CC1	35	6.04	0.61	6.17×10^{-10}
CC2	35	5.72	0.28	3.28×10^{-18}
CC3	35	14.16	1.24	1.31×10^{-12}

†No statistical significance to the negative control – indicates no toxic effects (T-test, $p<0.05$).
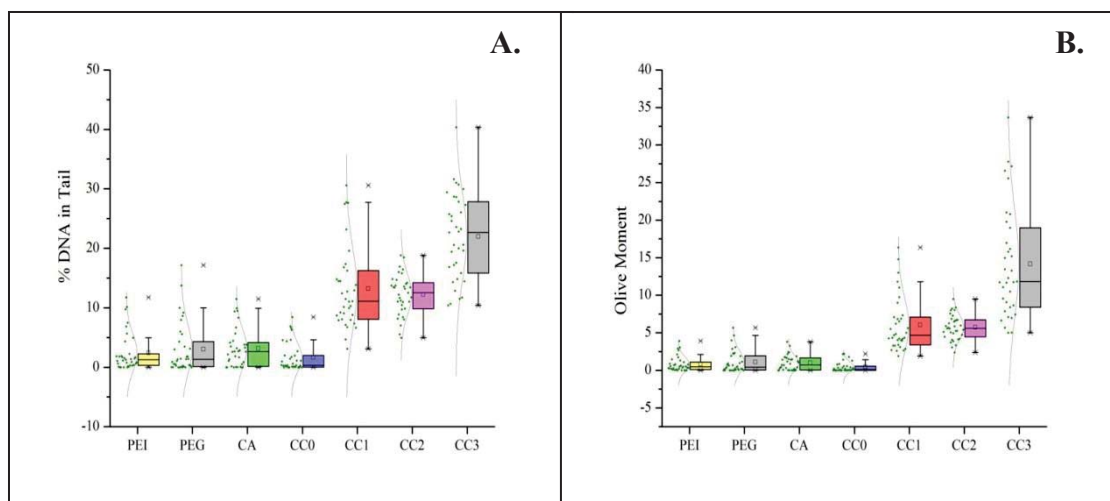
Figure 4.9. Graphical CometAssay® results for Tables 9 and 10. Panel A shows the DNA percentages and Panel B represents the Olive Moments. PEI is the best choice for biocompatible coating of MBNC.

4.3.3   Brief Summary of Results

The seeding and healthy proliferation of HASMC on MBNC has been successful according to apoptosis assays as well as visual examination. Fluorescently-labeled F-actin (by Phalloidin 488) was shown by confocal microscopy to be found throughout the intracellular matrix of the cells which proves that these cells are fit and exist fruitfully on these biomaterials. Moreover, citric acid, PEG, and PEI were tested for biocompatibility against the HASMC. These reagents were needed to confer harmonious conditions upon the embedded MNP residing in the MBNC. Without these coatings, the iron oxide nanoparticles would be toxic to any cell type. It was proven that while all three reagents were considered biocompatible, PEI was shown to be the best (compare PEI at 2.43% comet tail DNA to ~13.2% for CC1 positive control) thus this biochemical was used throughout the rest of the project. HASMC were also shown to migrate very well toward

BNC and MBNC and control studies of these cells using wound healing assays provided data exhibiting how well vigorous HASMC move upon a growth surface. A representative scratch assay showed the number of 57 infiltrating cells at the 30 h time point. In a representative standardized CytoSelect analysis, 100 cells moved to fill in the "wound" area at 24 hours.

4.4   Discussions and Conclusions

The human aortic smooth muscle cells (HASMC) had to be propagated on the new biomaterials generated and they had to be characterized before and afterwards to show that they remained unchanged. F-actin is present in healthy HASMC and is used as a marker for HASMC characterization [116]. In the cellular experiments, it was shown that F-actin is present throughout the entire cytoskeleton of the cells when they are healthy and continually proliferating. Fluorescent confocal results were equally vibrant for cells grown on the typical tissue culture flask surface compared to both BNC and MBNC. These data, together with the previous CometAssay® outcomes, show that BNC and MBNC are very biocompatible with the HASMC. Magnetically labeled HASMC exhibited slight attraction to what appeared to be ferromagnetic MBNC (no external magnetic field present). This characteristic is needed *in vivo* to attract magnetic cells to the aneurysm neck nidus to close the neck off from the aneurysmal sac. It was difficult to measure the ferromagnetic activity with the lack of instrumentation. The magnetometers used yielded sporadic results that were very inconclusive. The *in vitro* evidence was the only data that could show the ferromagnetism of the MBNC.

Iron oxide nanoparticles (IONP) are not biocompatible without special types of coatings. Therefore, citric acid, PEG, and PEI were tested to coat the MBNC after synthesis. According to the apoptosis assays, all three biochemical were successful in conferring biocompatibility, however, PEI was the one with the least amount of toxicity and was thus used throughout the rest of the project to overlay the MBNC. The coating step for the MBNC was relatively easy to accomplish, requiring no high temperature or harsh chemical reactions. With the successful apoptosis studies, the intriguing evidence that ferromagnetism existed, and the successful repeatability of the MBNC synthesis, it was concluded that the MBNC was ready for the integration into the static bioactive stent and the Aneurysm-on-a-Chip® device. Unfortunately, since standard BNC could not be successfully integrated into the nitinol stents, this next logical step in the project, was not attempted.

CHAPTER 5. AIM 3: DESIGN AND TESTING OF A DYNAMIC 2D ANEURYSM-
ON-A-CHIP™ MODEL

5.1   Introduction

This portion of the research centers on the generation of a bioMEMS prototype that could

be a potentially powerful tool in aneurysm treatment – the Aneurysm-on-a-Chip™

(AOC). The two dimensional (2D) bioMEMS (biological micro-electrical mechanical

system) mechanism is considered a dynamic bioactive stent. It is comprised of

polydimethylsiloxane (PDMS) - a polymer used to generate the microfluidics channels to

mimic the blood vessel and the aneurysm sac. A pathology-on-a-chip device such as the

AOC, must help to bridge the gap between the microfluidic world and the macro-world.

Hence, the PDMS chip is coupled to a set of pumps controlled by software for the

pumping action of the fluid through the device. There is a simple single inlet (i.e. inlet

port) used with a single outlet port combined with an "aneurysmal sac" between the two

ports. Sample particles/cells suspended in a liquid are injected into the chip and fluid

flow is measured offline using computational algorithms designed to analyze the

movement of sample entering the sac, contained in the sac, and exiting the sac. Particle

Image Velocimetry (PIV) and wall shear stress (WSS) was evaluated using a third party

software program. The 2D AOC trial product was synthesized to be redesignable and

modular to provide different configurations for simulating various aneurysm types and

fluid designs. Scheme 1 describes the AOC design and the generation of the PDMS chip,

itself. Scheme 2 provides the computational algorithmic analyses of particles and cells flowed through the device.

5.2 Materials and Methods

5.2.1 Scheme 1: Aneurysm-on-a-Chip™ Design and Synthesis

5.2.1.1 Mask Design of AOC Chip Device

A tri-layered chip design was proposed by Microfluidics Innovations, Inc. (Ravi Thakur, MI Intern, Microfluidics Innovations, West Lafayette, IN). The idea is to have one chip with three tiers that have separate functions. Working together, the three layers allow for sample flow through the device. Figure 5.1 is the diagram of the AOC model.
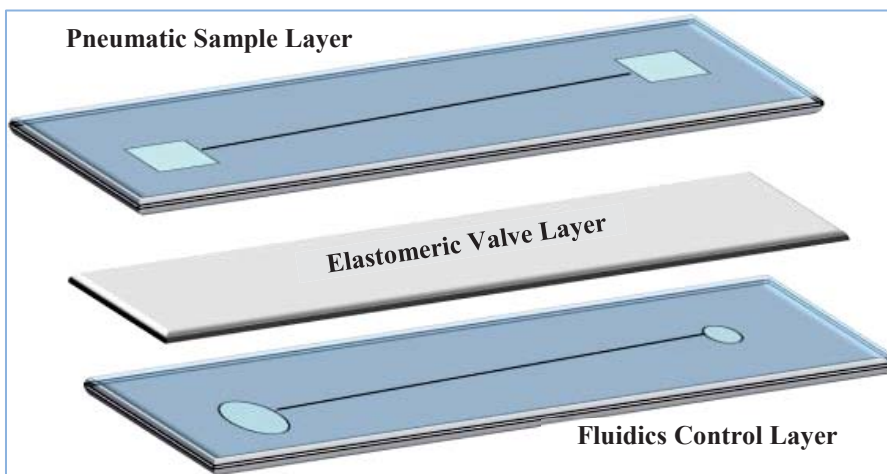
Figure 5.1. The three layers comprising the AOC device: top layer – pneumatic sample, middle layer – elastomeric valves, bottom layer – fluid control.

The Control Layer (bottom layer) is for valves operated by software for fluid flow. The elastomeric valve layer is a thin membrane providing actual valve action. The top

pneumatic layer is where the sample is flowed through the device. The mask design was based on a 5"x5" square mask that was contrived for a 4" diameter wafer, using AutoCAD software (Autodesk, Inc., Farnborough, Hampshire, England). The tri-layer design is represented functionally in this diagram (see Figure 5.7 in the Results section). Once the design was finalized, the .cad file was submitted electronically to Michael Courtney, Process and Equipment Owner for Photolithography (Birck Nanotechnology Center, Purdue University, West Lafayette, IN) for generation of the glass photomask – a special glass plate with a patterned emulsion of a metal thin film on one side that was also provided by Mr. Courtney).

5.2.1.2 Preparation of Silicon Wafers

A box of 4 in. diameter silicon wafers was purchased (100 mm thick, single polished side, Cat. #2887, Wafer World, Inc., West Palm Beach, FL) for the project. A clear plastic wafer box for washing and storage was also purchased (Cat. #2940, Wafer World). For the ultra-cleaning step, the wafers were boxed up and transported into the Scifres Nanofabrication Laboratory (25,000 sq. ft. Class 1, 10, and 100 bay-chase cleanroom, Birck Nanotechnology Center, Purdue University). Once inside the cleanroom, the wafer box was placed inside an acid fume hood with the wafers facing polished side up. The wafers were rinsed with nanograde water 3 times by allowing the water level to gently submerge the wafers. It is important to not allow the wafers to come into direct contact with the water stream, and the wafers themselves or the inside of the wafer box cannot be touched with gloved fingers. This precise handling is to ensure there are no foreign

contaminants introduced to the polished side of the wafers. The water is gently poured out of the wafer box and the Piranha solution is added at a 1:1 ratio of 400 ml 30% H_2O_2 (hydrogen peroxide, Cat. #H1009-500ML, Sigma-Aldrich) to 400 ml H_2SO_4 (sulfuric acid, Cat. #320501-205L, Sigma-Aldrich). In order to avoid a violent thermal reaction, the hydrogen peroxide was added first followed by the sulfuric acid. The wafer box was gently swirled to mix the components and the wafers were exposed to the Piranha solution for 10-15 min. at room temperature. After the Piranha step, the wafers were drained of the cleaning cocktail and rinsed with 6 changes of nanograde water for 20 min. as described before. The wafers were pulled out one by one with wafer tweezers (Cat. #TDI 6WF-SA, TDI International, Inc., Tucson, AZ) and blow dried with a nitrogen gun. The ultra-cleaned wafers were laid out onto a metal tray covered with aluminum foil and hard baked at 120°C for 15 min. in a lab oven (Isotemp Forced Air Lab Oven, Cat. #13-247-737, Thermo Fisher). The wafers were removed from the oven and allowed to cool prior to the next phase of processing.

The wafer to be used for the mask, was centered (placed polished side up) onto a 4 in. chuck fitted onto a spin coater system (Cat. #SCS 6800, Specialty Coating Systems, Indianapolis, IN) housed inside of a solvent fume hood. A quarter-sized dollop of SU-8 2000 epoxy negative photoresist emulsion (Cat. #2050, Microchem Corp., Newton, MA) was placed onto the center of the wafer. The wafer was first spun at 500 rpm for 10 s at an acceleration speed of 100 rpm/s, followed by a secondary spin at 3,000 rpm for 30 s at an acceleration speed of 300 rpm/s. This yields a 50 μm thin film of SU-8. The coated wafer was placed onto a hot plate and soft baked for 65°C for 3 min. followed by a

second bake at 95°C for 8 min. The wafer was allowed to cool prior to its exposure to

the photo mask.

5.2.1.3   <u>Synthesis of PDMS Chip</u>

5.2.1.3.1   Pattern Development on Wafer

This part of the project was actually performed by Microfluidics Innovations, Inc. which

is part of the total microfluidics system package, though this was also done by the

investigator herself. The next protocol was done in duplicate and the first step was to

perform the alignment of the mask to the silicon wafer. The alignment of the mask to the

wafer is similar to photo processing. The mask aligner positions the photo mask over the

SU-8 coated wafer. The SU-8 is very UV sensitive and is thus it becomes illuminated

("exposed") by the high-intensity UV lamp (350-400 nm) through the mask whereby the

microchannel pattern is transferred to the light-sensitive SU-8 thin film ("printing")

through the transparent areas ("pattern") of the mask. To do the alignment, the square

glass photo mask was placed into an automatic Suss MA 24 mask aligner system (SUSS

MicroTec, Inc., Sunnyvale, CA). The SU-8 was exposed to UV at 23 mJ/cm^2 for 15 s.

After alignment, the post exposure bake was done at 65°C for 10 min. on a hot plate. A

second bake was implemented at 95°C for 15 min. At this point, the pattern was visible

on the wafer.

To further develop the photoresist, the exposed wafer was submerged in a large 190 mm

x 100 mm glass crystallizing dish (Cat. #23000-19100, Kimble/Kontes, Vineland, NJ)

containing 200 ml SU-8 3050 Developer solution (Microchem Corp.) for about 3 min.

The wafer was removed from the developer and rinsed with 70% isopropyl alcohol (Cat. #A459-4, Thermo Fisher). The wafer was re-dipped in developer for another 3 min. followed by the alcohol rinse. This was repeated over and over until any white film on the wafer was completely removed. The processed wafer was dried with a nitrogen gun. The wafer was inspected with the Alpha-Step profilometer (KLA Tencor, Milpitas, CA) to check for proper channel dimensions and to make sure that there were no obvious surface defects. The wafer was then hard baked at 120°C for 5 min. on a hot plate and cooled before placing into a clean wafer holder for transport out of the cleanroom.

5.2.1.3.2　PDMS Chip Fabrication

To prepare the surface of the patterned wafer for the PDMS fabrication, the processed wafer was placed inside a solvent fume hood. The wafer was stood at about a 45° angle on the inside of a desiccator. A solution of trichlorosilane was prepared by adding 500 μl of 97% trichloro(3,3,3-trifluoropropyl)silane solution (Cat. #452807-5ML, Sigma-Aldrich) into a clean 4 ml glass vial (Cat. #60941A-4, Kimble/Kontes). The vial of trichlorosilane was placed beside the wafer in the desiccator and the lid was placed on top of the desiccator. House vacuum was applied slowly and the desiccator was sealed off. The wafer was allowed to stand under vacuum for 30 min. at room temperature to allow the trichlorosilane vapors to coat the wafer making for a cleaner surface. The wafer was removed from the desiccator, and using double-sided sticky tape, the wafer was taped with the coated side up, onto the bottom of a 6 in. clean glass Petri dish bottom (Cat. #07-250-076, Thermo Fisher). The Petr dish top was added to the bottom to keep the wafer

clean until ready for the PDMS pouring step. The finished wafer is depicted in Figure 5.3. The blue box shows the controller layer of the PDMS chip design. It is important to understand that the other patterns on the wafer were for another project, but placing different patterns on one wafer for different tasks is a common practice because individual PDMS chips can be cut out and applied to various apparatuses.

In a 5 1/4 in. plastic weighing boat (Cat. #08-732-117, Thermo Fisher), a 10:1 ratio or 50 g of elastomer to 5 g primer (SYLGARD® 184 Silicone Encapsulant, Cat. #184 SIL ELAST KIT 0.5KG, Ellsworth Adhesives, Germantown, WI) was added and slowly stirred with the bottom of a 15 ml polystyrene conical test tube. It is very important during this process to not touch the bottom of the plastic dish so as not to cause impurities from the plastic to contaminate the mixture. The PDMS solution was mixed very slowly (to avoid bubble formation) for 10 min. Foil was placed over the top of the PDMS solution so that it could sit undisturbed for 30-40 min. to allow any bubbles to pop. The PDMS was then slowly poured over entire the patterned wafer. The wafer with the PDMS was allowed to stand for 30 min. to allow any bubbles to collapse. Just as before, after the standing time, a sterile 200 μl microliter pipet tip (Cat. #53503-290, VWR Scientific, Chicago, IL) was used to pop any remaining bubbles. The PDMS-coated wafer was hard baked at 150°C for 1.5 h. This step cures the PDMS and allows for the formation of the microchannels to form on what is now the bottom of the PDMS layer. The PDMS covered wafer was allowed to cool completely before the chips were cut out.

To make the chips (bottom and top layers of the tri-layer chip), a single edge straight razor blade (Cat. #S17302, Thermo Fisher) is placed at approximately a 45° angle and then pressed into the PDMS polymer down to the wafer. A rectangular piece of polymer is then traced around with the razor and then gently lifted off the wafer surface. This produces a PDMS chip with the microchannels on the bottom side. Chips were cut out for both the bottom and top layers of the AOC. The middle elastomeric valve layer was generated next. The first thing was to clean a large 3" x 2" glass microscope slide (Cat. #260439, Ted Pella, Inc.) in the Branson barrel etcher with the following settings: vacuum pressure is 1 torr, RF is 200 W, exposure time is 30 s to 1 min., room air intake for oxygen plasma generation. Approximately 500 µl of the SylGard PDMS mixture was placed in the middle of the glass slide sitting on top of the sample chuck in a spin coater (Specialty Coating Systems). The spinner was programmed as follows: Ramp = 5 sec/Dwell = 30 sec/Speed = 1100 rpm. The spinner was run for one cycle. After the spin coating step, the resultant middle PDMS layer is around 100 µm thick (refer to Figure 5.4 where orange arrow points to a corner of the membrane). This membrane must be thin because it is used to keep the control layer away from the sample layer to provide the valve actions. The membrane is baked in foil for 10-15 minutes at 100°C for curing on a hot plate.
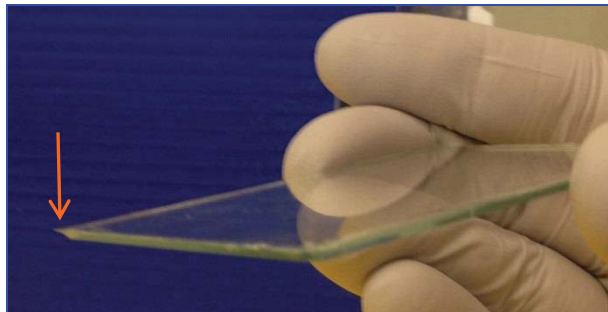
Figure 5.2. 100 μm thick PDMS layer spun onto large glass microscope slide. This will comprise the middle elastomeric valve tier of the Aneurysm-on-a-Chip™ mechanism.

The oxidation of PDMS with plasma is necessary to bind the chips to each other. Oxidation changes the surface chemistry and produces silanol terminations (SiOH) on its surface. In addition, this helps make PDMS hydrophilic – a characteristic rendering the polymer biocompatible. With this in mind, the chips and membrane were oxidized by using a hand-held Corona Treater (Model BD-20AC, Cat. #12051A-10, Electro-Technic Products, Chicago, IL). Immediately after plasma charging, the control layer was hand-pressed onto another plasma-cleaned glass slide with the microchannel side up, and then the PDMS membrane was lifted off its glass slide and subsequently pressed gently by hand on top of the control layer. Every effort was made to ensure that the two layers were completely sealed against each other without any bubbles. The top sample layer was oriented with its microchannel side down and using a Nikon upright brightfield microscope (Eclipse ME600 microscope, Nikon Instruments, Inc.) fitted with a 4X objective, it was aligned onto the membrane and pressed gently into place, again making sure there were no bubbles. The AOC PDMS tri-layered chip was now ready to be integrated with the solenoid valve hardware.

5.2.1.4   <u>Modular Design of AOC</u>

The system set up involved the use of the Nikon Eclipse ME600 microscope (Nikon

Instruments, Inc.) fitted with cameras to take live videos and images. A 4X objective was

employed to view the "aneurysm sac". To obtain the images and generate movies,

MetaMorph® Research Imaging Software (Molecular Devices, Downingtown, PA) and

ImageJ Image Processing and Analysis software (NIH, Washington, D.C.), were used

respectively. The bioMEMS AOC chip was attached to a controller box built by

Microfluidics Innovations as visualized in Figure 5.3. The box houses the solenoid

valves that are used to control the elastomeric valves of the microfluidics chip. The valve

set up is itself connected to the bioMEMS chip via a manifold (see red arrow of Figure

5.4) that has inlets into the chip where the valve control takes place. The manifold is

connected to the controller box by Tygon® ND 100-65 medical tubing with an ID of

1/16", and the vacuum/pressure connections are secured with 1/8" ID tubing (Cat.

#54623 and #54626, respectively, www.usplastic.com, U.S. Plastic Corp., Lima, OH) as

shown in Figs. 5.3 and 5.4.
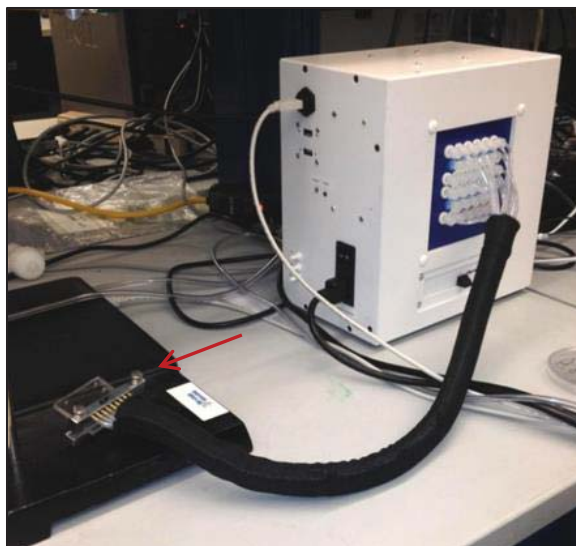
Figure 5.3. Microfluidics Innovations Controller Box showing fluidics ports connected to the manifold and bioMEMS chip (red arrow).

Figure 5.4. Close-up of manifold connected to microfluidic lines (tubing). These lines are responsible for pressure and vacuum going into the bioMEMS chip.

The controller box is coupled to a Dell Inspiron laptop PC (Dell Computer Corp., Round

Rock, TX) running Windows Vista (Microsoft Corp., Redmond, WA) with the Assay

Mark controller software (Microfluidics Innovations, LLC, West Lafayette, IN) installed

on it. The software is proprietary; however, the graphics user interface (GUI) is shown in

Figure 5.5. The basic GUI window that pops up after initialization shows the button to

connect the laptop to the controller box. For all experiments, the "Manual Mode" option

is selected. After the run mode is selected, then the valve GUI (Figure 5.6), pops up and

the user may select whether or not the solenoid valves are open or closed, reversed or

forwarded. Input sample ports (Circles A-E) are where the sample is introduced into the

PDMS microchip, and output ports (Circles X, Y, and Z in Fig. 5.6) are where the

sample can either be sent to waste or collected for further analyses.

Figure 5.5. Assay Mark opening GUI. "Connect" button is used to connect the controller
box to the laptop. The "Manual Mode" button is selected for normal operations.

While there are 40 valves and 8 ports, in reality only valves 1, 2, 3, 6, 7, 8, 15, 16, and 17

are actually operated in the Aneurysm-on-a-Chip™. The red highlights in Fig. 5.6 point

to the position of the valves on the GUI. The software is clickable, so clicking on any of

the valves on the GUI will actuate the corresponding valves in the valve box which in

turn actuate the elastomeric valves on the PDMS chip. The valves manipulating the

bioMEMS AOC device are valves 6, 7, and 8 for the bottom layer, valves 1, 2, 3 for the

middle layer, and valves 15, 16, and 17 for the top layer of the chip.
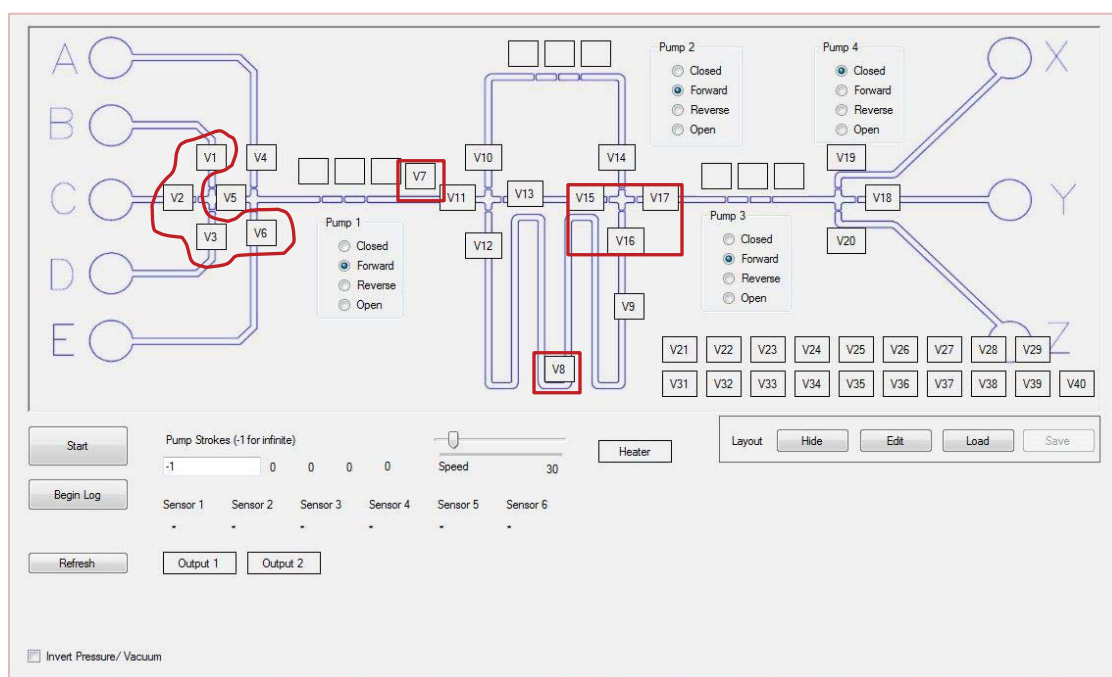
Figure 5.6. Valve control GUI showing samples input ports A-E, output ports X, Y, Z, and valves V1-V40. Red outlines highlight the valves actually utilized in the AOC device.

To summarize the entire AOC setup, the different parts of the overall design are: (1)

Biological sample, (2) PDMS bioMEMS microfluidic chip, (3) imaging device –

microscope and camera, (4) fluidics controller apparatus, (5) software for programming

fluidics controller. Each individual component can be taken offline easily for

maintenance and diagnostics as needed. Since the total schema is modular, each

individual component can be removed from the integrated system to be easily modified

and upgraded.

5.2.2   Scheme 2: Computational Algorithmic Analyses of Samples Flowed Through AOC Prototype

5.2.2.1   Leak Testing

In the first attempt to use the AOC, the aneurysm sac configuration seen in Figure 5.10,

Panel C (see Results Section) was used. 100 µl of yellow food coloring (Canary Yellow

Color, Esco Foods, Inc., San Francisco, CA) was added to 100 µl of nanograde water in a

small test tube. 2 µl was pipetted into a sample port on the bioMEMS chip. The pump

speed was 250 mS per stroke and 10-20 nl of solution is pushed through the

microchannels with each stroke. To create a pulsatile environment, there is a 132 mS

interval between valve actuations. Pressure was set at ~10 kPA and the vacuum was set

at ~ -40 kPA. An 8 mm Pen Shape 300X USB Digital Microscope (AliExpress –

www.aliexpress.com, Alibaba Co., Ltd., Hangzhou, China) was implemented to view the

microchannels and "sac" areas to ensure that the water did not stray out of the

microchannels – a sign that the top layer of the AOC was not sealed properly. Once the

hardware was set up, the "Start" button on the GUI (refer to Fig. 5.8) was pressed and the

colored water was pushed through the AOC. The purpose of this experiment was to

make sure that there were no leaks in the device and that the sample could be pushed

through the entire channel and come out the exit port. The colored water was rinsed out with 10 μl of nanograde water. The colored water trials were performed several more times successfully and a representative image is Figure 5.11. Since there were no leaks and the chip was easily cleaned (verified via microscope), it was time to use polystyrene microbeads in nanograde water to prepare for the bead assay.

5.2.2.2   Testing with Microspheres

The next set of tests utilized 7 μm polystyrene microspheres (Cat. #PS06N/5856, Bangs Laboratories, Inc., Fishers, IN) in nanograde water. It is very noteworthy to mention that 3% bovine serum albumin (BSA) was utilized for all fluid flow assays. 10 μl of BSA was run through the microchannels to ensure that no beads and cells would clump together and cause fluid flow difficulties. For the experiments, 100 μl of beads were diluted into 100 μl of water and 2 μl of this solution was pipetted into one of the microchip's sample ports. All the same settings were used as described for the colored water experiments. A vector graph was developed to view the fluid flow of the microspheres. The graphic output will be discussed later. The software used for this experiment was generated by Dr. Steven Wereley (Professor, School of Mechanical Engineering, Purdue University). Dr. Wereley provide the analysis.

In another set of analyses, three different flow speeds were used: 1 mS, 10 mS, and 100 mS. An air bubble was introduced into the sac to determine what impact it might have on the flow, if any. The bubble was actually a happy coincidence, as it occurred after the

PDMS top layer had to be pulled off the middle layer to thoroughly clean the

microchannels of microspheres that were stuck along them from the previous assays.

When the chip was reassembled and pressed by hand, a bubble was seen after colored

water was sent through to check for leaks. The size of the bubble was about 450 μm in

length by 150 μm wide. It was decided to keep the bubble in place and not pop it so as to

see what an obstruction would do to the flow of particles. All other settings were the

same as before for the bead runs. In addition, photomicrographs were taken using 5MP

color digital CCD camera (USB3.0, real-time live video, AmScope.com, Irvine, CA)

camera and particles were counted in the sac region using the particle count plugin in the

ImageJ (NIH) software. The plugin uses an edge detection subroutine where a .TIF

image is converted into an 8-bit image and then the edges are detected to find the

particles. The threshold is set so that the microspheres can be detected. A bit map

boundary is next set for the counting region and a histogram is generated for each

photograph to enumerate the counts and statistics within the bounded region.

Microspheres and colored water were successful. The next logical step was to flow the

HASMC.

5.2.2.3   Computational Algorithmic Analyses on HASMC

5.2.2.3.1   PIV Analysis

Initially, to run the cells, HASMC were grown as usual and harvested at about 90%

confluency with a density at $1x10^5$ cells/ml. The size and density of particles must be

carefully considered to ensure that the particles will closely follow the direction of fluid

flow. Therefore, to increase the amount of sample, the same polystyrene microspheres

used previously were added to provide a total density of 1 x 10^7 particles/ml. One

problem from the previous experiments was that some particles appeared as smears (see

Figure 5.12) and could not be resolved to obtain individual units. To solve this problem,

a Nikon Eclipse ME600 microscope (Nikon Instruments, Inc.) with a 4X objective was

used as stated earlier, but this time the microscope was fitted with a Photometrics

CoolSNAP™HQ camera (Photometrics©, Tucson). This camera allowed for the

elimination of smears and streaks and resolution of individual particles flowing through

the bioMEMS device. The following were the imaging specifications: image resolution

was 512 x 512 pixels, frame rate was 500 frames/s, interframe time was 2 mS, pixel size

was 3.33 x 3.33 μm2, and a binary mask was applied to the images for efficient

computation. The inlet velocity of the microchannel into the "aneurysm sac" was

5092.96-10185.92 μm/s. 10 μl cells/beads in PBS was introduced into the bioMEMS chip

and the system was run at the same settings as before, but with a 30 mS pump speed. For

particle image velocimetry (PIV)) analysis, a total of 6,359 images were taken and the

pictures chosen to report on were Image #2215 and #2216. This pair of pictures was

selected because they showed the particles clearly moving throughout the "sac".

PIV (particle image velocimetry) is a flow measurement method that computes the

velocity field of a sample flowing through a contained area [117]. It works by using a

pattern recognition algorithm on paired consecutive images to establish the shift of

particles inside the fluid flow. To do this, images must be separated by minor time

intervals since this allows for temporal statistics to be obtained over a spatial region.

Two subsequent images are selected as pairs for analysis and an interrogation area is

designated – in this case, the area is inside the "sac". Within the interrogation area, a grid

is used to determine the location of the particles. The cells of the grid are "windows" and

window resolution provides the spatial resolution (number of pixels devoted to comprise

a digital image) of the velocity vectors when the results are computed. The grid size

specifies the center-to-center distance between adjacent cells of the grid. The correlation

between the interrogation areas in both images is computed and displacement is

determined from the location of the correlation peak. It is important to observe that the

cells can overlap if the grid size is less than the window size. For the data given in this

typescript, the PIV specifications were: window resolution was 32 x 32 pixels

(containing 15 particles), grid resolution was 8 x 8 pixels [118], interrogation overlap

(compensation since grid size is less than window size) was 75% vertically and

horizontally between the paired images, correlation type was robust phase correlation

(RPC) [119]. The subpixel correlation peak location is the three point Gaussian estimator

[117] which uses a function to fit correlation data. This method uses only 3 adjoining

values to estimate a component of displacement [117].

In PIV, it is essential to comprehend that Bernoulli's equation is used to obtain velocity

components where U is the velocity of the vortex flow and V is the fluid flow speed

[117]. Vectorgraphs (quiver plots) are derived from the calculations and they display

velocity vectors as arrows with components (U, V) at the points (X, Y). The equations

for the velocity components as functions of X, Y, and Z coordinates are:

$$U = |\mathbf{U}_{\text{max}}| \frac{1}{\sqrt{2}\,0.2}$$

$$V = -|\mathbf{U}_{\text{max}}| \cos\left(\arctan\left(\frac{Y}{\Delta Y}\right) + \alpha_0\right) \frac{\Delta Y}{\sqrt{\Delta Y^2 + Y^2}}$$

$$W = -|\mathbf{U}_{\text{max}}| \sin\left(\arctan\left(\frac{Y}{\Delta Y}\right) + \alpha_0\right) \frac{\Delta Y}{\sqrt{\Delta Y^2 + Y^2}}.$$

In addition to the previous defined variables, U_{max} is the maximum velocity of the vortex

flow, W is the interrogation window, $\alpha_0 = \pi/4$ and is assumed so that V = 0 at the upper

left corner of the observation area, and W = 0 at the lower left corner [117]. The matrices

X, Y, U, and V must all be the same size and contain corresponding position and velocity

components. By default, the arrows are scaled so as not to overlap each other. Quiver (U,

V) draws vectors specified by U and V at equidistant points in the X-Y plane. In

summary, the first velocity vector is described by U(1), V(1) and is presented at the point

X(1),Y(1).

To analyze the collected images, a software program Prana Windows v1.0.1 Beta [120]

was used [114–118]. Prana is a MATLAB® freeware PIV tool that implements the RPC

kernel for PIV analysis. Robust Phase Correlation (RPC) is used to detect displacement

of image patterns and is a modified form of the standard General Cross Correlation (GCC)

method. GCC determines the translational shift of the flow by convoluting the inputs

from the two pair of images while RPC adds a spectral filter to GCC. The spectral filter

uses a novel algorithm to analytically model the signal-to-noise ratio and also

computationally amplifies it [121, 122]. Outputs of the PIV program provide

vectorgraphs of particle flow showing arrows pointing in the direction of flow for each resolved particle.

5.2.2.3.2 WSS Analysis

For WSS calculations, MATLAB® the quiver plots were achieved by inputting the following command line: "quiver(X,Y,shearstressx,shearstressy)", without the quotes. In the representative trial given in this manuscript, a total of 6,359 images of flowing cells and beads were captured and saved for evaluation offline. Only images that reflected the most turbulent movement of particles were chosen for analysis. For WSS determination, there were a total of 621 X vectors and 621 Y vectors for a total of 1,242 vectors. The vectorgraph provided in this report is for the outward edges of the flow (WSS_x_6336.mat, WSS_y_6336.mat) to observe how the particles behaved at the outer boundaries of the "aneurysm sac". The output vectorgraph was saved as a JPEG file.

5.3   Results

5.3.1   Scheme 1: AOC Design and Synthesis

5.3.1.1   Mask Design of AOC Chip Device

Figure 5.7 shows the finalized mask design for the Aneurysm-on-a-Chip™ system. The bottom stratum (fluidics control layer, refer to Fig. 5.1) is represented by the red box. This section of the chip is actually connected to the pneumatic valves box through tubing. The middle elastomeric valve layer (check out to Fig. 5.1) is highlighted by the orange

arrows. The PDMS membrane making up the middle sheet moves up and down as controlled by the fluidics control layer (i.e. the pneumatic valves). The top tier (pneumatic sample layer) is represented by the green arrows. The green arrows specifically point to the three configurations of aneurysm design. Sample is introduced into the device at this level and travels through the microchannels symbolized by blue lines in the picture. It is of note that the microchannels that are made are rectangle-shaped and ~5 mm in length.
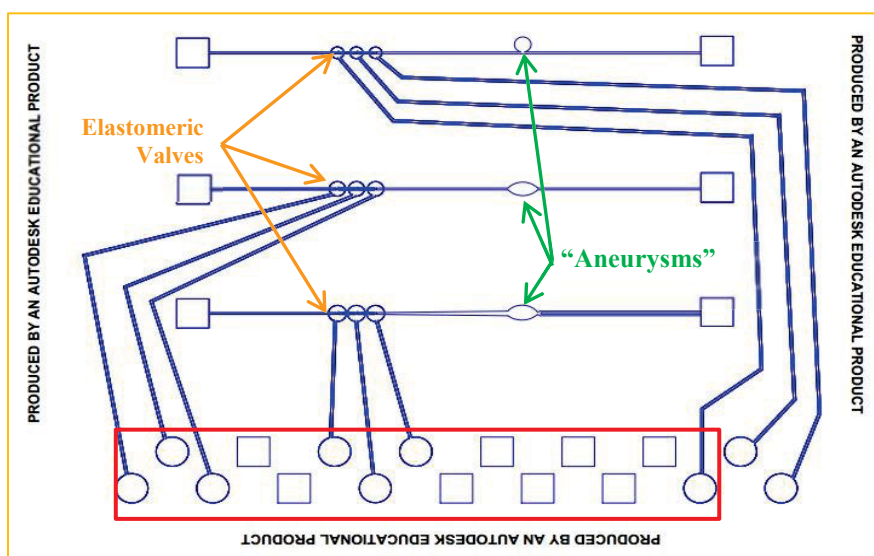
Figure 5.7. Mask design of AOC device. Red box is control layer: open circles - valves, squares - spacing on mask design, orange arrows - elastomeric valves, green arrows - "aneurysms". Squares on upper left are input ports, squares on upper right are output ports. Blue lines are the microfluidic channels.

5.3.1.2   Preparation of Silicon Wafers

The entire box of Si wafers was taken through the wash steps, while the mask was

actually exposed on duplicate wafers. This was a necessity because during the first cutting of the PDMS chips, one of the wafers was cracked and rendered unusable. All Piranha-cleaned wafers remain in the cleanroom until ready for further processing which picks up at the mask exposure stage.

5.3.1.3   <u>Synthesis of PDMS Chip</u>

5.3.1.3.1   Pattern Development on Wafer

The pattern on the duplicate wafers was developed successfully as seen in Figure 5.8. The blue square bounds the bottom controller layer of the AOC bioMEMS chip. The other patterns represent other aneurysm configurations that could be used for other analyses, but not on the current AOC PDMS chip. It is common to place patterns from different devices/systems on one wafer, since there is a lot of real estate there and wafers do cost time and money to process. Patterned wafers are stored at room temperature and can be used over and over again as long as they are handled with clean gloved hands and are not cracked or chipped across the pattern needed to be employed. To generate new chips over used patterns, liquid PDMS polymer just needs to be poured over the pattern and allowed to cure.
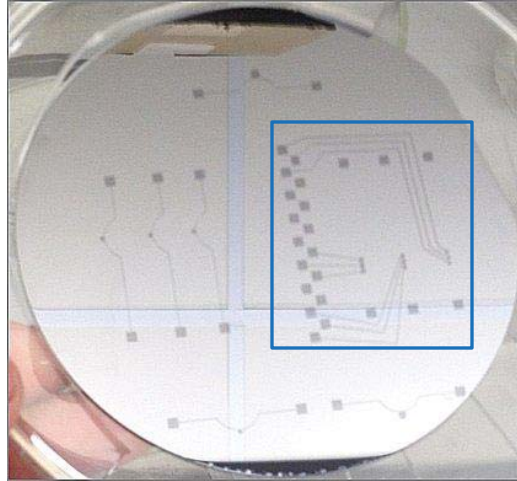
Figure 5.8. Developed pattern on coated silicon wafer. The blue box highlights the region showing the bottom control layer of the tri-layer AOC design. The other patterns are for supplementary experiments.

5.3.1.3.2 PDMS Chip Fabrication

When the individual PDMS layers were aligned and pressed together they became one unit – the AOC bioMEMS chip as depicted below in Figure 5.9. While a bit difficult to see, the aneurysm sac, and ports of the top layer are nicely aligned over the microchannels and valves of the bottom tier. The "invisible" middle layer now comprises the membranes of all the valves in the structure. For a better view of elastomer valves and the aneurysm sac, please see Figure 5.11 below. There are actually three configurations of "aneurysms" on the same chip that should be mentioned.
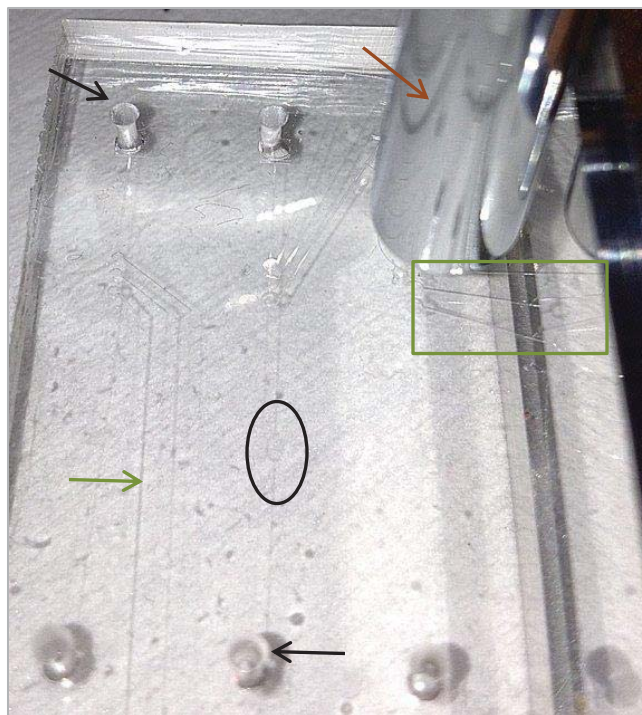
Figure 5.9. Assembled tri-layer PDMS AOC chip under microscope. Top layer: Black arrows – inlet/outlet ports, black oval – fusiform "aneurysm". Bottom layer: Green arrow – microchannel, green box - valves. Orange arrow – microscope objective.

Figure 5.10 shows three different PDMS configurations of PDMS "aneurysms" that are used to flow material. In Fig. 5.10 Panel A, the orange lines represent a bifurcated blood vessel with each microchannel at 25 μm diameter, while the blue line where the two channels converge to form a neck region is 50 μm across. The single microchannel on the opposite side of the aneurysm sac is 100 μm in width (yellow line). Finally, the vertical diameter of the aneurysm sac represented by the vertical purple line is 450 μm across and the horizontal diameter represented by the green line is 800 μm in length. In Panel B, the yellow line signifies an aneurysm neck that is 100 μm across, the blue line shows a microchannel that is 75 μm in diameter, and the purple and green lines for the

vertical and horizontal diameters across the sac are 350 μm wide. Looking at Panel C,

there are single microchannels leading into and out of the sac at about 75 μm in size (blue

lines) while the vertical diameter of the sac is 300 μm (purple line) and the horizontal

length is 800 μm. The oval shape of two of the "aneurysms" seen in Panels A and C is a

mockup of the fusiform aneurysms that have a gradual, progressive outpouching. The

round "aneurysm" represents berry aneurysms. The dimensions for the AOC were

determined so as to allow 10 μm cells to flow through the channels to simulate the actual

live human blood vessel.
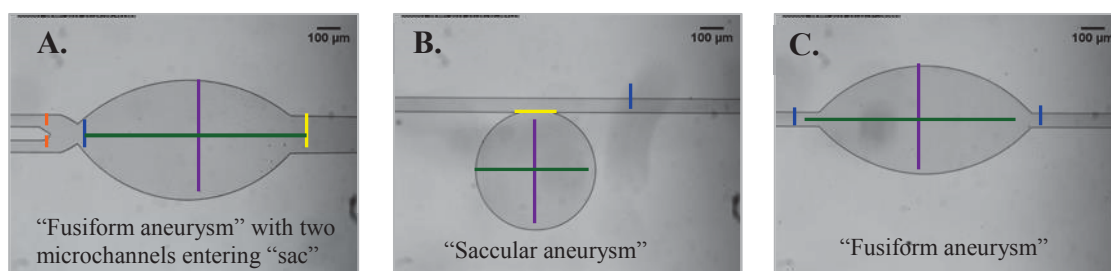
Figure 5.10. Three configurations of "aneurysm sacs" in the AOC microfluidic chip.
Lines

5.3.1.4 Modular Design of AOC

The Aneurysm-on-a-Chip™ was fabricated to be modular – to use different PDMS chips,

different microscopes, and different samples containing particles in solution. The entire

apparatus can easily be broken down into 4 parts: 1) PDMS chip, 2) manifold, 3) valve

controller hardware box, and 4) software installed on laptop. The software is also

designed to allow for the adjustment of pump strokes and pump speeds. The direction of

fluid flow can also be reversed in software. The complete system can easily be moved

from one lab and set up in another. While the larger Nikon microscope with high-speed

camera cannot fit into a biological safety cabinet (BSC), the smaller pen-shaped

microscope can easily be placed inside a BSC along with the hardware box connected to

the PDMS chip for BSL2 assays.

5.3.2   Scheme 2: Computational Algorithmic Analyses of Samples Flowed Through AOC Prototype

5.3.2.1   <u>Leak Testing</u>

Figure 5.11 shows the yellow water inside the AOC. Panel A shows the entire

microchannel highlighted in yellow where the aneurysm sac (purple oval) can easily be

seen. In Panel B, the yellow water is seen being pumped out – a nice feature that can be

exploited to recover sample for further testing and analysis. Further, the fact that the

water is evident in the output port (black arrow) proves that the valve system works (red

oval). It is equally important to note that the yellow water is completely contained within

the microchannels. There is no evidence of the sample leaking through any other part of

the chip – definite proof that the tri-layer design is robust and the sealing technique is

efficacious. Incidentally, the bottom and top layers can be distinguished easily in this

figure (blue arrows).

It is important to talk about the manifold (yellow arrows in Panels A and B of Fig. 5.11).

This component is an integral piece of the AOC system. As can be seen in Fig. 5.4 in the

Materials and Methods section, the manifold is the metal holder connected to tubing for

the air and vacuum lines to push liquid through the microchannels. This single

component facilitates the introduction of sample into the bioMEMS chip and by simply

opening the screws, the chip can be removed and another one easily reinserted. This

setup eliminates the need to insert microtubing for sample introduction directly into the

sample port of the chip and the implementation of syringes and syringe drives for moving

the fluid along the microchannels. Each tubing is connected to a solenoid valve inside

the drive controller box (Fig. 5.10), and since the pressure and vacuum is actuated in

software, the tubing that is not activated remains simply inert. This feature eliminates the

necessity of connecting and disconnecting tubing on other PDMS chip archetypes, or

trying to plug up unnecessary existing tubings not required for an experiment.
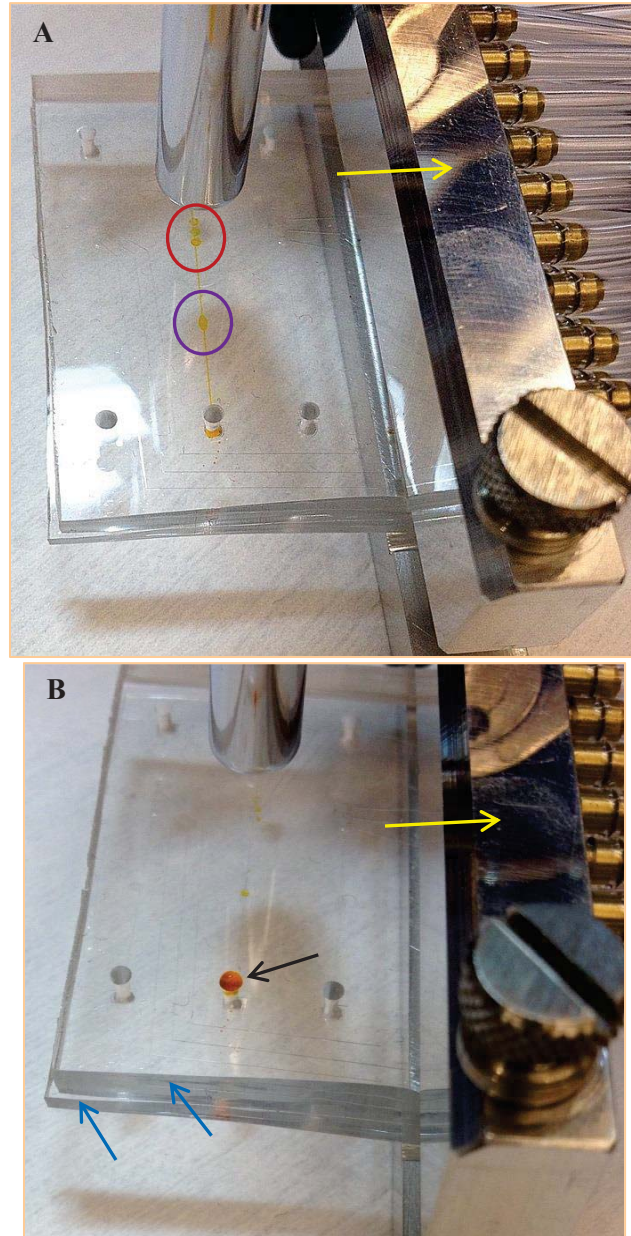
Figure 5.11. PDMS AOC bioMEMS chip leak test. Panel A shows yellow water inside device: red circle – valves, purple circle – aneurysm sac. Panel B is output port with liquid drop coming out. Yellow arrows in both panels point to the manifold.

5.3.2.2   Testing with Microspheres

The microspheres experiments were performed to test the system. Specifically, it was

important to determine how well the beads flowed through the aneurysm, what problems

might be encountered, and how well the camera could resolve the individual particles. Dr.

Steve Wereley (School of Mechanical Engineering, Purdue University) provided the

analysis seen in Figure 5.12 - a vector graph of the beads as they are flowing inside the

"aneurysm sac".
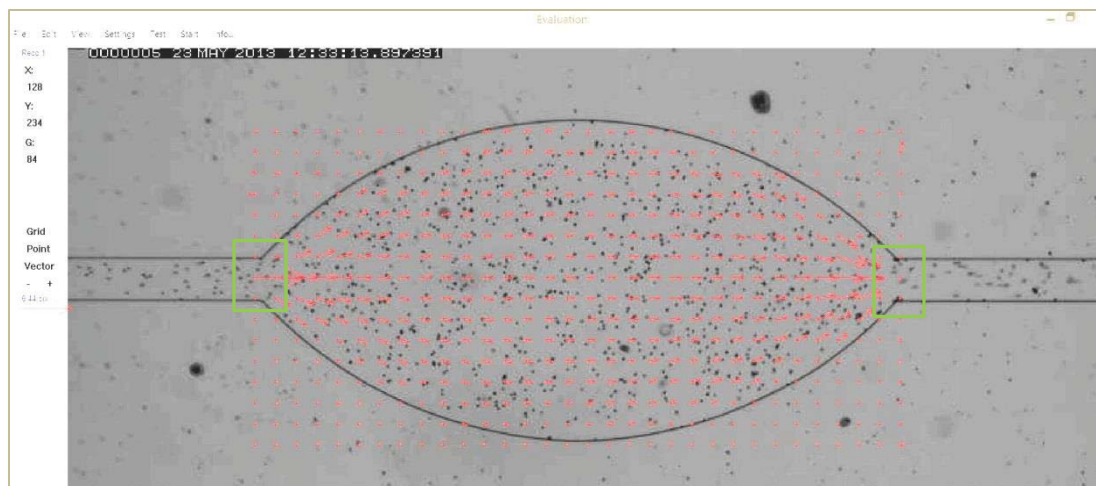
Figure 5.12. Vector graph of microsphere flowing from left (inlet) to right (outlet). Red
arrows show how the particles are travelling both toward the outer edge of the "sac"
(green boxes) as well as straight through the "sac".

The second set of trials involved the beads but three different pump speeds as described

formerly. Figure 5.13 shows the 7 µm microspheres flowing through the sac of the AOC.

Panel A is 1 mS pump speed, Panel B is 10 mS, and Panel C is 100 mS. The clear area

seen at the bottom of each image is an air bubble (yellow ovals, Panels A, B). The

experiments were to see how well particles would flow with an obstruction (air bubble)

and to determine how many particles could be contained within the sac.
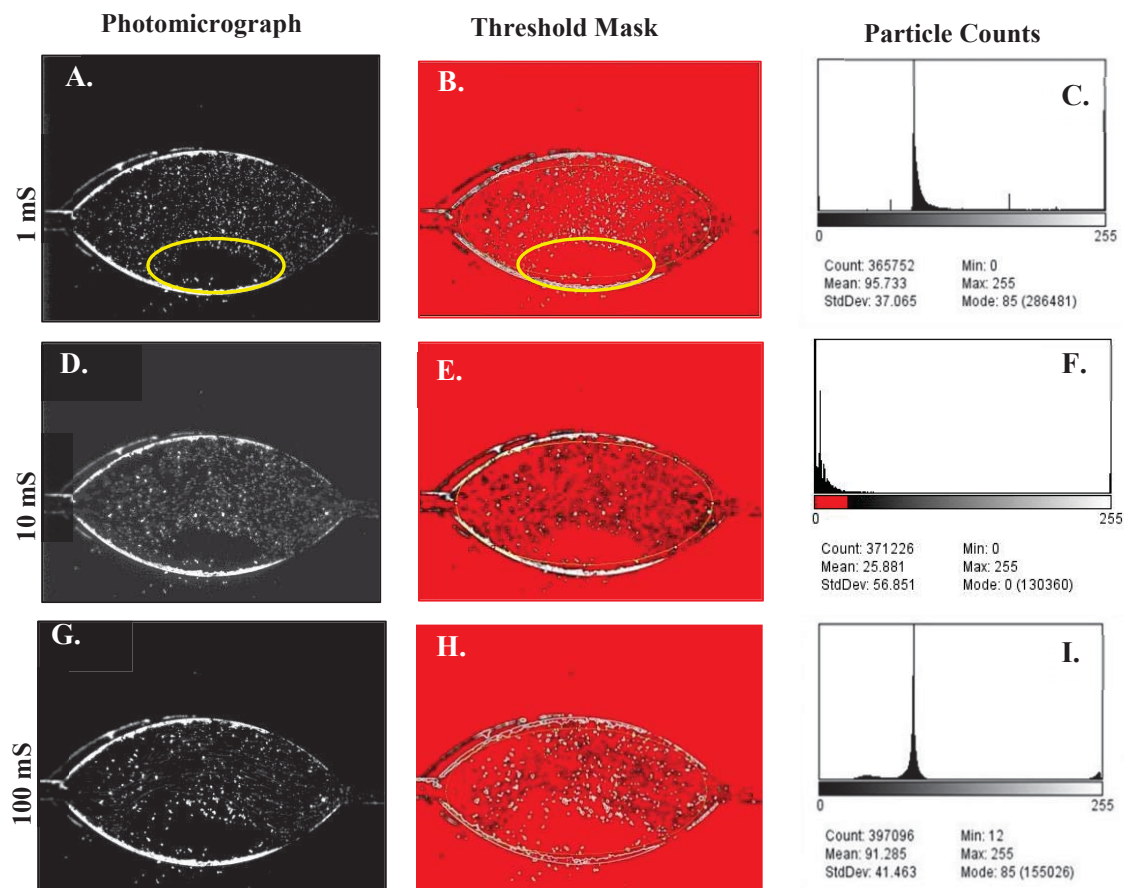
Figure 5.13. Particle counts inside the "aneurysm sac". Panels A, D, and E are photomicrographs of microspheres flowing through aneurysm sac at pump speeds of 1 mS, 10 mS, and 100 mS, respectively. Panels B, E, and H are the threshold masks of the photomicrographs. Panels C, F, and I are the particle counts and statistics calculated from the threshold masks. Yellow ovals show bubbles in Panels A, B.

The edge detection program of the ImageJ plugin provided the following data. For a pump speed of 1 mS, a total of 365,752 beads were counted. By increasing the pump speed by a factor of 10, a total of 371,226 particles were counted, and increasing the speed by another factor of 10 (100 mS) yielded 397,096 microspheres. Overall the trend was increasing the bead count by approximately 20,000 units for each increase. There

were no aggregation of particles and each time the beads freely flowed through the device. Even with the obstruction, the experiments proved that the device worked. The one drawback was that the counts were not entirely accurate because ImageJ could not resolve any individual particles seen inside the blurred streaks of flowing microspheres. The only way to get around this issue is to use a high speed camera. Even though the analysis had a lot to be desired, it did provide substantiation that the device was operating properly with little issues that frequently occur in microfluidics devices such as agglomeration of particles leading to the plugging up of microchannels. Further, with the increase in the pump speed, the seal of the three tiers of the PDMS bioMEMS device held and no leakages or outflows occurred.

5.3.2.3 Computational Algorithmic Analyses on HASMC

5.3.2.3.1 PIV Analysis

Beads and HASMC were run through the fusiform "aneurysm" as communicated earlier. Figure 5.14 shows the combined images 2215 and 2216 with the direction of flow indicated from right to left.
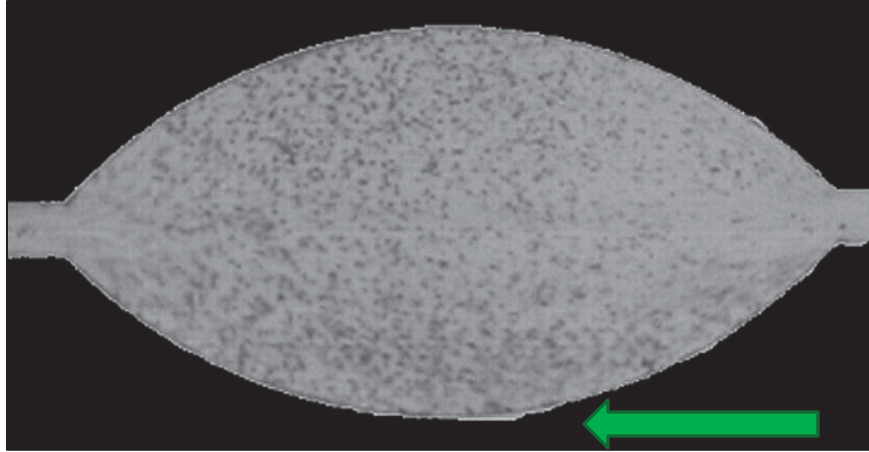
Figure 5.14. Combined Images #2215 and #2216. HASMC and microspheres are flowing inside fusiform "aneurysm". The direction of flow is indicated by the green arrow.

To elucidate the fluid flow patterns from the paired images, PIV analysis yielded the vectorgraph seen in Figure 5.15 below as generated by MATLAB® Prana software. The blue arrows indicate the travel of the particles imaged. It appears that there may be no cells or beads in the area bounded by a red circle. This was evident in all acquired images; the density of particles decreases at the input port, and increases at the output port as particles are pushed together toward the exit. The results show that the cells flow easily through the device and the straightforward pattern of flow shows that the fusiform configuration with the sample exhibits no turbulent flow. What this does not show is the wall shear stress forces.
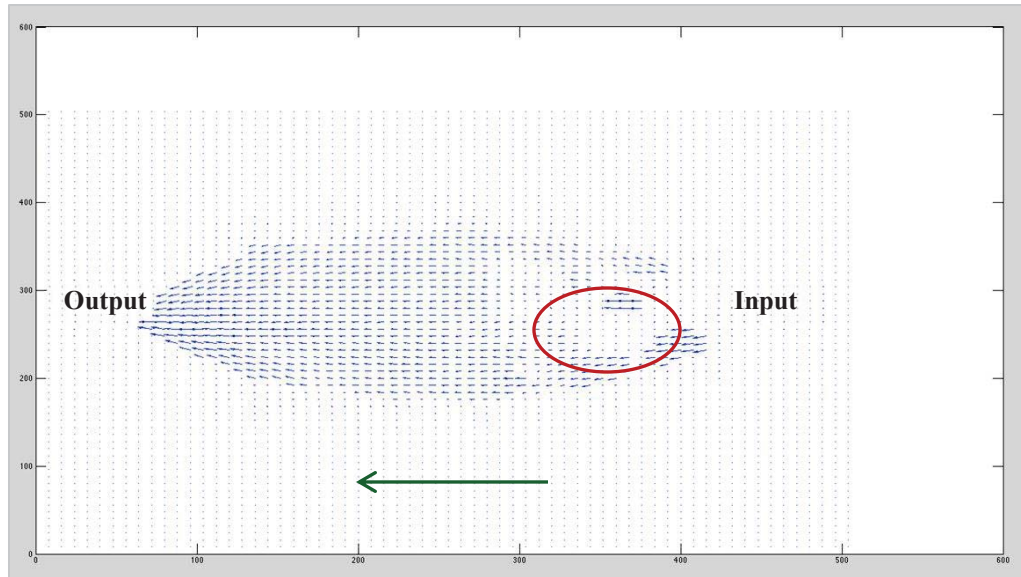
Figure 5.15. MATLAB® PIV vectorgraph of HASMC and Microspheres (refer to Fig. 5.14 above). Green arrow shows direction of flow from input to output.

5.3.2.3.2 WSS Analysis

MATLAB® was used to generate the quiver plot as represented in Figure 5.16. The purple line is the direction that the fluid is flowing. The black arrow is pointing to an area where there are two vectors that are flowing backward. This would cause some turbulence. This was evident in several vectorgraphs.
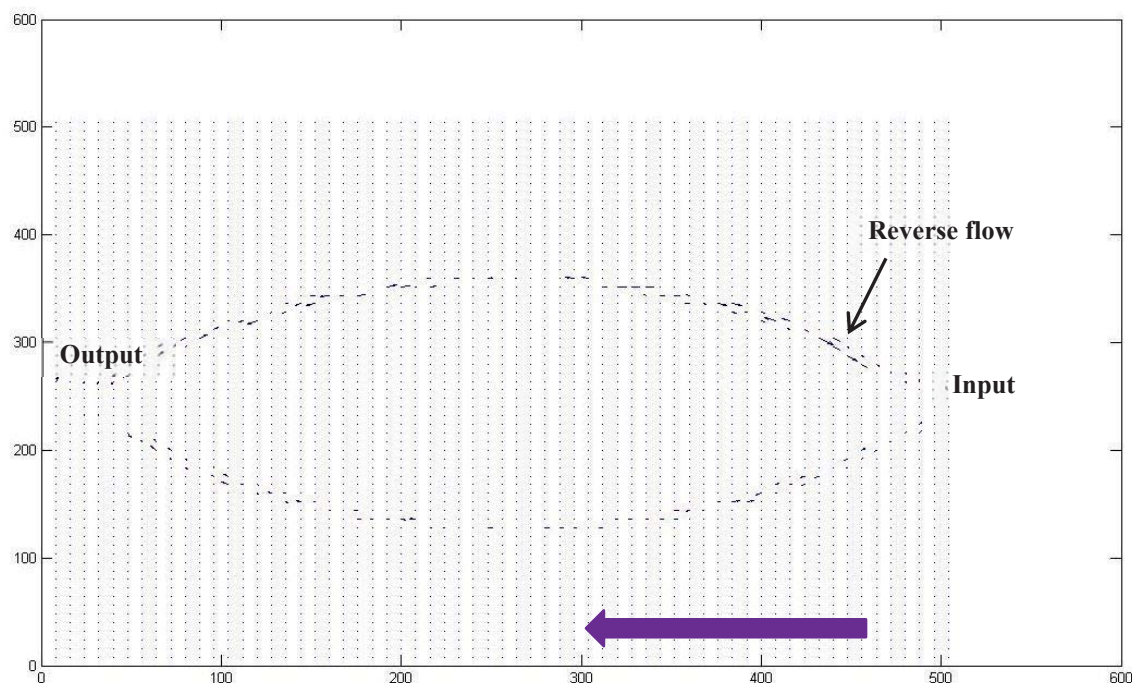
Figure 5.16. MATLAB® WSS quiver plot for HASMC/microspheres assay. Arrow is pointing to region of reverse flow. Purple line depicts direction of fluid flow.

5.3.3 Brief Summary of Results

Results thus far were from the fusiform aneurysm configuration with single input and output. The soft lithography process was perfected to allow for successful PDMS chip manufacturing. Testing of the bioMEMS device was pursued logically: first testing to ensure there were no leaks and all components worked together, to running polystyrene microspheres, and culminating in running fixed HASMC mixed with the beads. PIV results showed that the general flow of the cells/beads was efficacious from input to output. This may be because the microchannels and "sac" were first rinsed with 3% BSA to avoid the problem of particle clumping. It must be reiterated that there was a clear

space in the sac where there appears to be no particles. This was observed in all acquired images and could be the result of the pulsatile flow.

The WSS shows that there was some back flow around the edge and this showed up in all the images acquired. The berry aneurysm configuration was tried with beads only and it immediately clogged. The bioMEMS chip had to be disassembled, cleaned, and reassembled to attempt the flow experiment again. The same result occurred and the chip had to be recleaned. The other fusiform "sac" with the bifurcated microchannel, had issues with a clog at the input port. Attempts to clean have not been successful. Overall, the fusiform sac configuration proved to be useful in analyzing fluid flow.

5.4   Discussion and Conclusions

The PDMS bioMEMS AOC device was generated using basic soft lithography techniques. Wafers were processed and masks made inside a Class 100 cleanroom area while the PDMS chip synthesis was performed on a lab bench in a standard laboratory setting. It is imperative that during the mask making step, the environment be extremely clean and that the PDMS process be carried out carefully to avoid bubbles and contamination for plastic containers and the mixing tube. It is equally important to understand how fragile the patterned wafer is and that it can be fractured during the cutting step, when one is trying to cut the PDMS chip resting on top of the desired pattern. It is also imperative that once the Corona plasma step be done, the immediate pressing of the layers must be performed for complete sealing together of the polymer tiers.

The entire AOC device is modular and can be unassembled and reassembled with relative ease. The device can be used with most any type of microscope and the software can be installed and used on Windows Vista and Windows 7 platforms. Microfluidics Innovations is a company that manufacturer's the hardware box containing the solenoid valves. The company not only provides the box, but also the tubing connections and the manifold that is specifically designed for the PDMS chip the customer has designed. The tubing can be disconnected completely from the box and manifold, but this is not necessary once things are assembled. The manifold and tubing can be autoclaved if needed. The ease of which the PDMS chip can be changed out is a plus because the manifold is just loosened by the screws, then the old chip is slid out and the new one is installed. The microchannels are viewed using standard microscopy techniques and as long as a high-speed camera is utilized, then effective fluid flow measurements may be achieved.

The high-speed camera was needed to resolve the streaks seen in earlier experiments. Once that was accomplished then the PIV and WSS could be calculated and vectorgraphs produced. The PIV and WSS measurements show that particles flow without clumping or aggregation even with pulsatile flow. The WSS, however, shows that there was some reverse flow that could be problematic if the density of particles were increased. It is this type of data that may be useful in predicting aneurysms in human patients. While the flow patterns could be established, there was an area in each image where no particles could be detected. This may be an artifact from the pulsing motion of going forwards

and then backwards. The particles seem to be grouping together more toward the output

after the push forward. This too, may be an issue in a human blood vessel.

CHAPTER 6. CONCLUSIONS

6.1   Comprehensive Summary

Aneurysms are usually treated with coils, stents, or clipping. While these are effective

methods of treatment, all carry advantages and disadvantages. It has long been held that

the development of a bioactive stent device be made that would allow cells to be

recruited to it so that the neck of the lesion be sealed off. The bioactive stent should be

made of a biocompatible material that would not only enhance the cells' abilities to

proliferate, but would also be able to recruit cells to itself. In this vein, the static

bioactive stent using bacterial nanocellulose (BNC) was developed. The static device

does not disclose whether the cells are capable of being recruited successfully or not

giving the constraints of the aneurysm and blood vessel environment. For this part of the

puzzle, the active Aneurysm-on-a-Chip™ (AOC) was created. The AOC is a proof-of-

concept device that can show how particles (cells) can potentially move inside a

microchannel (i.e. blood vessel) and throughout the "aneurysm sac". The AOC must be

able to provide analytical proof that particles are flowing in one direction and without

hindrance. On the other hand, the AOC must show if the particles/cells are flowing in a

turbulent pattern. Fluid dynamics are important in the development of "initiation, growth,

and rupture of" aneurysms as a result of computational fluid dynamics (CFD) modeling

and patient study [123]. Therefore, the AOC is able to provide preliminary data on fluid flow within a bioMEMS environment.

The work presented in this dissertation demonstrates proof-of-concept of both type of bioactive stents: the active and the dynamic stent devices. The static bioactive stent prototype is comprised of a standard nitinol stent acting as a scaffold to a covering of BNC – a natural, biocompatible fibrous matrix already used in wound healing. BNC is already used in would healing and is easy to make and can be configured to render any size and shape needed along with any pore size required. With the integration of magnetic NP, the pore sizes can still be kept to accommodate fluid flow and the movement of cells through the BNC matrix. The static prototype has been shown to successfully provide a suitable growth substrate for the human aortic smooth muscle cells (HASMC) by evidence of strong F-actin detection and high viability counts that characterize this cell type. The BNC was rendered magnetic by the successful impregnation of iron oxide nanoparticles (IONP) that were themselves coated with PEI, PEG, and citric acid to confer biocompatability. To see if there were any ferromagnetic properties of the MBNC, magnetically labeled HASMC were shown to proliferate around the edge of a piece of MBNC. While not complete evidence of the fact, this preliminary data is intriguing because it shows the great possibility of providing a substance that can actively attract cells to itself – one of the goals of the bioactive stent system. The BNC was shown to grow in the presence of the nitinol stents in both the horizontal and vertical configurations; however, the BNC was not fully incorporated into the stents and was easily removed. This is not acceptable. A bioactive stent made of a nitinol stent and

BNC or MBNC must remain intact during deployment into the human body and during placement.

Soft lithography methods were employed to generate the bioMEMS AOC prototype. Microfluidic Innovations (MI) was the company who helped design the hardware portion of the system: the valve controller box and the software that controls it. MI's software has the ability to control all valves, allow for forward and reverse flow, and determine fluid flow speed. All components of the AOC are modular and can be assembled and reassembled with ease and swiftness. Most any microscope can be accommodated and the latest Windows platforms will support MI's software. Different PDMS chips can be interchanged easily, and the PDMS chips, manifold, and tubing can all be autoclaved for sterility. In regards to the scientific value of the instrument, the dynamic AOC was successful as it provided proof of fluid flow properties for HASMC mixed with polystyrene microspheres within the device. The mixture was flowed and movies and images captured. Particle image velocimetry (PIV) Vectorgraphs were generated and analyzed to provide graphic evidence of the particles movement entering the "sac" region, exiting the "sac", and flowing through the "aneurysm sac". The images taken showed that during pulsatile flow, the sample particles did not agglomerate or stick together and remained monodispersed. Further, the wall shear stress (WSS) quiver plots reflected that there was back or reverse flow of the particles. This is a very important piece of information since it is flow patterns such as this that can be detrimental to a weakened blood vessel in the human body.

6.2   Future Work

6.2.1   Improvements to the Current Static Bioactive Stent Device

The use of BNC in the static bioactive stent system is logical because it is already

biocompatible and used in medical practice. It is easy to make and can grow on a sterile

nitinol mesh. The major drawback is that the BNC does not remain incorporated into the

NiTi matrix. The BNC always grows on the boundaries of the air-liquid interface, so to

embed the BNC throughout the entire NiTi stent would require a different method of

incorporation. Electrospinning, layer-by-layer growth assembly, or polymer sleeve

braiding [112] are all methods that would need to be tried so that the BNC remains

"glued" in place into the nitinol mesh and allow for NBC to fill the spaces between the

NiTi mesh pores. These procedures would have to be proven effective both BNC and

MBNC biomaterials. In addition to the incorporation of the two types of materials to

each other, sterility must be conferred, so UV irradiation and autoclaving must be tested

to see which of these methods would confer sterility without compromising device

integrity.

6.2.2   Improvements to the Current Dynamic AOC System

First, it should be understood that the soft lithography process as well as the PDMS chip

synthesis is optimized and repeatable. These procedures have been in place and used

many years. The hardware and software are also very well produced and tested.

Therefore, the focus of improvement must lie upon the design of the mask. As

mentioned before, there were three designs of "aneurysm" that were produced, only one

configuration, however, was utilized for this research. The reason is that the other two

designs had some flaws. The berry aneurysm design immediately had clogging problems. The microspheres aggregated around the sharp corners of the "sac" that were located on either side of the "aneurysm neck". In real life, there are no sharp corners in any blood vessel or aneurysm, so this is not a good design for a berry aneurysm. The bifurcated fusiform motif also was tried with beads; however, clogs with the twin entry ports were a problem. While the tri-layer chip was easily disassembled, cleaned, and reassembled, the PDMS chip was troublesome in the realigning step as it had to be performed under a microscope. While this was acceptable for a non-sterile unit, if things had to be run under aseptic conditions and within a biological safety cabinet (BSC) and accommodating the existing high-speed camera, this could not be done with the present setup. The addition of the high-speed camera on top of a standard microscope is taller than the inside of a BSC. Another modular design may need to be considered, such as the use of and EVOS® imaging system (Life Technologies, Inc.), where the microscope and computer are combined into one nice compact benchtop unit. The EVOS® FL Imaging System can perform both fluorescence and brightfield imaging and the monitor folds down so that the entire piece of equipment fits inside a BSC. Combining the EVOS® with the MI unit would provide a powerful way to image particles flowing through the AOC device, provided the pump speed was set very low to avoid streaking in the captured image. If a small high-speed CCD camera were to be added to the configuration, then the problem is solved and sterile conditions with actively growing cells (instead of dead fixed ones) could be obtained and studied.

The combination of the static device with the dynamic system could not be tested using the current design. The first idea was to use a piece of BNC-covered NiTi stent and place it into the neck region of the PDMS chip aneurysm conformation. With such small dimensions in the microchannels, this was impossible to do without completely occluding both the "sac" and microchannels. Pieces of BNC could be utilized by themselves in the stent's place, however, there would be no way to secure the BNC and during flow, it would either be stuck in a microchannel downstream, or simply not budge and completely block the microchannels *in situ*. Another scheme that was considered was to place HASMC directly across the aneurysm neck region by themselves, since cells have been shown to grow in place in PDMS chips successfully. However, this could not be executed because there was no way to place a bolus of cells exactly into the neck area. If the chip were to be taken apart to add the cells by pipet, then this would have required a microscope to be placed into a BSC and the operation be performed under sterile conditions. It would be impossible for this since the microscopes available were too large to fit into a biohood. Even if this step were completed successfully, then to press the PDMS layers back together would require the death or damage of the cells. The solution to this would be to develop an inlet port just for the cells, however, the port diameter would have to equal 50-75 μm in diameter (the sizes of the neck regions) and there would still be no way to make sure that the cells would not migrate from the initial seeding spot into the "sac" and microchannels. A complete redesign must take place to take into account all the listed anomalies. One way to answer all the problems would be to make a more micro model via 3D printing so that there would be no sharp corners, cells could easily be seeded, and stents could be utilized. The problem here would be that

things would no longer be at the microscale, but more on the macroscale. Having said all of this, it is still noteworthy to state that should the complications be resolved, then a true dynamic bioactive stent system would be greatly appreciated to reveal flow patterns and potential difficulties in predicting aneurysms and/or treating existing ones in animal models and ultimately human patients.

6.3   Concluding Remarks

Aneurysm formation, detection and treatment are crucial today for military personnel and the general population. If there could be a solid way to predict and prevent aneurysms before rupture, thousands of lives could be saved. The work presented in this dissertation has endeavored to establish a working aneurysm model that could aid in studying fluid flow within a bioMEMS device that could provide data meaningful to real life trauma. Within this manuscript, proof-of-concept of the Aneurysm-on-a-Chip™ has been demonstrated as a dynamic stent device in conjunction with a static bioactive design using bacterial nanocellulose. The knowledge that can be gained from further testing and model of a true prototype able to both predict aneurysm development and bioactively treat existing aneurysms, could save lives and render the "silent killer" (aneurysm rupture) impotent.

REFERENCES

REFERENCES

[1]   B. V. R. Kumar and K. B. Naidu, "Hemodynamics in Aneurysm," *Comput. Biomed. Res.*, vol. 29, no. 0011, pp. 119–139, 1996.

[2]   P. N. Watton, N. A. Hill, and M. Heil, "A mathematical model for the growth of the abdominal aortic aneurysm," *Biomech. Model. Mechanobiol.*, vol. 3, no. 2, pp. 98–113, Sep. 2004.

[3]   L. M. Reece, J. W. Khor, R. Thakur, A. Amin, S. T. Wereley, and J. F. Leary, "A Microfabricated, Microfluidics BioMEMS Device to Model Human Brain Aneurysms: The Aneurysm-on-Chip," in *Microfluidics, BioMEMS, and Medical Microsystems XIII*, San Francisco, CA, 2015.

[4]   S. Yang, "New medical technique punches holes in cells, could treat tumors," *UCBerkeley News*, p. 1, 12-Feb-2007.

[5]   J. L. Brisman, J. K. Song, and D. W. Newell, "Cerebral Aneurysms," *N Engl J Med*, vol. 355, no. 9, pp. 928–939, 2006.

[6]   D. Roy, G. Milot, and J. Raymond, "Endovascular Treatment of Unruptured Aneurysms," *Stroke*, vol. 32, no. 9, pp. 1998–2004, Sep. 2001.

[7]   S. S. Jeong, "Toxicologic evaluation of bacterial synthesized cellulose in endothelial cells and animals," *Mol. Cell. Toxicol.*, vol. 6, no. 4, pp. 373–380, 2010.

[8]   R. S. Coltran, K. Kumar, and S. Robbins, "Chapter 11: Blood Vessels - Aneurysms and Dissection," in *Pathologic Basis of Disease*, 5th ed., Philadelphi, PA: W.B. Saunders Company, 1994, pp. 499–504.

[9]   R. P. Tummala, R. M. Chu, M. T. Madison, M. Myers, D. Tubman, and E. Nussbaum, "Outcomes after Aneurysm Rupture during Endovascular Coil Embolization," *Neurosurgery*, vol. 49, pp. 1059–1067, 2001.

[10]   "What is an Aneurysm?" [Online]. Available: www.nhlbi.nih.gov/health/health-topics/topics/arm.

[11]   L. A. Weinrauch and D. Zieve, "Patient EducationWeinrauc." Harvard Medical School, 2009.

[12]   T. Krings, P. L. Lasjaunias, S. Geibprasert, V. Pereira, and F. J. Hans, "The Aneurysmal Wall. The Key to a Subclassification of Intracranial Arterial Aneurysm Vaxculopathies?," *Interv. Neuroradiol.*, vol. 14, pp. 39–47, 2008.

[13]   M. Forsting and C. Cognard, *Intracranial vascular malformations and aneurysms from diagnostic work-up to endovascular therapy*. Berlin; New York: Springer, 2004.

[14]   B. Seibert, R. P. Tummala, R. Chow, A. Faridar, S. A. Mousavi, and A. A. Divani, "Intracranial Aneurysms: Review of Current Treatment Options and Outcomes," *Front. Neurol.*, vol. 2, 2011.

[15]   "Endovascular Coiling," Johns Hopkins Medical Center, Web article, 2012.

[16]   E. S. Connolly, A. A. Rabinstein, J. R. Carhuapoma, C. P. Derdeyn, J. Dion, R. T. Higashida, B. L. Hoh, C. J. Kirkness, A. M. Naidech, C. S. Ogilvy, A. B. Patel, B. G. Thompson, P. Vespa, and on behalf of the American Heart Association Stroke Council, Council on Cardiovascular Radiology and Intervention, Council on Cardiovascular Nursing, Council on Cardiovascular Surgery and Anesthesia, and Council on Clinical Cardiology, "Guidelines for the Management of Aneurysmal Subarachnoid Hemorrhage: A Guideline for Healthcare Professionals From the American Heart Association/American Stroke Association," *Stroke*, vol. 43, no. 6, pp. 1711–1737, May 2012.

[17]   D. Wiebers, "Unruptured intracranial aneurysms: natural history, clinical outcome, and risks of surgical and endovascular treatment," *The Lancet*, vol. 362, no. 9378, pp. 103–110, Jul. 2003.

[18] E. F. M. Wijdicks, D. F. Kallmes, E. M. Manno, J. R. Fulgham, and D. G. Piepgras, "Subarachnoid Hemorrhage: Neurintensive Care and Aneurysm Repair," in *Mayo Clinic Proceedings*, 2005, vol. 80, pp. 550–559.

[19] E. F. Wijdicks, D. Hasan, K. W. Lindsay, P. J. Brouwers, R. Hatfield, G. D. Murray, J. van Gijn, and M. Vermeulen, "Short-term tranexamic acid treatment in aneurysmal subarachnoid hemorrhage," *Stroke*, vol. 20, no. 12, pp. 1674–1679, Dec. 1989.

[20] M. Vermeulen, K. W. Lindsay, G. D. Murray, F. Cheah, A. Hijdra, J. P. Muizelaar, M. Schannong, G. M. Teasdale, H. van Crevel, and J. van Gijn, "Antifibrinolytic Treatment in Subarachnoid Hemorrhage," *N Engl J Med*, vol. 311, pp. 432–437, 1984.

[21] V. L. Feigin, "Advances in Subarachnoid Hemorrhage," *Stroke*, vol. 37, no. 2, pp. 305–308, Jan. 2006.

[22] D. E. LeFeuvre and A. G. Taylor, "Endovascular cerebral aneurysm treatment: Long-term outcomes," *SAMJ*, vol. 98, no. 12, pp. 954–957, 2008.

[23] D. Fiorella, F. C. Albuquerque, and C. G. McDougall, "Durability of Aneurysm Embolization with Matrix Detachable Coils," *Neurosurgery*, vol. 58, no. 1, pp. 51–59, Jan. 2006.

[24] G. Richter, T. Engelhorn, T. Struffert, M. Doelken, O. Ganslandt, J. Hornegger, W. A. Kalender, and A. Doerfler, "Flat Panel Detector Angiographic CT for Stent-Assisted Coil Embolization of Broad-Based Cerebral Aneurysms," *Am. J. Neuroradiol.*, vol. 28, no. 10, pp. 1902–1908, Nov. 2007.

[25] J. M. Abrahams, M. S. Forman, M. S. Grady, and S. L. Diamond, "Delivery of human vascular endothelial growth factor with platinum coils enhances wall thickening and coil impregnation in a rat aneurysm model," *AJNR Am. J. Neuroradiol.*, vol. 22, no. 7, pp. 1410–1417, Aug. 2001.

[26] M. Piotin, R. Blanc, L. Spelle, C. Mounayer, R. Piantino, P. J. Schmidt, and J. Moret, "Stent-Assisted Coiling of Intracranial Aneurysms: Clinical and Angiographic Results in 216 Consecutive Aneurysms," *Stroke*, vol. 41, no. 1, pp. 110–115, Dec. 2009.

[27] Y. Murayama, Y. L. Nien, G. Duckwiler, Y. P. Gobin, R. Jahan, J. Frazee, N. Martin, and F. Viñuela, "Guglielmi Detachable Coil embolization of cerebral aneurysms: 11 years' experience," *J. Neurosurg.*, vol. 98, no. 5, pp. 959–966, May 2003.

[28] C. A. Taschner, X. Leclerc, H. Rachdi, A. M. Barros, and J.-P. Pruvo, "Matrix Detachable Coils for the Endovascular Treatment of Intracranial Aneurysms: Analysis of Early Angiographic and Clinical Outcomes," *Stroke*, vol. 36, no. 10, pp. 2176–2180, Sep. 2005.

[29] Y. Niimi, J. Song, M. Madrid, and A. Berenstein, "Endosaccular Treatment of Intracranial Aneurysms Using Matrix Coils: Early Experience and Midterm Follow-Up," *Stroke*, vol. 37, no. 4, pp. 1028–1032, Mar. 2006.

[30] Meyers, Steven R., D. J. Kenan, X. Khoo, and M. W. Grinstaff, "Bioactive Stent Surface Coating That Promotes Endothelialization while Preventing Platelet Adhesion," *Biomacromolecules*, vol. 12, pp. 533–539, 2011.

[31] C. R. Greben, D. J. Axelrod, H. Charles, E. J. Gandras, M. Bank, and A. Setton, "Treatment of Posttraumatic Aortic Pseudoaneurysms Using Detachable Hydrogel-Coated Coils," *J. Trauma Inj. Infect. Crit. Care*, vol. 66, no. 6, pp. 1735–1738, Jun. 2009.

[32] T. N. Nguyen, B. L. Hoh, S. Amin-Hanjani, J. C. Pryor, and C. S. Ogilvy, "Comparison of ruptured vs. unruptured aneurysms in recanalization after coil embolization," *Surg. Neurol.*, vol. 68, no. 1, pp. 19–23, Jul. 2007.

[33] M. H. Babiker, L. F. Gonzalez, J. Ryan, F. Albuquerque, D. Collins, A. Elvikis, and D. H. Frakes, "Influence of stent configuration on cerebral aneurysm fluid dynamics," *J. Biomech.*, vol. 45, no. 3, pp. 440–447, Feb. 2012.

[34] "Cerebral Aneurysm." Yale School of Medicne, 2012.

[35] K. K. Jain, "Surgical Treatment of Unruptured Intracranial Aneurysms," *Acta Neurochir. (Wien)*, vol. 66, pp. 187–194, 1982.

[36] A. Molyneux, "International Subarachnoid Aneurysm Trial (ISAT) of neurosurgical clipping versus endovascular coiling in 2143 patients with ruptured intracranial aneurysms: a randomised trial," *The Lancet*, vol. 360, no. 9342, pp. 1267–1274, Oct. 2002.

[37] T. W. M. Raaymakers, G. J. E. Rinkel, M. Limburg, and A. Algra, "Mortality and Morbidity of Surgery for Unruptured Intracranial Aneurysms : A Meta-Analysis," *Stroke*, vol. 29, no. 8, pp. 1531–1538, Aug. 1998.

[38] S. Fridriksson, H. Saveland, K.-E. Jakobsson, G. Edner, S. Zygmunt, L. Brandt, and J. Hillman, "Intraoperative complications in aneurysm surgery: a prospective national study," *J. Neurosurg.*, vol. 96, pp. 515–522, 2002.

[39] F. Jung, C. Wischke, and A. Lendlein, "Degradable, Multifunctional Cardiovascular Implants: Challenges and Hurdles," Bulletin 35, 2010.

[40] P. M. Consigny, D. A. Silverberg, and N. J. Vitali, "Use of Endothelial Cells Containing Superparamagnetic Microspheres to Improve Endothelial Cell Delivery to Arterial Surfaces after Angioplasty," *J. Vasc. Interv. Radiol.*, vol. 10, no. 2, pp. 155–163, Feb. 1999.

[41] Alimi, Yves S., "Looking to the Future - Next-generation Bioactive Stent-graft Technology," *Touch Brief.*, pp. 65–68, 2008.

[42] P. C. Slaikeu, M. P. Wallace, J. C. Eder, J. J. Barry, and R. M. Abrams, "Bioactive Aneurysm Closure Device Assembly and Kit," US 2001/0047202 A1.

[43] I. Lim, "Biocompatibility of Stent Materials," *MURJ*, vol. 11, pp. 33–37, 2004.

[44] L. Moroni, P. Habibovic, D. J. Mooney, and C. A. van Blitterswijk, "Functional Tissue Engineering Through Biofunctional Macromolecules and Surface Design," Bulletin 35, 2010.

[45] C. Roberts, C. S. Chen, M. Mrksich, V. Martichonok, D. E. Ingber, and G. M. Whitesides, "Using Mixed Self-Assembled Monolayers Presenting RGD and (EG)3OH Groups to Characterize Long-Term Attachment of Bovine Capillary Endothelial Cells to Surfaces," *J Am Chem Soc*, vol. 120, pp. 6548–6555, Jun. 1998.

[46] M. J. P. Biggs, R. G. Richards, and M. J. Dalby, "Nanotopographical modification: a regulator of cellular function through focal adhesions," *Nanomedicine Nanotechnol. Biol. Med.*, vol. 6, no. 5, pp. 619–633, Oct. 2010.

[47] M. O. Klein, A. Bijelic, T. Ziebart, F. Koch, P. W. Kämmerer, M. Wieland, M. A. Konerding, and B. Al-Nawas, "Submicron Scale-Structured Hydrophilic Titanium Surfaces Promote Early Osteogenic Gene Response for Cell Adhesion and Cell Differentiation," *Clin. Implant Dent. Relat. Res.*, p. no–no, May 2011.

[48] E. W. K. Young, A. R. Wheeler, and C. A. Simmons, "Matrix-dependent adhesion of vascular and valvular endothelial cells in microfluidic channels," *Lab. Chip*, vol. 7, no. 12, p. 1759, 2007.

[49] J. El-Ali, P. K. Sorger, and K. F. Jensen, "Cells on chips," *Nature*, vol. 442, no. 7101, pp. 403–411, Jul. 2006.

[50] A. S. Arbab, V. Frenkel, S. D. Pandit, S. A. Anderson, G. T. Yocum, M. Bur, H. M. Khuu, E. J. Read, and J. A. Frank, "Magnetic Resonance Imaging and Confocal Microscopy Studies of Magnetically Labeled Endothelial Progenitor Cells Trafficking to Sites of Tumor Angiogenesis," *Stem Cells*, vol. 24, no. 3, pp. 671–678, Mar. 2006.

[51] A. Folch and M. Toner, "Microengineering of Cellular Interactions," *Annu Rev Biomed Eng*, vol. 02, pp. 227–256, 2000.

[52] I. Meyvantsson and D. J. Beebe, "Cell Culture Models in Microfluidic Systems," *Annu. Rev. Anal. Chem.*, vol. 1, no. 1, pp. 423–449, Jul. 2008.

[53] S. D. H. Chan, G. Luedke, M. Valer, C. Buhlmann, and T. Preckel, "Cytometric analysis of protein expression and apoptosis in human primary cells with a novel microfluidic chip-based system," *Cytometry*, vol. 55A, no. 2, pp. 119–125, Oct. 2003.

[54] H. J. Kim, D. Huh, G. Hamilton, and D. E. Ingber, "Human gut-on-a-chip inhabited by microbial flora that experiences intestinal peristalsis-like motions and flow," *Lab. Chip*, vol. 12, pp. 2165–2174, 2012.

[55] S. Haeberle and R. Zengerle, "Microfluidic platforms for lab-on-a-chip applications," *Lab. Chip*, vol. 7, no. 9, p. 1094, 2007.

[56] M. M. G. Grafton, L. Wang, P.-A. Vidi, J. Leary, and S. A. Lelievre, "Breast-on-a-chip: mimicry of the channeling system of the breast for development of theranostics," *Integr. Biol.*, vol. 3, pp. 451–459, 2010.

[57] D. Huh, Y. Torisawa, G. A. Hamilton, H. J. Kim, and D. E. Ingber, "Microengineered physiological biomimicry: Organs-on-Chips," *Lab. Chip*, vol. 12, pp. 2156–2164, 2012.

[58] C. J. Kirkpatrick, F. Bittinger, M. Wagner, H. Kohler, T. G. van Kooten, C. L. Klein, and M. Otto, "Current trends in biocompatibility testing," *Proc. Inst. Mech. Eng. [H]*, vol. 212, no. 2, pp. 75–84, Feb. 1998.

[59] L. Kim, Y.-C. Toh, J. Voldman, and H. Yu, "A practical guide to microfluidic perfusion culture of adherent mammalian cells," *Lab. Chip*, vol. 7, no. 6, p. 681, 2007.

[60] B. D. Ratner, "A History of Biomaterials." Elsevier, Inc, 2004.

[61] B. D. Ratner, A. S. Hoffman, F. J. Schoen, and J. Lemons, "Biomaterials Science: A Multidisciplinary Endeavor." Elsevier, Inc, 2004.

[62] D. F. Williams, "Definitions in Biomaterials.," presented at the Consensus Conference of the European Society for Biomaterials, Chester, England, 1986, vol. 4.

[63] L. L. Hench, "Third-Generation Biomedical Materials," *Science*, vol. 295, no. 5557, pp. 1014–1017, Feb. 2002.

[64] S. I. Stupp and P. V. Braun, "Molecular Manipulation of Microstructures: Biomaterials, Ceramics, and Semiconductors," *Science*, vol. 277, pp. 1242–1248, 1997.

[65] Y. Wang, G. A. Ameer, B. J. Sheppard, and R. Langer, "A tough biodegradable elastomer," *Nat. Biotechnol.*, vol. 20, pp. 602–606, 2002.

[66] D. Campoccia, P. Doherty, M. Radice, P. Brun, G. Abatangelo, and D. F. Williams, "Semisynthetic resorbable materials from hyaluronan esterification," *Biomaterials*, vol. 19, no. 23, pp. 2101–2127, 1998.

[67] A. S. Hoffman, "Hydrogels for biomedical applications," *Adv. Drug Deliv. Rev.*, vol. 43, pp. 3–12, 2002.

[68] G. D. Prestwich, D. M. Maracak, J. F. Marecek, K. P. Vercruysse, and M. Ziebell, "Controlled chemcial modification of hyaluronic acid: synthesis, applications, and biodegradation of hydrazide derivatives," *J. Controlled Release*, vol. 53, no. 1–3, pp. 93–103, 1998.

[69] K. A. Kazmierska and T. Ciach, "Bioactive Coatings for Minimally Invasive Medical Devices: Surface Modification in the Service of Medicine," *Recent Pat. Biomed. Eng.*, vol. 2, pp. 1–14, 2009.

[70] B. G. Amsden, "Biodegradable elastomers in drug delivery," *Expert Opin. Drug Deliv.*, vol. 5, no. 2, pp. 175–187, Feb. 2008.

[71] J. C. Rodriguez-Cabello, S. Prieto, J. Reguera, F. J. Arias, and A. Ribeiro, "Biofunctional design of elastin-like polymers for advanced applications in nanobiotechnology," *J Biomater Sci Polym. Edn*, vol. 18, no. 3, pp. 269–286, 2007.

[72] C. Fidkowski, M. R. Kaazempur-Mofrad, J. Borenstein, J. P. Vacanti, R. Langer, and Y. Wang, "Endothelialized Microvasculature Based on a Biodegradable Elastomer," *Tissue Eng.*, vol. 11, no. 1/2, pp. 302–309, 2005.

[73] A. A. Al Fattah Amara, "Polyhydroxyalkanoates: From Basic Research and Molecular Biology to Application," *IUM Eng. J.*, vol. 9, pp. 37–73, 2008.

[74] K.-C. Chen, T.-P. Lee, Y.-C. Pan, C.-L. Chiang, C.-L. Chen, Y.-H. Yang, B.-L. Chiang, H. Lee, and A. M. Wo, "Detection of Circulating Endothelial Cells via a Microfluidic Disk," *Clin. Chem.*, vol. 57, no. 4, pp. 586–592, Feb. 2011.

[75] X. Yang, K. Zhao, and G.-Q. Chen, "Effect of surface treatment on the biocompatibility of microbial polyhydroxyalkanoates," *Biomaterials*, vol. 23, pp. 1391–1397, 2002.

[76] S.-J. Kim, J. K. Lee, J. W. Kim, J.-W. Jung, K. Seo, S.-B. Park, K.-H. Roh, S.-R. Lee, Y. H. Hong, S. J. Kim, Y.-S. Lee, S. J. Kim, and K.-S. Kang, "Surface modification of polydimethylsiloxane (PDMS) induced proliferation and neural-like cells differentiation of umbilical cord blood-derived mesenchymal stem cells," *J. Mater. Sci. Mater. Med.*, vol. 19, no. 8, pp. 2953–2962, Mar. 2008.

[77] D. Fuard, T. Tzvetkova-Chevolleau, S. Decossas, P. Tracqui, and P. Schiavone, "Optimization of poly-di-methyl-siloxane (PDMS) substrates for studying cellular adhesion and motility," *Microelectron. Eng.*, vol. 85, no. 5–6, pp. 1289–1293, May 2008.

[78] M. Ni, W. H. Tong, D. Choudhury, N. A. A. Rahim, C. Iliescu, and H. Yu, "Cell Culture on MEMS Platforms: A Review," *Int. J. Mol. Sci.*, vol. 10, no. 12, pp. 5411–5441, Dec. 2009.

[79] C. S. Chen, M. Mrksich, S. Huang, G. M. Whitesides, and D. E. Ingber, "Micropatterned Surfaces for Control of Cell Shape, Position, and Function," *Biotechnol. Prog.*, vol. 14, pp. 356–363, May 1998.

[80] D. Klemm, D. Schumann, U. Udhardt, and S. Marsch, "Bacterial synthesized cellulose - artificial blood vessels for microsurgery," *Prog Polym Sci*, vol. 26, pp. 1561–1603, 2001.

[81] D. Klemm, U. Udhardt, S. Marsch, and D. Schumann, "Method and Device for Producing Shaped Microbial Cellulose for use as a Biomaterial, Especially for Microsurgery," US 2003/0013163 A1.

[82] A. Retegi, N. Gabilondo, C. Peña, R. Zuluaga, C. Castro, P. Gañan, K. la Caba, and I. Mondragon, "Bacterial cellulose films with controlled microstructure–mechanical property relationships," *Cellulose*, vol. 17, no. 3, pp. 661–669, Dec. 2009.

[83] W. K. Czaja, D. J. Young, M. Kawecki, and R. M. Brown, Jr., "The Future Prospects of Microbial Cellulose in Biomedical Applications," *Biomacromolecules*, vol. 8, no. 1, pp. 1–12, Jan. 2007.

[84] H. Andersson and A. van den Berg, "Microfabrication and microfluidics for tissue engineering: state of the art and future opportunities," *Lab. Chip*, vol. 4, no. 2, p. 98, 2004.

[85] K. S. Rho, L. Jeong, G. Lee, B.-M. Seo, Y. J. Park, S.-D. Hong, S. Roh, J. J. Cho, W. H. Park, and B.-M. Min, "Electrospinning of collagen nanofibers: Effects on the behavior of normal human keratinocytes and early-stage wound healing," *Biomaterials*, vol. 27, no. 8, pp. 1452–1461, Mar. 2006.

[86] H. Fink, L. Ahrenstedt, A. Bodin, H. Brumer, P. Gatenholm, A. Krettek, and B. Risberg, "Bacterial cellulose modified with xyloglucan bearing the adhesion peptide RGD promotes endothelial cell adhesion and metabolism - a promising modification for vascular grafts," *J. Tissue Eng. Regen. Med.*, vol. 5, pp. 454–463, Dec. 2010.

[87] D. I. Zeugolis, B. Li, R. R. Lareu, C. K. Chan, and M. Raghunath, "Collagen solubility testing, a quality assurance step for reproducible electro-spun nano-fibre fabrication. A technical note," *J. Biomater. Sci. Polym. Ed.*, vol. 19, no. 10, pp. 1307–1317, Jan. 2008.

[88] S. Vitta and V. Thiruvengadam, "Multifunctional bacterial cellulose and nanoparticle-embedded composites," *Curr. Sci.*, vol. 102, no. 10, pp. 1–8, May 2012.

[89] R. T. Olsson, M. A. S. Azizi Samir, G. Salazar-Alvarez, L. Belova, V. Ström, L. A. Berglund, O. Ikkala, J. Nogués, and U. W. Gedde, "Making flexible magnetic aerogels and stiff magnetic nanopaper using cellulose nanofibrils as templates," *Nat. Nanotechnol.*, vol. 5, no. 8, pp. 584–588, Aug. 2010.

[90] H. Backdahl, G. Helenius, A. Bodin, U. Nannmark, B. R. Johansson, B. Risberg, and P. Gatenholm, "Mechanical properties of bacterial cellulose and interactions with smooth muscle cells," *Biomaterials*, vol. 27, pp. 2141–2149, 2006.

[91] N. L'Heureux, S. Paquet, R. Labbe, L. Germain, and F. A. Auger, "A completely biological tissue-engineered human blood vessel," *FASEB*, vol. 12, no. 1, pp. 47–56, Jan. 1998.

[92] L. E. Niklason, J. Gao, W. M. Abbott, K. K. Hirschi, S. Houser, and R. Marini, "Functional arteries grown in vitro," *Science*, vol. 284, no. 5413, pp. 489–493, 1999.

[93] R. Strehl, K. Schumacher, U. de Vries, and W. W. Minuth, "Proliferating cells versus differentiated cells in tissue engineering," *Tissue Eng.*, vol. 8, no. 1, pp. 37–42, 2002.

[94] G. M. Lanza, X. Yu, P. M. Winter, D. R. Abendschein, K. K. Karukstis, M. J. Scott, L. K. Chinen, R. W. Fuhrhop, D. E. Scherrer, and S. A. Wickline, "Targeted Antiproliferative Drug Delivery to Vascular Smooth Muscle Cells with a Magnetic Resonance Imaging Nanoparticle Contrast Agent," *Circulation*, pp. 2842–2847, Nov. 2002.

[95] N. Kramer, A. Walzl, C. Unger, M. Rosner, G. Krupitza, M. Hengstschläger, and H. Dolznig, "In vitro cell migration and invasion assays," *Mutat. Res. Mutat. Res.*, vol. 752, no. 1, pp. 10–24, Jan. 2013.

[96] A. D. van der Meer, K. Vermeul, A. A. Poot, J. Feijen, and I. Vermes, "A microfluidic wound-healing assay for quantifying endothelial cell migration," *AJP Heart Circ. Physiol.*, vol. 298, no. 2, pp. H719–H725, Nov. 2009.

[97] A. E. Adams and J. R. Pringle, "Staining of actin with fluorochrome-conjugated phalloidin," *Methods Enzymol.*, vol. 194, pp. 729–731, 1991.

[98] H. Faulstich, S. Zobeley, G. Rinnerthaler, and J. V. Small, "Fluorescent phallotoxins as probes for filamentous actin," *J Muscle Res Cell Motil*, vol. 9, no. 5, pp. 370–383, 1988.

[99] W. Jeong and K. Rhee, "Hemodynamics of Cerebral Aneurysms: Computational Analyses of Aneurysm Progress and Treatment," *Comput. Math. Methods Med.*, vol. 2012, pp. 1–11, 2012.

[100] J. R. Cebral, F. Mut, J. Weir, and C. Putman, "Quantitative Characterization of the Hemodynamic Environment in Ruptured and Unruptured Brain Aneurysms," *Am. J. Neuroradiol.*, Dec. 2010.

[101] S. M. C. Berman, P. Walczak, and J. W. M. Bulte, "Tracking stem cells using magnetic nanoparticles," *Wiley Interdiscip. Rev. Nanomed. Nanobiotechnol.*, vol. 3, no. 4, pp. 343–355, Jul. 2011.

[102] J.-L. Yu, S. Yang, Q. Luo, H.-L. Wang, B. Wang, Y.-Y. Qu, and K. Xu, "Endovascular Treatment of Intracranial Ruptured Aneurysms Associated with Arteriovenous Malformations: A Clinical Analysis of 14 Hemorrhagic Cases," *Interv. Neuroradiol.*, vol. 17, pp. 78–86, 2011.

[103] S. Boutry, D. Forge, C. Burtea, I. Mahieu, O. Murariu, S. Laurent, L. Vander Elst, and R. N. Muller, "How to quantify iron in an aqueous or biological matrix: a technical note," *Contrast Media Mol. Imaging*, vol. 4, no. 6, pp. 299–304, Nov. 2009.

[104] W. Strober, "Trypan Blue Exclusion Test of Cell Viability," in *Current Protocols in Immunology*, J. E. Coligan, B. E. Bierer, D. H. Margulies, E. M. Shevach, and W. Strober, Eds. Hoboken, NJ, USA: John Wiley & Sons, Inc., 2001.

[105] A. Petri-Fink, M. Chastellain, L. Juillerat-Jeanneret, A. Ferrari, and H. Hofmann, "Development of functionalized superparamagnetic iron oxide nanoparticles for interaction with human cancer cells," *Biomaterials*, vol. 26, no. 15, pp. 2685–2694, May 2005.

[106] E. P. McFadden, E. Stabile, E. Regar, E. Cheneau, A. T. Ong, T. Kinnaird, W. O. Suddath, N. J. Weissman, R. Torguson, K. M. Kent, A. D. Pichard, L. F. Satler, R. Waksman, and P. W. Serruys, "Late thrombosis in drug-eluting coronary stents after discontinuation of antiplatelet therapy," *The Lancet*, vol. 364, no. 9444, pp. 1519–1521, Oct. 2004.

[107] "CometScore Tutorial." TriTek Corp., 2013.

[108] F. Nossoni, "Single-Cell Gel Electrophoresis (Comet Assay): Methodology, Potential Applications, and Limitations in Cancer Research," *Microbiol. Mol. Genet. Basic Biotechnol. EJournal*, vol. 4, pp. 30–35.

[109] A. K. Gupta and M. Gupta, "Synthesis and surface engineering of iron oxide nanoparticles for biomedical applications," *Biomaterials*, vol. 26, no. 18, pp. 3995–4021, Jun. 2005.

[110] T. D. Schladt, K. Schneider, H. Schild, and W. Tremel, "Synthesis and bio-functionalization of magnetic nanoparticles for medical diagnosis and treatment," *Dalton Trans.*, vol. 40, no. 24, p. 6315, 2011.

[111] B. Issa, I. Obaidat, B. Albiss, and Y. Haik, "Magnetic Nanoparticles: Surface Effects and Properties Related to Biomedicine Applications," *Int. J. Mol. Sci.*, vol. 14, no. 11, pp. 21266–21305, Oct. 2013.

[112] Y. Farhatnia, A. Tan, A. Motiwala, B. G. Cousins, and A. M. Seifalian, "Evolution of covered stents in the contemporary era: clinical application, materials and manufacturing strategies using nanotechnology," *Biotechnol. Adv.*, vol. 31, no. 5, pp. 524–542, Sep. 2013.

[113] L. E. Freed, J. C. Marquis, A. Nohria, J. Emmanual, A. G. Mikos, and R. Langer, "Neocartilage formation in vitro and in vivo using cells culturing on synthetic biodegradable polymers," vol. 27, pp. 11–23, 1993.

[114] K. Matsumoto, K. -i. Hirano, S. Nozaki, A. Takamoto, M. Nishida, Y. Nakagawa-Toyama, M. Y. Janabi, T. Ohya, S. Yamashita, and Y. Matsuzawa, "Expression of Macrophage (M) Scavenger Receptor, CD36, in Cultured Human Aortic Smooth Muscle Cells in Association With Expression of Peroxisome Proliferator Activated Receptor- , Which Regulates Gain of M -Like Phenotype In Vitro, and Its Implication in Atherogenesis," *Arterioscler. Thromb. Vasc. Biol.*, vol. 20, no. 4, pp. 1027–1032, Apr. 2000.

[115] "CometAssay Alkaline Control Cells." Trevigen, 2014.

[116] V. Kundumani-Sridharan, N. K. Singh, S. Kumar, R. Gadepalli, and G. N. Rao, "Nuclear Factor of Activated T Cells c1 Mediates p21-activated Kinase 1 Activation in the Modulation of Chemokine-induced Human Aortic Smooth Muscle Cell F-actin Stress Fiber Formation, Migration, and Proliferation and Injury-induced Vascular Wall Remodeling," *J. Biol. Chem.*, vol. 288, no. 30, pp. 22150–22162, Jul. 2013.

[117] M. Raffel, Ed., *Particle image velocimetry: a practical guide*, 2nd ed. Heidelberg ; New York: Springer, 2007.

[118] I. Foster and C. Kesselman, "The Emerging Grid," in *Computational Aerosciences in the 21st Century*, M. D. Salas and W. K. Anderson, Eds. Dordrecht: Springer Netherlands, 2000, pp. 29–46.

[119] H. Yan and J. G. Liu, "Robust Phase Correlation based Motion Estimation and Its Applications," in *Proceedings of the British Machine Vision Conference 2008*, Leeds, UK, 2008.

[120] "Qi-Quantitative Imaging (PIV and more)." SourceForge, 2014.

[121] A. Eckstein and P. P. Vlachos, "Digital particle image velocimetry (DPIV) robust phase correlation," *Meas. Sci. Technol.*, vol. 20, no. 5, p. 055401, May 2009.

[122] A. C. Eckstein, J. Charonko, and P. Vlachos, "Phase correlation processing for DPIV measurements," *Exp. Fluids*, vol. 45, no. 3, pp. 485–500, Sep. 2008.

[123] M. A. Castro, C. M. Putman, and J. R. Cebral, "Computational Fluid Dynamics Modeling of Intracranial Aneurysms: Effects of Parent Artery Segmentation on Intra-Aneurysmal Hemodynamics," *Am J Neuroradiol*, vol. 27, pp. 1703–1709, Sep. 2006.

VITA

VITA

Lisa M. Reece
Department of Basic Medical Sciences, Purdue University

Education

B.S., Microbiology, 1983, University of Texas at El Paso, El Paso, Texas
Ph.D., Basic Medical Sciences, 2014, Purdue University, West Lafayette, Indiana

Research & Scientific Interests

My research interests revolve around BioMEMS work in treating disease as well as nanomedicine (specifically targeting nanoparticles) for cancer therapy. I am also very interested in STEM education and problem-based learning and have experience in developing PBL units for area high schools. I have a broad background in microbiology and immunology, with specific training and expertise in key research areas such as single cell sorting (flow cytometry as well as micromanipulation/microinjection), advanced data analysis with several commercial software packages, and experience with prototyping of new cell analysis/sorting hardware and software. I am considered an expert in the field of flow cytometry and was on the committee that generated the On the clinical side, I have participated in Phase II and Phase II clinical trials for the nasal spray, Flonase, where I ran the clinical experiments on human volunteers. I have a demonstrated record of successful and productive basic and clinical research projects. I excel in laboratory setup and management and currently supervise 9 bionanotechnology labs within the Birck Nanotechnology Center at Purdue University.

Professional Experience

Current Positions at Purdue University

2009-2014	Lab Director, Indiana Clinical Translational Sciences Institute (IN-CTSI) Bionanotechnology Core Facilities, Birck Nanotechnology Center (BNC)
2009	Interim Manager, Purdue Cancer Center Flow Cytometry and Cell Separation Facility, Bindley Bioscience Center (BBC)

2008-2014	Coordinator, IN-CTSI Bionanotechnology Approaches and Therapeutics Development, BNC	
2006-2014	Biosafety Research Engineer, BNC	
2005-2007	Lab Director, Molecular Cytometry Facility, BBC	

Past Positions

1981-1982	Phlebotomist, Clinical Laboratory	*Providence Memorial Hospital, El Paso, TX*
1983-1984	Microbiology Laboratory Technician, Dept. of Quality Assurance	*American Convertors, Inc., El Paso, Texas*
1984-1985	Assistant Microbiology Technician, Dept. of Quality Control	*Baltimore Spice Company, Inc., El Paso, Texas*
1986-1987	Assistant Microbiologist, Dept. of Quality Control	*Seamless Hospital Products, Inc., El Paso, Texas*
1987	Volunteer Laboratory Assistant, Dept. of Clinical Investigations	*William Beaumont Army Medical Center, Ft. Bliss, Texas*
1987-1989	Laboratory Supervisor, Dept. of Biological Sciences	*Univ. of Texas at El Paso*
1989	Research Assistant II, Dept. of Tumor Biology	*Univ. of Texas M.D. Anderson Cancer Center, Houston*
1989-1993	Research Assistant I, Dept. of Chemical Pathology	*UTMB*
1993-1996	Research Assistant II, Div. of Adult Allergy and Immunology, Dept. of Internal Medicine	*UTMB*
1996-2003	Research Associate I, Molecular Cytometry Unit, Dept. of Internal Medicine	*UTMB*
2003-2005	Assistant Director, Molecular Cytometry Unit, Dept. of Internal Medicine	*Univ. of Texas Medical Branch, Galveston (UTMB)*

Other Experience and Professional Memberships

1996-2014	Member	International Society for the Advancement of Cytometry (ISAC)

2006-2014	Member, Oncological Sciences Center	Purdue Univ.
2006-2007	Member, Policy and Procedures Committee, BNC	Purdue Univ.
2006-2010	Co-Chair, International Groups Subcommittee, Membership Services Committee - Invited	ISAC
2010-2014™	Member, Discovery Park Graduate Student Ambassadors	Purdue Univ.
2011	Item Writer/Expert for the International Cytometry Certification Examination (ICCE) - Invited	ISAC
2011	Chairperson, Malvern Instruments-Birck Nanotechnology Center Joint Mini-Symposium	Purdue Univ.
2014	Nominated for two-year membership in AAAS/Science Program for Excellence in Science - Accepted	American Association for the Advancement of Science (AAAS)

Honors

1995	Who's Who in America
1995	Who's Who of American Women
1995	Who's Who in Science and Engineering
2010	Purdue Graduate Ambassador Award - $500 (competitive)
2010	ISAC Student Travel Award - $650 (competitive)
2010	ISAC Outstanding Poster Award - $200 (competitive)
2011	Purdue Graduate Ambassador Award - $500 (competitive)
2011	Purdue University Seeds for Success Investigator Award
2012	Purdue University Student Innovator Award
2012	Purdue Graduate Ambassador Award - $500 (competitive)
2013	Purdue Graduate Ambassador Award - $500 (competitive)
2014	Purdue 3MT Thesis Competition – finalist (competitive)
2014	Purdue University Student Innovator Award
2014	Purdue Graduate Ambassador Award - $600 (competitive)

Past Grant Support

Department of Defense DMRDP-ARATDA, DM090909: PI - Jean Paul Allain, PhD, **Co-PI - Lisa M. Reece,** "Development and Fabrication of a Stent Prototype to Induce Closure of Post-Traumatic Blast-Induced Pseudoaneurysm"	01/01/2011-01/31/2014 $1,000,000	0.25 AY

The goal of this grant is to enhance attraction and adhesion locally at a bioactive stent surface and improve/promote tissue growth and biocompatability with magnetic protocol.

Teaching Responsibilities

Birck Nanotechnology Center, Purdue University
2011-Present (every Spring/Summer Semesters)   **Instructor, BNC Tissue Culture Workshop**

2014-Summer   **Instructor, Research Goes to School**

Thesis

Reece, Lisa M. "Development of a Bioactive Stent Prototype and Aneurysm-on-a-Chip™ Model for the Treatment of Aneurysms". Ph.D. thesis, Department of Basic Medical Sciences, College of Veterinary Medicine, Purdue University, 2014.

Books/Book Chapters

1. Boysen, Earl, Muir, Nancy D., "Nanotechnology for Dummies", 2nd Edition, **Reece, Lisa M.**, Technical Editor. Wiley Press, ISBN: 978-0-470-89191-9, Aug. 2011.
2. Ignacio C. Camarillo, Funian Xiao, S. Madhivanan, Therese Salameh, Maxine Nichols, **Lisa M. Reece**, James F. Leary, Kevin Otto, Arutselvan Natarajan, A. Ramesh, Raji Sundararajan. "Electroporation-based Therapies for Cancer: From Basics to Clinical Applications - Chapter 4: Low and high voltage electrochemotherapy for breast cancer: an *in vitro* model study", Biohealthcare Publishing Series on Pharma, Biotech and Bioscience: Science, Technology and Business; hardback; Ed. Raji Sundararajan, in press, 2013.
3. Raji Sundarajan, Arutselvan Natarajan, Kavitha Sankaranarayanan, **Lisa M. Reece**, Brent Vernon. "Electroporation-based Therapies for Cancer: From Basics to Clinical Applications - Chapter 9: Low and high voltage electroporation of *in vitro* ovarian adenocarcinoma cells", Biohealthcare Publishing Series on Pharma, Biotech and Bioscience: Science, Technology and Business; hardback; Ed. Raji Sundararajan, in press, 2013.
4. **Lisa M. Reece**, Kavitha Sankarananarayanan, Priyadarshan Kathirvelu, Christy Cooper, Raji Sundararajan, James F. Leary. "Electroporation-based Therapies for Cancer: From Basics to Clinical Applications - Chapter 11: Targeted delivery of siRNA and other difficult to transfect molecules using electroporation: current status and future scope", Biohealthcare Publishing Series on Pharma, Biotech and Bioscience: Science, Technology and Business; hardback; Ed. Raji Sundararajan, in press, 2013.

Patents and Inventions

1. **Reece, Lisa M.**, Thakur, Raviraj, Alucozai, Milad, Leary, James F. "Aneurysm-on-a-Chip™ Microfluidics Device". Purdue Office of Technology Commercialization Disclosure: 2013-REEC-66567 (2013).
2. Allain, Jean Paul, **Reece, Lisa**, Yang, Zhangcan, Armonda, Rocco, Kempaiah, Ravindra, Tigno, Teodoro. "System and stent for repairing endovascular defects and methods of use". European Patent US2012059151 (2014).
3. Allain, Jean Paul, **Reece, Lisa**, Yang, Zhangcan, Armonda, Rocco, Kempaiah, Ravindra, Tigno, Teodoro. "System and stent for repairing endovascular defects and methods of use". U.S. Patent 2014/0277354 A1 (2014).

Talks and Presentations at National and International Meetings

1. **Reece, Lisa**, Fontenot, Andrea, Leary, James F. "High-Throughput Instrumentation for Flow Cytometry and Cell Sorting". 20th Annual Houston Conference on Biomedical Engineering Research, Houston, Texas, 2003.
2. **Reece, Lisa**, Leary, James F. "High-Throughput Instrumentation for Sorting Stem Cells and Some Ethics Behind the Research". Phi Theta Kappa Dimensions and Directions Discussion, Galveston Community College, Galveston, Texas, 2004.
3. **Reece, Lisa M**. "Cellular Studies in the Development of a Bioactive Stent Prototype to Close Aneurysm/Pseudoaneurysm Neck Orifices". 10th Annual World Congress of SBMT on Brain, Spinal Cord Mapping, and Image Guided Therapy, Baltimore, MD, 2013.

Participation in K-12 Events

1. 2010-Present: Member – Organization Committee, NISE NanoDays hosted at Birck Nanotechnology Center
2. 2013-2014: Educational Liaison – Research Goes to School program, NSF I-Cubed funded grant – Discovery Learning Center and Birck Nanotechnology Center

PUBLICATIONS

Article in Preparation – Pertinent to Thesis Work (Purdue University)

Reece, Lisa M., Leary, James F. "A Microfabricated, Microfluidic BioMEMS Device to Model Human Brain Aneurysms: The Aneurysm-on-a-Chip™". SPIE Photonics West BIOS: Conference on Microfluidics, BioMEMS, and Medical Microsystems XIII, Tracking #PW15B-BO208-3, 2014.

Other Article in Preparation (Purdue University)

Madsen, Alex, Weaver, Gabriela, Kirkham, Lisa, **Reece, Lisa M.**, Adedokun, Omolola. "Research Goes to School: Development of Nanoscience-Specific Learning Objectives and Assessment for a Professional Development Program". Journal of Nano Education, 2014.

Article Submitted – Pertinent to Thesis Work (Purdue Univeristy)

Pavón, Juan José, Allain, Jean Paul, Tomar, Vikas, Devendra, Verma, **Reece, Lisa M.**, Cooper, Christy L., Rendón, Mónica Echeverry. "In-situ studies of bio-nanomechanical behavior in a multi-functional hierarchical magnetic bacterial nano-cellulose (MBNC) hydrogel." Proceedings of National Academy of Science, PNAS, submitted 2014.

Published Articles – Pertinent to Thesis Work (Purdue University)

1. Leary, James F., Key, Jaehong, Vidi, Pierre-Alexandre, Cooper, Christy L., Kole, Ayeeshik, **Reece, Lisa M.**, Leliévre, Sophie A. "Human organ-on-a-chip BioMEMS devices for testing new diagnostic and therapeutic strategies". SPIE 86150A-1:1-10 (2013).
2. Sundararajan, Raji, Xiao, Funian, Salameh, Therese, **Reece, Lisa M.**, Campana, Luca, Camarillo, Ignacio G. "Effective Proliferation Control of Human Cancer Cells using Electrical Pulses". IEEE Transactions on Dielectrics and Electrical Insulation (2012).
3. Grafton, Meggie M.G., Maleki, Teimour, Zordan, Michael D., **Reece, Lisa M.**, Byrnes, Ron, Jones, Alan, Todd, Paul, Leary, James F. "Microfluidic MEMS Hand-Held Flow Cytometer". Microfluidics, BioMEMS, and Medical Microsystems IX, SPIE 7929: 79290C-1-79290C-10, 2011.
4. Grafton, M.G., Maleki, T., Zordan, M.D., **Reece, L.M.**, Jones, A.L., Todd, P.W., Leary, J.F. "Design of a portable point-of-care BioMEMS microfluidic blood analyzer". Proc. SPIE 2011.
5. Xiao, Funian, Leary, Jim F., **Reece, Lisa**, Camarillo, Ignacio G., Sundararajan, Madhivanan, Sundararajan, Raji. "Nanosecond, Low Voltage Electro-Endocrine-Therapy for Breast Cancer Treatment". Annual Report Conference on Electrical Insulation and Dielectric Phenomena, IEEE Xplore: 1-4, 2010.
6. Grafton, Meggie M., Zordan, Michael D., Chuang, Han-Sheng, Rajdev, Pooja, **Reece, Lisa M.**, Irazoqui, Pedro P., Wereley, Steven T., Byrnes, Ron, Todd, Paul, Leary, James F. "Portable microfluidic cytometer for whole blood cell analysis." Microfluidics, BioMEMS, and Medical Microsystems VIII, SPIE 7593: 75930M-1-75930M-8, 2010.
7. **Reece, L.M.**, Sanders, L., Kennedy, D., Guernsey, B., Todd, P., Leary, J.F. "High-Throughput Magnetic Flow Sorting of Human Cells Selected on the Basis of Magnetophoretic Mobility" SPIE, 7568-73, 2010.

8. Geheb, B, Grafton, M.G., Jang, J., **Reece, L.M.**, Kwon, J., Leary, J.F., Jung, B. "Low-Noise, Wide Dynamic Range Sigma Delta Sensor Interface with Applications in Microfluidic Cell Sorting." IEEE Transaction on Biomedical Circuits and Systems, Vol. 3, No. 3, April 2009.

9. Xiao, Funian, Salameh, Therese, Camarillo, Ignacio, Dykstra, Carly, Lenarduzzi, Nick, **Reece, Lisa**, Leary, Jim F. Electrically-Enhanced Chemodrug Delivery to Human Breast Cancer Cells". Biomedical Conference Presentation, IEEE: 1-7, 2009.

10. Zordan, Michael D., Grafton, Meggie M.G., Acharya, Ghanashyam, **Reece, Lisa M.**, Aronson, Arthur I., Park, Kinam, Leary, James F. "A microfluidic-based hybrid SPR/molecular imaging biosensor for the multiplexed detection of food-borne pathogens". Frontiers in Pathogen Detection: From Nanosensors to Systems, SPIE 7167: 716706-1-716706-10, 2009.

11. Grafton, M.G., Geheb, B., Jang, J.H., Chuang, H.-S., Rajdev, P., **Reece, L.M.**, Irazoqui, P.P., Wereley, S.T., Jung, B., Leary, J.F. "Microfabrication of a Two-Stage BioMEMS Microfluidics Cell Sorter." Microfluidics, BioMEMS, and Medical Microsystems VII, Proc. of SPIE, Vol. 7207, 7207A-1, 2009.

12. Zordan, M.D., Grafton, M.G., Ghanashyam, A., **Reece, L.M.**, Cooper, C.L., Aronson, A.I., Park, K., Leary, J.F. "Detection of Pathogenic *E. coli* O157:H7 by a Hybrid Microfluidic SPR and Molecular Imaging Device." Cytometry: Part A, Nov. 5, 2008.

13. Grafton, M., **Reece, L.M.**, Irazoqui, P.P., Jung, B., Summers, H.D., Bashir, R., Leary, J.F. "Design of a Multi-Stage Microfluidics System for High-Speed Flow Cytometry and Closed System Cell Sorting for Cytomics." Imaging, Manipulation, and Analysis of Biomolecules, Cells, and Tissues VI, SPIE, 6859, 2008.

14. Seale-Goldsmith, Mary-Margaret, Haglund, Emily, Cooper, Christy L., **Reece, Lisa M.**, Knapp, Deborah W., Leary, James F. "Multi-Component, Multi-Functional Nanomedical Systems for Drug/Gene Delivery". 2nd Annual KIST/PU Symposium, "Molecular Imaging and Theragnosis", 1-7, 2007.

15. Seale, Mary-Margaret, Zemlyanov, Dimitry, Cooper, Christy L., Haglund, Emily, Prow, Tarl W., **Reece, Lisa M.**, Leary, James F. "Multifunctional nanoparticles for drug/gene delivery in nanomedicine". Nanoscale Imaging, Spectroscopy, Sensing, and Actuation for Biomedical Applications IV, SPIE 6447: 64470E-1-664470E-9, 2007.

16. Seale, Mary-Margaret, Haglund, Emily, Cooper, Christy L., **Reece, Lisa M.**, Leary, James F. "Design of programmable multilayered nanoparticles with *in situ* manufacture of therapeutic genes for nanomedicine". Advanced Biomedical and Clinical Diagnostic Systems V, SPIE 6430: 1-7, 2007.

Other Published Articles – Purdue University

17. Zordan, Michael, Fatig, Ray, **Reece, Lisa**, Davisson, V. Jo, Leary James. "An efficient method to produce clonal colonies of cancer cells using Laser Enabled Analysis and Processing (LEAP)". Imaging, Manipulation, and Analysis of Biomolecules, Cells, and Tissues VI. SPIE 6859: 685910-1-685910-8, 2008.
18. Haglund, Emily M., Seale-Goldsmith, Mary-Margaret, Dhawan, Deepika, Stewart, Jane, Ramos-Vara, Jose, Cooper, Christy L., **Reece, Lisa M.**, Husk, Timothy, Bergstrom, Donald, Knapp, Deborah, Leary, James F. "Peptide targeting of quantum dots to human breast cancer cells." Colloidal Quantum Dots for Biomedical Applications III, SPIE 6866: 68660S-1-68660S-8, 2008.

Other Published Articles Pertinent to Thesis Work (UTMB)

19. Leary, J.F., **Reece, L.M.**, Hokanson, J.A., Rosenblatt, J.I. "Advanced "Real-time" Classification Methods for Flow Cytometry Data Analysis and Cell Sorting". SPIE 4622: 204-210, 2002.
20. Leary, J.F., Smith, J., Szaniszlo, P., **Reece, L.M.** "Comparison of multidimensional flow cytometric data by a novel data mining technique." SPIE, 6441, 2007.
21. Smith, Jacob N., **Reece, Lisa**, Szaniszlo, Peter, Leary, Rosemary C., Leary, James F. "Subtractive Clustering Analysis: A Novel Data Mining Method for Finding Cell Subpopulations". Imaging, Manipulation, and Analysis of Biomolecules and Cells: Fundamentals and Applications III, SPIE 5699: 354-361, 2005.
22. Leary, J.F., **Reece, L.M.**, Yang, X., Gorenstein, D. "High-Throughput Flow Cytometric Screening of Combinatorial Chemistry Bead Libraries for Proteomics and Drug Discovery". Advanced Biomed. And Clinical Diagnostic Systems III, SPIE, 5692: 216-223, 2005.
23. Prow, T., Salazar, Jose H., Rose, William A., Smith, Jacob N., **Reece, Lisa**, Fontenot, Andrea A., Wang, Nan A., Lloyd, R. Stephen, Leary, James F. "Nanomedicine-nanoparticles, molecular biosensors and targeted gene/drug delivery for combined single-cell diagnostic and therapeutics". Advanced Biomedical and Clinical Diagnostic Systems II, SPIE 5318, 1-11, 2004.
24. Leary, J.F., **Reece, L.M.**, Yang, X., Gorenstein, D. "High-Throughput Flow Cytometric Screening of Combinatorial Chemistry Bead Libraries for Proteomics and Drug Discovery". Advanced Biomed. And Clinical Diagnostic Systems III, SPIE, 5692: 216-223, 2005.
25. Prow, T.W., Salazar, J.H., Rose, W.A., Smith, J.N., **Reece, L.M.**, Fontenot, A.A., Wang, N.A., Lloyd, R.S., Leary, J.F. "Nanoparticles, Molecular Biosensors and Targeted Gene/Drug Delivery for Combined Single-Cell Diagnostics and Therapeutics." SPIE 5318: 1-11, 2004
26. Leary, James F., Szaniszlo, Peter, Prow, Tarl, **Reece, Lisa M.**, Wang, Nan, Asmuth, David M. "The Importance of High-Throughput Cell Separation Technologies for Genomics/Proteomics-Based Clinical Diagnostics". Clinical Diagnostic Systems: Technologies and Instrumentation, SPIE 4625, 1-8, 2002.

27. Leary, J.F., **Reece, L.N.**, Szaniszlo, P., Prow, T., Wang, N.: "High-Throughput Cell Analysis and Sorting Technologies for Clinical Diagnostics and Therapeutics". SPIE 4255: 16-27, 2001.

28. Smith, J.N., Prow, T., **Reece, L.**, Fontenot, A., Salazar, E., Wang, N., Rose, W., Szaniszlo, P., and Leary, J.F. "Subtractive clustering analysis: A novel data mining method for finding cell subpopulations". Cytometry Part A, 140, 2004.

29. Leary, J.F., McLaughlin, S.R., **Reece, L.N.**, Rosenblatt, J.I., Hokanson, J.A. "Real-time Multivariate Statistical Classification of Cells for Flow Cytometry and Cell Sorting: A Data Mining Application for Stem Cell Isolation and Tumor Purging" SPIE 3604: 158-169, 1999.

30. Prow, T., Salazar, J., Rose, W., Smith, J.N., **Reece, L.**, Fontenot, A., Wang, N., Leary, J.F. "Nanomedicine-nanoparticles, molecular biosensors, and targeted gene/drug delivery." Cytometry Part A, 59A 1: 107-107, 2004.

31. Chen, K.-H., **Reece, L.M.**, Leary, J.F. "Mitochondrial Glutathione Modulates TNF-α-Induced Endothelial Cell Dysfunction". Free Radical Biology & Medicine 27 (1/2): 100-109, 1999.

Other Published Articles – UTMB

32. Prow, T.W., Rose, W.A., Wang, N., **Reece, L.M.**, Lvov, Y., Leary, J.F. "Biosensor-controlled gene therapy/drug delivery with nanoparticles for nanomedicine". Advanced biomedical and Clinical Diagnostic Systems III, 199, SPIE 5692: 199-208, April 11, 2005.

33. Asmuth, D.M., Wang, N., Ying, L., Li, X.D., **Reece, L.**, Terry, N.H.A., Pollard, R.B., Nokta, M., Leary, J.F., White, A.R. "Cell Cycle Kinetic Dysregulation in HIV-Infected Normal Lymphocytes". Cytometry: Part A: 66A 41-51, 2005.

34. Szaniszlo, P.E., Wang, N., Sinha, M., **Reece, L.M.**, Van Hook, J.W., Luxon, B.A., Leary, J.F. "Getting the Right Cells to the Array: Gene Expression Microarray Analysis of Cell Mixtures and Sorted Cells". Cytometry 59A (2): 191-202, 2004.

35. Yang, X., Li, X. Li, Prow, T., **Reece, L.M.**, Bassett, S., Luxon, B., Herzog, N.K., Aronson, J., Shope, R., Leary, J.F., Gorenstein, D. "Immunofluorescence Assay and Flow-Cytometry Selection of Bead-bound Aptamers". Nucleic Acids Research 31 (10): 1-8, 2003.

36. Leary, J.F., He, F., **Reece, L.M.** "Application of Advanced Cytometric and Molecular Technologies to Minimal Residual Disease Monitoring". SPIE 3913: 36-44, 2000.

37. Leary, J.F., McLaughlin, S.R., **Reece, L.M.** "Application of a Novel Data Mining Technique to Cytometry Data". SPIE 3921: 84-89, 2000

38. Leary, J.F., He, F., Reece, L.N. "Detection and Isolation of Single Tumor Cells Containing Mutated DNA Sequences". SPIE 3603: 93-101, 1999.

39. Rajakulasingam, K., Durham, S.R., O'Brien, F., Humbert, M., Barata, L.T., **Reece, L.**, Kay, A.B., Grant, J.A. "Enhanced expression of high-affinity IgE receptor (FCεRI) α chain in human allergen-induced rhinitis with co-localization to mast cells, macrophages, eosinophils, and dendritic cells". J Allergy Clin Immunol 100 (1): 78-86, 1997.

40. Weido, A.J., **Reece, L.M.**, Alam, R., Cook, C.K., Sim, T.C. "Intranasal fluticasone propionate inhibits recovery of chemokines and other cytokines in nasal secretions in allergen-induced rhinitis." Annals of Allergy, Asthma & Immunology, 77(5): 407-415, 1996.

41. Sim, T.C., **Reece, L.M.**, Hilsmeier, K.A., Grant, J.A., Alam, R. "Secretion of Chemokines and Other Cytokines in Allergen-induced Nasal Responses: Inhibition by Topical Steroid Treatment". Am J Respir Crit Care Med 152: 927-933, 1995.

42. Sim, T.C., Hilsmeier, K.A., **Reece, L.M.**, Grant, J.A., Alam, R. "Interleukin-1 Receptor Antagonist Protein Inhibits the Synthesis of IgE and Proinflammatory Cytokines by Allergen-stimulated Mononuclear Cells." Am. J. Respir. Cell Mol. Biol., Vol. 11, 1994.

Other Published Articles – UTEP

43. Arenaz, P., **Bitticks, L. (surname from first marriage)**, Pannell, K.H., Garcia, S. "Genotoxic potential of crown ethers in mammalian cells: Induction of sister-chromatid exchange". Mutation Research, 280: 109-115, 1992.

44. Arenaz, P., **Bitticks, L.**, Pannell, K., Garcia, S. "Genotoxic potential of crown ethers in Salmonella typhimurium. Mutagenesis, vol. 4, no. 6, 437-438, 1989